
Development of an Ion Mobility Spectrometer for Heavy Element Research

Mustapha Laatiaoui



München 2009

Development of an Ion Mobility Spectrometer for Heavy Element Research

Mustapha Laatiaoui

Dissertation
zur Erlangung des akademischen Grades
Doktor der Naturwissenschaften

an der Fakultät für Physik
der Ludwig-Maximilians-Universität München

vorgelegt von
Mustapha Laatiaoui
aus Oujda

München, den 14.12.2009

Erstgutachter: Prof. Dr. Dietrich Habs

Zweitgutachter: Prof. Dr. Hartmut Backe (Universität Mainz)

Tag der mündlichen Prüfung: 18.01.2010

Summary

In the past, Ion Mobility Spectrometry (IMS) devices have proven to be powerful tools for state-selective mobility investigations at a variety of elements. Hence, the mobility spectrometry increasingly gains importance if dealing with the heaviest elements, where relativistic effects strongly affect their valence electron configurations.

During this work, a dedicated IMS apparatus has been developed, assembled, characterized and subsequently applied in systematic mobility studies at various lanthanide elements. The developed ion mobility spectrometer consists of a drift cell and a differential pumping section containing a quadrupole ion guide (QPIG), a mass filter and a channeltron detector. The drift cell is decoupled from the differential pumping section by an extraction nozzle. The apparatus is designed for mobility measurements at a ratio $E/n < 5$ Td (Townsend), where $1 \text{ Td} = 10^{-17} \text{ Vcm}^2$. The quantity E denotes the static electric field strength and n is the number density of buffer gas atoms in the cell. The efficiency ε_{ex} of ion extraction from the drift cell has been studied using a ^{223}Ra recoil ion source and is found to be $\varepsilon_{ex} = 0.57 \pm 0.10$ at a cell pressure of 80 mbar argon when using a nozzle of 1 mm throat diameter.

First systematic mobility measurements were performed using lanthanide filaments in off-line experiments. After evaporation from a given filament inside the cell, lanthanide atoms are resonantly ionized in a two-step excitation scheme via two suitable laser wavelengths. In a nearly homogeneous electric field and at an argon pressure of about 41 mbar, the ions drift towards the nozzle and get extracted. After extraction, the ions are guided by the QPIG into the high vacuum section, where mass selective detection occurs. The diffusion of the ions during their drift results in broadened peaks in the arrival time distributions (ATD). The lower limit of the normalized standard deviation of such peaks for usual ion mobility spectrometers can be given by $\sigma_t/t \approx 1\%$. With $\sigma_t/t \approx 1.2\%$ the developed spectrometer comes close to this figure of merit and thus provides a good tool for investigating the dependence of the mobility of heavy elements on their electronic configuration.

As expected from mobility theory, the lanthanide mobilities show a great similarity. The only exception is the element gadolinium, which exhibits an 8% lower reduced mobility of $K_0 = [1.692 (\pm 0.001)_{stat} (\pm 0.018)_{sys}] \text{ cm}^2/\text{Vs}$. The gadolinium peak in the arrival time distributions can be clearly resolved from the other investigated lanthanides at a resolving power of about 45 of the developed apparatus. The observed mobility deviation is assumed to be a direct consequence of occupying the d -orbital in singly charged gadolinium, which in turn has a significant impact on the ion-atom interaction potential. The latter is of particular interest in the mobility theory, which allows for quite accurate K_0 calculations. The rigid-sphere model is found to be too simple

when aiming at mobility estimations and it can be concluded that the long-range and intermediate-range terms in the interaction potential, which account for the polarizability of the gas atoms or the ion, cannot be safely ignored, especially at small E/n values.

Future application of mobility spectrometry to heavy elements at different E/n ratios may deliver significant knowledge about their ion-atom interaction potentials and may pave the way for electron configuration and relativistic contraction studies also in the region of superheavy elements.

Zusammenfassung

Bereits in der Vergangenheit haben moderne Mobilitätsspektrometer ihre Tauglichkeit für zustandsselektive Mobilitätsuntersuchungen bei zahlreichen chemischen Elementen unter Beweis gestellt. Die Mobilitätsspektrometrie gewinnt nun zunehmend an Bedeutung, wenn solche Untersuchungen auf die schwersten Elemente ausgedehnt werden, wo relativistische Effekte die atomaren Zustände ihrer Valenzelektronen stark beeinflussen.

Im Rahmen dieser Arbeit wurde ein Ionenmobilitäts-Spektrometer entwickelt, aufgebaut, charakterisiert und anschließend in systematischen Mobilitätsmessungen bei Lanthaniden eingesetzt. Es besteht aus einer Driftzelle und einer differentiellen Pumpstrecke, die eine lineare Paul-Falle, einen Massenfilter und einen Elektronenvervielfacher beinhaltet. Eine Düse dient zur Trennung der Driftzelle von der Pumpstrecke. Das Spektrometer ist konzipiert für Mobilitätsmessungen im Bereich von $E/n < 5$ Td (Townsend), wobei $1 \text{ Td} = 10^{-17} \text{ Vcm}^2$. Die Größe E bedeutet hier die statische elektrische Feldstärke und n ist die Dichte der Puffergasatome in der Zelle. Die Extraktionseffizienz der Driftzelle wurde mit Hilfe einer ^{223}Ra -Rückstoßquelle untersucht und beträgt $\varepsilon_{ex} = 0,57 \pm 0,10$ bei einem Zellendruck von 80 mbar Argon für eine Düse mit 1 mm Innendurchmesser.

Erste systematische Mobilitätsmessungen bei monoatomaren Lanthaniden wurden in Offline-Experimenten durchgeführt. Dabei wurden die gewünschten Elemente von einem Filament innerhalb der Zelle abgedampft und anschließend in einer Zwei-Stufen-Anregung mit zwei geeigneten Laserstrahlen resonant ionisiert. Die erzeugten Ionen driften so in einem fast homogenen elektrischen Feld bei einem Argon-Zellendruck von etwa 41 mbar in Richtung der Düse, von wo aus sie extrahiert werden. Danach werden sie mit Hilfe der linearen Paul-Falle zum massenselektiven Nachweis in der letzten Pumpsektion bei gutem Vakuum weitergeleitet. Die Diffusion der Ionen innerhalb der Driftzelle verursacht verbreiterte Peaks in den Zeitspektren. Gängige Mobilitätsspektrometer weisen daher eine relative Peakbreite von $\sigma_t/t \approx 1\%$ auf. Das in dieser Arbeit beschriebene Spektrometer erreicht eine relative Peakbreite von $\sigma_t/t \approx 1,2\%$ und stellt damit ein hervorragendes Hilfsmittel dar, um die Abhängigkeit der Mobilität von der elektronischen Konfiguration der Lanthaniden zu untersuchen.

Wie theoretisch erwartet ergeben sich für die untersuchten Lanthanide ähnliche Mobilitäten. Die einzige Ausnahme stellt das Element Gadolinium dar, welches eine um 8% kleinere sogenannte „reduzierte Mobilität“ von $K_0 = [1,692 (\pm 0,001)_{stat} (\pm 0,018)_{sys}] \text{ cm}^2/\text{Vs}$ aufweist. Bei einem Auflösungsvermögen des Spektrometers von ca. 45 können die Gadolinium-Peaks in Bezug auf andere Elemente eindeutig aufgelöst werden. Diese beobachtete Anomalie ist möglicherweise auf die Besetzung des d -Orbitals beim einfach geladenen Gadolinium zurückzuführen, welche

wiederum einen Einfluss auf das interatomare Wechselwirkungspotential hat. Letzteres ist von besonderer Bedeutung in der Ionen-Mobilitätstheorie, die eine sehr genaue Bestimmung von K_0 zulässt. Dieser Arbeit zufolge eignet sich das sogenannte „Rigid-Sphere-Model“ nicht besonders gut zur Bestimmung von Ionenmobilitäten, insbesondere nicht bei verschwindend kleinen elektrischen Feldern. Genauso ungeeignet sind Wechselwirkungspotentiale, bei denen die langreichweitigen oder mittelreichweitigen Terme vernachlässigt werden, die die Polarisierbarkeit der Gas-Atome oder des Ions berücksichtigen.

Eine zukünftige Anwendung der Mobilitätsspektrometrie bei schweren Elementen und bei verschiedenen E/n -Parametern könnte aufschlußreiche Informationen über deren interatomare Wechselwirkungspotentiale liefern. Sie könnte zudem einen experimentellen Zugang eröffnen zum Studium ihrer Elektronenkonfigurationen und der relativistischen Kontraktion der Valenzelektronenorbitale der besonders interessanten superschweren Elemente.

Contents

1	Introduction	1
2	Theory of ion mobility spectrometry	5
2.1	Diffusion and drift	5
2.2	The collision cross section	6
2.2.1	The rigid-sphere model	7
2.2.2	The ion-neutral interaction models	8
3	Preliminary considerations about the ion mobility spectrometer	13
3.1	The experimental method	13
3.2	Principle of resonance ionization using lasers	15
3.3	Requirements on the design of the drift cell	16
3.3.1	Principles of ion extraction	18
3.3.2	Considerations concerning the static electric field	20
3.3.3	Choosing a proper extraction nozzle	23
3.4	Considerations for the detection part	25
4	The experimental setup	29
4.1	The spectrometer	29
4.1.1	The drift cell	32
4.1.2	The gas supply system	34
4.1.3	The quadrupole ion guide	34
4.2	The laser system	37
4.3	Signal processing, data acquisition and measurement control system	39
4.3.1	The data acquisition system	39
4.3.2	Measurement control system during mobility experiments	40
4.3.3	Signal processing during extraction efficiency measurements	41
5	Preparatory experiments	45
5.1	Extraction efficiency measurements employing a ^{223}Ra recoil source	45
5.1.1	The ^{223}Ra recoil source	45
5.1.2	Optimization of the source potential	47
5.1.3	Determination of the extraction time	48
5.1.4	Determination of the extraction efficiency	50
5.2	Commissioning and optimizing the detection part of the spectrometer	53
5.2.1	The background pressures inside the differential pumping section	53
5.2.2	The potential configuration inside the detection part	53

5.3	Determination of highest possible E/n parameters	56
5.4	Estimation of the overall detection efficiency of the IMS apparatus . . .	57
6	Investigation of the time resolution by RIS methods	59
6.1	Creation of sample ions by RIS methods	59
6.2	Identifying the signals of sample ions	60
6.3	The arrival time distribution	61
6.3.1	The time resolution	66
6.3.2	Pressure effects	69
6.3.3	The influence of the laser beams	70
6.3.4	Ionization above the filament	71
6.4	The transit time of extracted ions	74
6.5	Consequences drawn from time resolution studies	76
7	Investigation of ion loss processes and background events	81
7.1	Ion loss processes due to chemical reactions	81
7.1.1	Chemical reactions	82
7.1.2	Charge transfer reactions	84
7.2	Molecule cracking	86
7.3	Thermionic emission of the filament	87
8	Ion mobility measurements in the lanthanide region	89
8.1	Experimental results	89
8.2	Extraction of the ion mobilities	94
8.3	Discussion of the mobility data	97
8.3.1	Lanthanide mobilities	98
8.3.2	Mobility of oxides	104
9	Outlook	107
A	Laser resonance ionization methods	110
A.1	The two-step photoionization process	110
A.2	Suitable excitation states of some actinide elements	111
B	The developed IMS software	112
B.1	The control software of the iseg high voltage modules	112
B.2	The control software of the DAQ system	114
C	Gas discharge experiments	117
D	SIMION simulations	118
D.1	The viscous damping model used in the drift time simulations	118
D.2	High-level language program (Lua) for drift time simulations	120
D.3	Lua code used for gas cooling simulations	121
E	Mobility of Tl^+ in argon	124

List of Figures

1.1	Effects of the relativistic contraction at heavy ions.	3
2.1	Effective reduced potential for different reduced angular momenta . . .	11
3.1	Principle of operation of the developed IMS.	14
3.2	Excitation scheme of sample atoms.	16
3.3	SIMION simulations of drift trajectories.	21
3.4	E/n parameter vs. the drift time of the ions.	22
3.5	Functional principle of quadrupole mass filters and ion guides.	26
3.6	Gas cooling inside the extraction chamber.	28
4.1	Schematic view of the novel ion mobility spectrometer.	30
4.2	Photograph of the novel IMS apparatus.	31
4.3	Cross-section plot of the drift cell.	32
4.4	The specially designed electric CF16-feedthrough.	34
4.5	Gas supply system of the drift cell.	35
4.6	One part of the quadrupole ion guide.	36
4.7	The used RF electric circuitry.	37
4.8	The laser system used in the IMS experiment.	38
4.9	Experiment control mechanism during mobility measurements.	42
4.10	Block diagram of the data acquisition system used for α decay readout.	43
5.1	The used recoil ion source.	46
5.2	Energy spectrum of the recoil ion source under gas conditions.	46
5.3	Potential optimization for the recoil ion source.	48
5.4	Determination of the extraction time.	49
5.5	Extraction time at different buffer gas pressures.	50
5.6	The extraction efficiency of the drift cell.	51
5.7	Background pressure in the differential pumping section.	54
5.8	The different static potentials used in the detection part of the IMS.	55
5.9	Optimization of the potential configuration inside the detection part.	56
6.1	Measured resonance and mass spectra for Er filaments.	60
6.2	Measured resonance and mass spectra for Yb, Ho and Dy filaments.	62
6.3	Measured resonance and mass spectra for Tb, Gd and Eu filaments.	63
6.4	The arrival time distribution of Er and ErO ions.	64
6.5	The influence of the electrostatic drift field on the arrival time spectra.	65
6.6	Normalized standard deviation of ATDs vs. different drift fields.	68

6.7	Variations in the gas number density.	69
6.8	The normalized standard deviation vs. laser beam diameter.	71
6.9	Comparison of ionization methods using optical fibers.	72
6.10	Landscape of erbium vapor above the filament.	73
6.11	Principle of transit time measurements.	75
6.12	Standard deviation σ for ATD peaks and for transit time spectra . . .	77
6.13	Determination of the transit time of the ions.	77
6.14	Example of multi-filaments as used during mobility experiments.	79
6.15	Superimposed mass spectra for Ho^+ and Gd^+	80
7.1	Suppression of gas impurities inside the drift cell.	83
7.2	Discrimination of oxides.	84
7.3	Reactions with water.	85
7.4	Example of primed multi-filaments.	86
8.1	ATDs of Gd^+ , Tb^+ and Ho^+	90
8.2	ATDs of Ho^+ , Er^+ , HoO^+ and ErO^+	91
8.3	Drift time means of some investigated lanthanides	92
8.4	Drift time means of some investigated lanthanide oxides.	93
8.5	Reduced mobilities of some investigated lanthanide ions.	99
8.6	Interaction potential of Yb^+ ions with argon at 300 K.	101
8.7	Mobility of Yb^+ in argon vs. E/n	102
B.1	The control panel for the iseg HV modules.	113
B.2	User interface of the listmode data acquisition software.	115
B.3	Electric circuitry of the used fast HV-switch.	116
C.1	Measured breakdown voltages.	117
E.1	Mobility of Tl^+ in argon.	124

List of Tables

3.1	Some lanthanide atomic states chosen for laser resonance ionization. . .	17
3.2	HV-potential used in the electric field calculations.	18
4.1	Geometry chosen for the electrodes near the nozzle.	33
4.2	Dye laser parameters used for atomic excitations.	38
4.3	The data acquisition system (Ni PXI 7833R).	40
5.1	HV-potentials used for the extraction efficiency measurements.	47
5.2	Potentials used in the detection part of the apparatus.	56
6.1	Vapor pressures of some lanthanide elements.	78
8.1	Drift time of some investigated ions.	94
8.2	Mobilities of some investigated ions.	96
A.1	Suitable excitation states of some actinide elements.	111

Some important symbols

α_p	: Polarizability of atoms.
b	: Impact parameter of an ion-atom collision.
d_d	: Drift distance.
d_d^{ref}	: Reference drift distance.
d_{Noz}	: Nozzle throat diameter.
D	: Diffusion coefficient.
ε_0	: Energy corresponding to the internuclear distance r_m .
ε_{ex}	: Extraction efficiency from the drift cell.
ε_{tot}	: Overall efficiency of the IMS apparatus.
E	: Electric field strength.
HV_B	: Breakdown voltage.
K	: Ion mobility at a certain gas pressure and a certain gas temperature.
K_0	: Reduced ion mobility.
μ	: Reduced mass.
n	: Gas number density.
n	: Integer number, which describes the steepness of the repulsion potential.
$\Omega^{(1,1)}$: Momentum transfer collision integral.
P_{cell}	: Cell pressure.
P_{cell}^{ref}	: Reference cell pressure.
$Q^{(1)}$: Momentum transfer cross section.
r_m	: Internuclear distance corresponding to the minimum of the ion-atom interaction potential.
r_c	: Capture radius for an ion-atom collision.
R_d	: Resolving power.
θ	: Deflection angle in an ion-atom collision.
t_t	: Transit time of ions inside the detection part of the spectrometer.
t_d	: Drift time of ions inside the buffer gas cell.
t_a	: Arrival time of ions.
t^{exp}	: Measured drift time of ions.
t^{sim}	: Calculated drift time of ions.
T	: Gas temperature.
T_{eff}	: Effective temperature of ions.
T_{Fil}	: Filament temperature.
v_d	: Drift velocity of ions.
V_{eff}	: Effective interaction potential.
V_{dis}	: Dispersion potential.

1 Introduction

Research on the mobility of trace amounts of ions through neutral gases began more than 100 years ago, and most of the theoretical work in this field was published in the sixties and seventies of the last century [1, 2]. Nowadays, Ion Mobility Spectrometry (IMS) [3] has gained widespread acceptance in many applications for detecting and identifying contaminant atoms or molecules [4]. In its simplest form an IMS device measures how fast gas phase ions drift in a uniform electric field through a given atmosphere. Based upon the ion mobility K , a parameter that depends on mass, size and shape of sample ions, the separation of chemical species is achieved, e.g. smaller ions move faster than larger ions through the drift region of an IMS device at the same conditions.

In commercial IMS systems the separation of the ions occurs typically on the order of tens of milliseconds. This feature combined with its ease of use, versatility, relatively high sensitivity and highly compact design has allowed IMS devices to be used as routine tools for e.g. the field detection of explosives, drugs or chemical weapons. Often an IMS device is equipped with a simple Faraday-cup [5], however, more advanced ion mobility instruments are coupled with mass spectrometers, where both ionic mass and size may be obtained simultaneously.

As a research tool, ion mobility has also shown great strides towards chemical reaction studies and the analysis of biological materials. In modern high-resolution IMS tools a resolving power close to 200 can be achieved [6]. Especially in ion chemistry, sophisticated IMS devices have proven to be powerful tools for a variety of investigations [7]. Kemper and Bowers [8], for example, have shown that not only electron configurations of monoatomic ions, which strongly impact the ion size, can be deduced from ion mobility measurements, but that it is even possible to distinguish between metastable ionic states. Hence chemistry of excited electronic states becomes possible also with IMS techniques. Most chemical investigations, however, focus on the mobility of abundant monoatomic ions or molecules such that only a few mobilities of heavy elements can be found in the literature [2]. At present the most advanced method for studying heavy and superheavy elements is the aqueous phase and gas phase chemistry of single atoms. This method yielded detailed chemical information up to element 108 (hassium) [9] and for element 112 [10]. Most recently also first experiments at element 114 [11] have been performed. The aim of such experiments is to compare the chemical properties within a group of homologue elements.

The lack of mobility information as well as the influence of increasingly strong relativistic effects on the valence electrons of heavy atoms and its consequence on their chemical

behavior have led to develop IMS techniques for the investigation of lanthanides and trace amounts of short-lived actinides [12, 13, 14, 15]. The contraction of neighboring actinides amounts to $> 1\%$ [16], whereof 20% are caused by relativistic effects [17]. Also QED effects gain importance for the heaviest elements and cause changes in the valence electron binding energies of $> 0.1\text{ eV}$ [18], which contributes to the actinide contraction. Deviations from the periodicity in the atomic shell structure may be the product of such an influence, which gains importance in particular for elements with a charge number $Z > 100$, where simple extrapolation of systematics, e.g. the oxidation states, electron affinity and complex formation, may not lead to reliable predictions.

These relativistic effects on the valence electrons are mainly due to the shrinking of the wave functions of s - and $p_{1/2}$ -electrons. Inner shell electrons influence indirectly via the shielding of the nuclear potential the valence electrons, which occupy the $4f$ -, $5d$ -, $6s$ - and $5f$ -, $6d$ - and $7s$ -orbitals in the case of lanthanides and actinides, respectively. The relativistic distortion of the charge distribution in the inner shells modify in a non-trivial way the potential in which the outer electrons move [19] and hence has a big impact on binding energies of corresponding electron configurations and therefore as well on the chemical properties of these elements. Quantum chemical atomic and molecular codes allow for predictions and descriptions of atomic and molecular properties [20]. However, direct comparison of the measured quantities with the quantum-mechanical observables would represent a microscopic test of Dirac-Fock calculations. The mean radius of the outermost orbital $\langle r_{out} \rangle$ and the mean spherical radius $\sqrt{\langle r^2 \rangle}$, for instance, are not only subject to the above mentioned relativistic contraction, but also reflect the electron configuration of the respective atoms [21] and ions [16], see Fig. 1.1. Thus, systematic studies of $\langle r_{out} \rangle$ or $\sqrt{\langle r^2 \rangle}$ of lanthanides, actinides and transactinides may contribute to a better understanding of the electronic structure in strong (nuclear) fields.

It was first stated in Ref. [22] that such relativistic effects for heavy elements can also be studied by the measurement of ionic radii. These may be extracted from ion mobility measurements in inert buffer gases like argon. Measuring the drift time of ions in electrical fields represents a rather simple access to the mobility of both ions and ion chemical compounds. In particular, this method is assumed to be sensitive to relative changes of radii, either for simple ions as a function of Z , or for a selected element for various ion chemical compounds. From the latter, information on the bond length can be extracted, which might be similarly sensitive to relativistic effects as well [23]. Thus IMS techniques provide a good tool for testing the relation between mobilities, electronic configurations and ionic radii of heavy elements.

IMS devices typically allow for wide variations of the buffer gas pressure, its temperature and the electric field strength. These variations allow for probing mobility theories [24, 25, 26] and for deducing the interaction potentials of a given ion-atom system. Such investigations are possible at heavy elements up to element fermium, which can be produced in sub-microgram quantities in high-flux nuclear reactors [27]. Considering mobility measurements of single, heavy or superheavy ions, extended measurements at different electric fields and/or buffer gas pressures may be hampered by

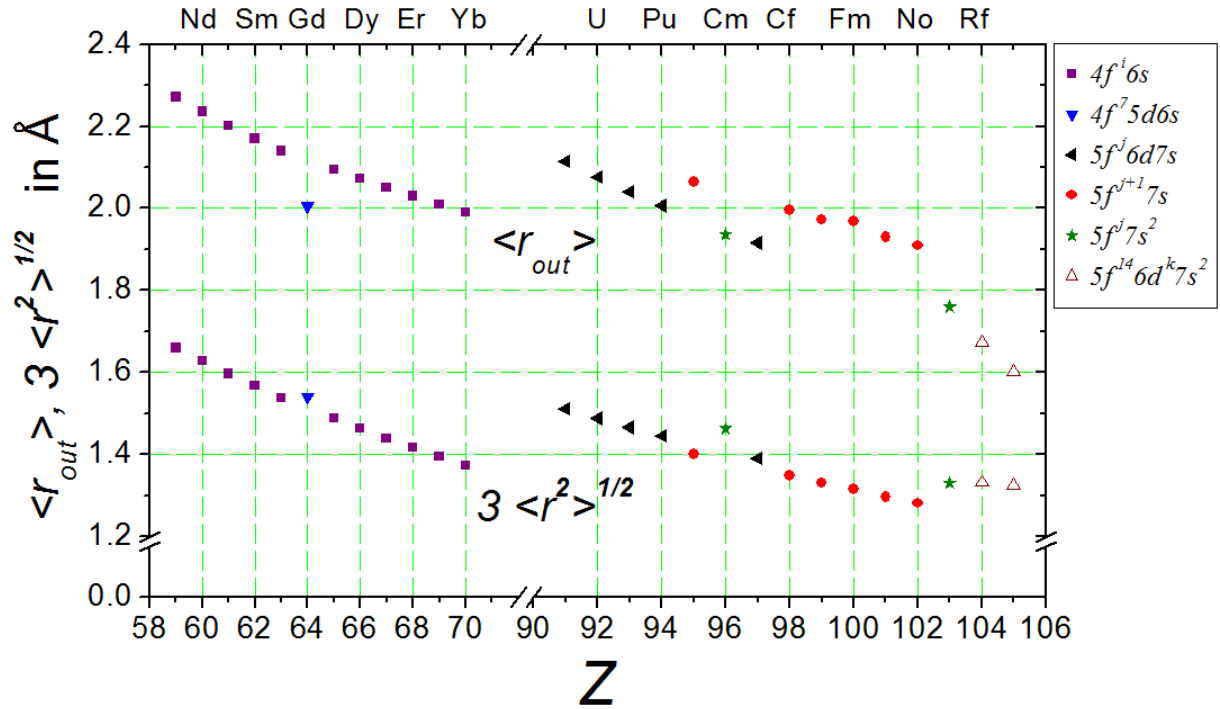


Figure 1.1: The mean radius of the outermost orbital $\langle r_{out} \rangle$ and the mean spherical radius $\sqrt{\langle r^2 \rangle}$ of singly ionized atoms as a function of the charge number Z . The mean spherical radius is scaled by a factor 3 just for illustration purposes. The number of electrons in the $4f$ -shell is $i = Z - 56$, in the $5f$ -shell $j = Z - 89$ and in the $6d$ -shell $k = Z - 103$. Values taken from Ref. [16].

limited quantities of sample elements provided during off-line experiments or by the low production rates in fusion reactions in on-line experiments. From this point of view, the development of an IMS apparatus for heavy and superheavy element research becomes quite a challenging issue.

In advance of mobility measurements of actinides and transactinides, the abundant rare-earth metals also allow for testing the effect of different electronic configurations on the ion mobility [16]. For instance, the $\langle r_{out} \rangle$ and $\sqrt{\langle r^2 \rangle}$ value of gadolinium ($Z = 64$) in Fig. 1.1 does not follow the general trend of the other rare-earth metals. This is a direct consequence of the exceptional occupation of the d -orbital in gadolinium. Due to the fact that atomic physics investigations of heavy elements require extremely sensitive methods, no systematic IMS studies have been performed with these elements so far.

The IMS apparatus presented in this work combines different approved spectroscopic methods, whereas its drift cell fulfills the requirements for gas cells used as ion sources of thermalized fusion products [28, 29]. Like most advanced mobility spectrometers around the world, the IMS apparatus is equipped with a mass spectrometer [30] for isotope-selective detection. In addition, the sample atoms are ionized by exploiting the

laser resonance ionization techniques [31, 32], which allow for a practically background free detection [33]. Therefore, the main task of this work is the characterization of the developed IMS apparatus and the investigation of the effects of different electronic configurations on lanthanide mobilities.

Outline of the thesis

In the next chapter, a brief overview of the theory of ion mobility spectrometry will be given describing the mathematical treatment, especially of heavy monoatomic ions drifting in lighter noble gases. Also a survey on the usual procedure followed for mobility calculations using different theoretical models will be presented here. In chapter 3, preliminary considerations about the design of a suitable IMS apparatus for heavy element research will be given. Special emphasis will be placed on the challenge such an apparatus is facing if used in on-line experiments. A brief introduction to resonance ionization of sample atoms using lasers will be provided also in this chapter. In chapter 4, the novel ion mobility spectrometer will be introduced. Within this chapter, a laser system used for resonance ionization of sample atoms as well as the data acquisition system used during the mobility measurements will be presented. Preparatory experiments, including extraction efficiency measurements using a radioactive ^{223}Ra recoil source and commissioning test experiments for determining the working parameters of the spectrometer, will be explained in chapter 5. Investigations of the time resolution of the spectrometer by means of laser resonance ionization techniques will be presented in chapter 6. Ion loss processes due to chemical reactions and the origin of background events that may perturb the mobility measurements will be explained in chapter 7. Chapter 8 contains the experimental results from mobility measurements carried out for lanthanide ions drifting in argon followed by an extended discussion of the applicability of the theoretical models introduced in the theory chapter of this thesis. An outlook for further improvements and further interesting physics experiments will be given in chapter 9.

2 Theory of ion mobility spectrometry

The foundations for IMS were laid in the early years of last century by Townsend [34] and were refined by several other investigators. Noteworthy are the books written by McDaniel and Mason [1, 2], both of which deal extensively with the phenomena of ion transport in gases from a theoretical point of view as well as from experimental considerations. Detailed treatment of ion motion in the drift region of an IMS apparatus can be found in these books and in the references therein. In this chapter, the theory of IMS will be introduced with the focus on the motion of singly charged ions in noble gases under weak electric field conditions.

2.1 Diffusion and drift

In an accumulation of n_i ions of a single type per unit volume in a noble gas the ions disperse through the gas by diffusion. This is the dominant force on the ions if the following conditions are met:

- There is no temperature gradient.
- The density of the ions is low enough that Coulomb repulsion can be neglected.
- No electric or magnetic fields are present.
- No chemical or charge transfer reactions occur.

The ion flux¹ J due to diffusion is then proportional to the magnitude of the concentration gradient ∇n_i , according to Fick's law: $J = -D|\nabla n_i|$, with the proportionality constant D that is a joint property of the ions and the gas through which they are diffusing. Since the velocity of the diffusive flow v is given by $J = n_i v$, Fick's law can be reformulated to give $v = -\frac{D}{n_i}|\nabla n_i|$.

Applying a weak uniform electric field throughout the gas initiates a steady flow of the ions along the field lines. This motion is superimposed on the diffusive motion described above. The average velocity of the ions is called the drift velocity v_d and is directly proportional to the electric field E via:

$$v_d = K \cdot E. \quad (2.1)$$

The mobility K , like the diffusion coefficient D , is a joint property of the ions and the gas through which the motion proceeds. Hence, the ion flux can be calculated

¹In order to simplify the expressions, absolute values of the flux, velocity and field vectors are used.

as $\mathbf{J} = n_i K \cdot \mathbf{E} - D|\nabla n_i|$. The relationship between the diffusion coefficient and the “low-field” ion mobility for singly charged ions is given by the familiar Einstein relation

$$K = eD/k_B T, \quad (2.2)$$

where e is the electron charge, k_B is the Boltzmann constant, and T is the gas temperature. This relation holds quite generally as long as both the field and the concentration gradients are small, so that the system is near equilibrium. Further, it is valid not only for dilute gases, but also for dense gases, liquids and isotropic solids [2]. The mobility can be easily determined by measuring the drift time of the ions as

$$t_d = \int_S ds/v_d(s) = \frac{1}{K} \int_S ds/E(s). \quad (2.3)$$

Here, $v_d(s)$ is the instantaneous ion drift velocity along a known trajectory S in a “low-field” $E(s)$.

To facilitate the comparison of results of different experiments, it is helpful to introduce the parameter E/n , with the number density n of the drift gas atoms. This parameter describes the conditions prevailing during the measurements and determines the average ionic energy acquired from the electric field. The Townsend unit, defined as $1 \text{ Td} = 10^{-17} \text{ Vcm}^2$, is used to express the E/n ratio. “Low-field” conditions generally hold as long as E/n is below $\sim 2 \text{ Td}$ [4]. But for heavy ions drifting in a lighter neutral gas, E/n values that still fulfill “low-field” conditions may be extended up to $^2 \approx 20 \text{ Td}$.

The mobility is inversely proportional to the number density of the gas atoms. Usually, it is converted to the “reduced mobility”, K_0 , defined by the equation

$$K_0 = K \cdot \frac{P}{P_0} \cdot \frac{T_0}{T}, \quad (2.4)$$

with the standard pressure $P_0 = 1013 \text{ mbar} = 760 \text{ Torr}$, the standard temperature $T_0 = 273.16 \text{ K}$ and the gas pressure P at which the mobility K was obtained.

2.2 The collision cross section

The general theory of Viehland and Mason [36] allows the ionic mobility in a single-component neutral gas to be calculated entirely from knowledge of the ion-neutral reduced mass $\mu = mM/(m + M)$ and interaction potential. The quantity M and m stands for the atomic mass of the neutral gas atoms and the ions, respectively. According to Mason and co-workers (see. Ref. [2], p. 289-299), one gets for singly charged ions

$$K = \frac{3e}{16n} \sqrt{\frac{2\pi}{\mu k_B T_{eff}}} \frac{1 + \alpha}{\Omega^{(1,1)}(T_{eff})}, \quad (2.5)$$

²Compare mobility data given in Ref. [35] for the heavy Tl^+ drifting in argon.

where T_{eff} is the effective temperature of the ions. Under “low-field” conditions of IMS measurements, the ion temperature is nearly equal to the gas temperature [37], such that for the one-temperature approximation adopted here, one gets

$$\frac{3}{2}k_B T_{eff} = \frac{3}{2}k_B T + \frac{1}{2}Mv_d^2(1 + \beta) \approx \frac{3}{2}k_B T. \quad (2.6)$$

The parameter β in Eq. (2.6) is a negligibly small correction factor, which is set equal to zero in the first order approximation. The higher correction term to the mobility in Eq. (2.5) α is generally less than 0.5% for an ion-atom mass ratio $m/M \gtrsim 4$ [25] and is neglected in first order approximation as well. The quantity $\Omega^{(1,1)}(T_{eff})$ is the so-called momentum transfer collision integral, which is a function of the effective temperature and contains all of the information on the ion-neutral interaction potential. It is defined as

$$\Omega^{(1,1)}(T_{eff}) = \frac{1}{2}(k_B T_{eff})^{-3} \int_0^\infty \varepsilon^2 Q^{(1)}(\varepsilon) \exp(-\varepsilon/k_B T_{eff}) d\varepsilon. \quad (2.7)$$

Here, ε is the relative energy of an ion-neutral collision, and $Q^{(1)}$ is the momentum transfer³ cross section, given by the equation (see [37] and [2] p.188)

$$Q^{(1)}(\varepsilon) = 2\pi \int_0^\infty (1 - \cos \theta) b db, \quad (2.8)$$

in which θ is the deflection angle in an ion-neutral collision of energy ε and impact parameter b . The angle θ is given by the classical equation of motion [38]

$$\theta(b, \varepsilon) = \pi - 2b \int_\varrho^\infty \left[1 - \frac{b^2}{r^2} - \frac{V(r)}{\varepsilon} \right]^{-1/2} \frac{dr}{r^2}. \quad (2.9)$$

In this equation ϱ is the distance of closest approach (the outermost zero of the bracketed expression) and $V(r)$ is the ion-neutral potential energy.

2.2.1 The rigid-sphere model

In the rigid-sphere model, both $\Omega^{(1,1)}$ and $Q^{(1)}$ can be written as [4]

$$\Omega^{(1,1)} = Q^{(1)} = \pi(r_{gas} + r_{ion})^2, \quad (2.10)$$

where r_{ion} and r_{gas} are the radii of the ions and of the neutral gas atoms, respectively. Taking Eq. (2.3) and (2.5) and assuming the validity of Eq. (2.6), r_{ion} can be deduced from mobility measurements if the radius r_{gas} of the buffer gas atom is known. Relative changes of ionic radii of two ion species A and B can be determined much more precisely from the relative drift time [15]

$$\frac{\Delta t_d}{t_d^B} \approx \frac{\Delta \Omega^{(1,1)}}{\Omega_B^{(1,1)}} \approx \frac{2\Delta r}{r_{gas} + r_B}, \quad (2.11)$$

³It is also called the transport or the diffusion cross section.

with $\Delta t_d = t_d^A - t_d^B$, $\Delta\Omega^{(1,1)} = \Omega_A^{(1,1)} - \Omega_B^{(1,1)}$ and $\Delta r = r_A - r_B$. The radius r_{ion} may provide a good approach to the $\langle r_{out} \rangle$ or $\sqrt{\langle r^2 \rangle}$ values mentioned before and hence allow a test of Dirac-Fock calculations for the heavy elements [16]. A detailed discussion on this issue is provided in Sect. 8.3 of this work.

As shown by Mason and McDaniel [2], some of the main features of mobility theory are reproduced by the rigid-sphere model:

- The velocity v_d and the temperature T_{eff} depend on E/n at a fixed temperature T as can be inferred from Eq. (2.5) and Eq. (2.1).
- The mobility K is inversely proportional to the neutral gas density n at a given T_{eff} according to Eq. (2.5).

2.2.2 The ion-neutral interaction models

To know the true interaction potential $V(r)$ in Eq. (2.9) is almost impossible. Instead, mathematical models that mimic this potential in a reasonable way provide good tools to test kinetic theories via mobility measurements. It is convenient to divide intermolecular forces into long-range, short-range and intermediate-range forces. The semi-empirical hard-core potential has shown its generality in most ion-neutral interactions and can be described as the sum of one repulsion term and two attraction terms [2],

$$V(r) = \frac{C_n}{r^n} - \frac{C_6}{r^6} - \frac{C_4}{r^4}, \quad (2.12)$$

where the constants n (not to be confused with the ion density introduced before), C_n and C_6 are adapted empirically to the experimental data. Such a potential is denoted as an $(n, 6, 4)$ potential, where n usually equals to 8, 10, 12 or 16 and describes the steepness of the repulsion⁴ as well as the width and depth ε_0 of the potential well, see Fig. 2.1. The corresponding position of ε_0 is usually given by the parameter r_m . The relationship between ε_0 and r_m can be found in Ref. [4] and [39]. The coefficient C_4 may be adapted to data but it is often known rather accurately, since it is given by the simple expression [40]⁵

$$C_4 = \frac{1}{2} \frac{e^2}{4\pi\epsilon_0} \alpha_p = 7.2\alpha_p, \quad (2.13)$$

where α_p is the polarizability of the neutral entity in units of \AA^3 and ϵ_0 is the dielectric constant. The constant C_4 is obtained in units of $\text{eV}\text{\AA}^4$.

⁴When the singly charged ion is brought close enough to the closed shell gas atom such that their electronic charge clouds can overlap, large distortions are produced because of the requirements of the Pauli exclusion principle, and there will be a decrease of charge density in the region between them. This decrease reduces the screening of the nuclear charges from each other, and the net effect is one of repulsion between the pair [2], which can be approximated by the C_n/r^n -term. The case of $n = \infty$ describes ion-atom collisions according to the rigid-sphere model mentioned before.

⁵The factor $(4\pi\epsilon_0)$ is set equal to 1 in the given reference.

At low temperatures, the mobility is dominated by the long-range polarization attraction, $-C_4/r^4$ of Eq. (2.12), in the sense that the mobility approaches a constant nonzero polarization limit, K_{pol} , as $T \rightarrow 0$ according to [40]

$$K_{pol} = K(T \rightarrow 0) = (13.876/\alpha_p^{1/2}) \left(\frac{m+M}{mM} \right)^{1/2}. \quad (2.14)$$

The number 13.876 is obtained when α_p is given in units of \AA^3 and the masses are in u. The mobility K_{pol} is, of course, in units of $\text{cm}^2\text{V}^{-1}\text{s}^{-1}$.

The inverse sixth power term in Eq. (2.12) describes the interaction based on permanent dipoles or higher multipoles of one partner, which induce multipole moments on the other⁶ [41], charge induced quadrupole moments, and the lowest order term of the dispersion interaction potential⁷ V_{dis} . Methods for estimating C_6 are summarized in Ref. [1]. It is often convenient to rewrite Eq. (2.12) in the dimensionless form

$$V(r) = \frac{n\varepsilon_0}{n(3+\gamma) - 12(1+\gamma)} \left[\frac{12}{n}(1+\gamma) \left(\frac{r_m}{r} \right)^n - 4\gamma \left(\frac{r_m}{r} \right)^6 - 3(1-\gamma) \left(\frac{r_m}{r} \right)^4 \right], \quad (2.15)$$

where ε_0 , r_m have their usual meanings and γ is a dimensionless parameter, ranging between 0 and 1, that measures the relative strength of the r^{-6} and r^{-4} terms. Extensive tabulations of the momentum transfer collision integral for (n, 6, 4) ion-neutral potentials can be found in e.g. [40], allowing one to test via mobility measurements ab initio interaction potentials such as those provided by Buchachenko and co-workers [42]. According to Eiceman and Karpas ([4], p. 66), a model including only the short-range repulsion and the long-range induced dipole attraction gives sufficiently good agreement with experimental data in most practical cases. Mason and McDaniel came to the same conclusion for bulky ions drifting in neutral gases ([2], p. 411). Hence, Eq. (2.15) is simplified to give an (n, 4) potential [43] (Eq. (2.16)), which may be sufficient to describe the interaction of monoatomic, heavy ions with lighter noble gas atoms

$$V(r) = \frac{n\varepsilon_0}{n-4} \left[\frac{4}{n} \left(\frac{r_m}{r} \right)^n - \left(\frac{r_m}{r} \right)^4 \right]. \quad (2.16)$$

From a given $V(r)$ one may define an effective potential [1]

$$V_{eff}(r) = V(r) + \frac{\varepsilon b^2}{r^2}, \quad (2.17)$$

⁶No multipole contributions are present for monoatomic ions drifting in noble gases.

⁷The dispersion potential is fundamentally quantum-mechanical in nature, but has a simple semi-classical interpretation [1]. Although the average motion of electrons about a single nucleus is spherically symmetric, at any instant of time there may be a temporary accumulation of negative charge in one region, hence an instantaneous dipole moment of the atom. This instantaneous dipole induces corresponding instantaneous dipole, quadrupole, etc., moments in another nearby atom. Although the instantaneous dipole moment averages to zero over a period of time, the interaction energy between it and its induced multipoles does not average to zero because the two moments are in phase.

with the centrifugal potential $\frac{\varepsilon b^2}{r^2}$, which conveniently describes orbiting collisions at low collision energies for interaction potentials with attractive components, see also the discussion of the obtained mobilities in Sect. 8.3.

Depending on the angular momentum $L = (2\mu\varepsilon)^{1/2} b$ of the ion-atom system, different effective potentials may be obtained. Figure 2.1 shows the effective potential for various values of reduced angular momentum $(\varepsilon/\varepsilon_0)^{1/2} (b/r_m)$ for a (12,4) potential, normalized on the potential minimum. During a collision and if the angular momentum is not too large, V_{eff} can have a maximum, as shown in Fig. 2.1, and an unstable circular orbit with a deflection angle $\theta = -\infty$ will result in accordance with Eq. (2.9) if the height of the maximum is equal to the relative collision energy ε .

As the angular momentum is increased, the height of the maximum in this centrifugal barrier increases, but eventually the maximum disappears entirely, degenerating to a horizontal inflection point of energy E_0 marked with the black dot in the same figure. Thus orbiting is not possible for collision energies larger than E_0 , resulting in a monotonic effective potential.

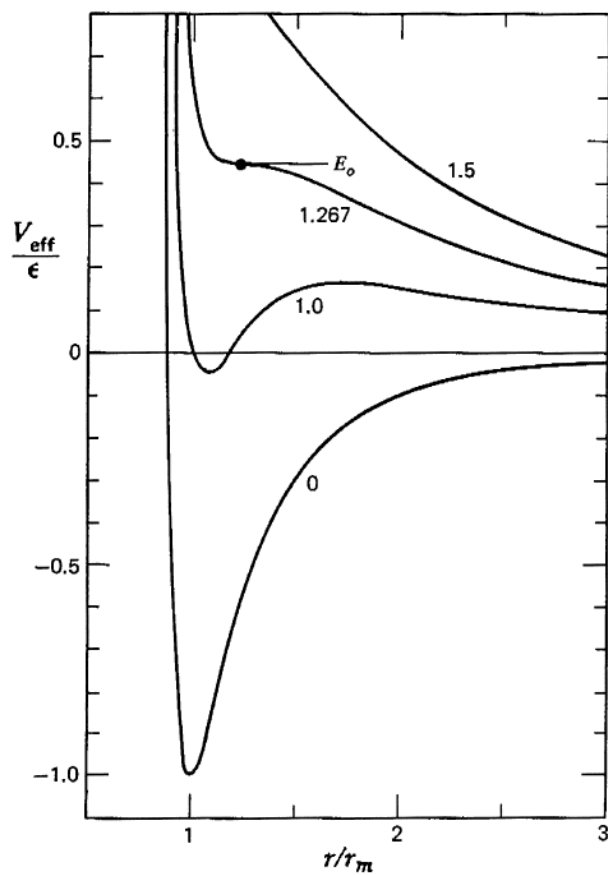


Figure 2.1: Effective reduced potential for various values of reduced angular momenta for a (12,4) potential. In this plot the potential minimum is referred to as ϵ instead of the usually used notation ε_0 and is located at the internuclear distance r_m . The numbers on the curves indicate the reduced angular momenta. The plot is taken from Ref. [1].

3 Preliminary considerations about the ion mobility spectrometer

Nowadays, buffer gas cells [44] are widely used at different accelerator laboratories as stopping chambers for energetic ions produced in fusion reactions. The reaction products are thermalized and stored in high-purity helium or argon and extracted as singly charged ions for post-acceleration or mass measurements [45]. Most of the gas cells are used as ion catchers, which are basically dedicated to the preparation of the reaction products [29]. However, the application of Resonance Ionization Spectroscopy (RIS) methods using lasers allows for re-ionization of the fusion products during the storing period and thus for the realization of ion sources of heavy isotopes with high element selectivity [46, 28]. Such a method opens new possibilities for hyperfine interaction studies at thermalized fusion products [47, 48] and provides access to atomic spectroscopy at trans-fermium elements for which no experimental data exist so far [49].

Furthermore, manipulating the ions existing inside the stopping cell via suitable electrostatic fields allows for ion mobility investigations [12, 13] and may provide deep insights into the interaction of those ions with the surrounding buffer gas atoms. Thus the use of buffer gas cells as drift cells/tubes in sophisticated ion mobility spectrometers exhibiting mass filtering features may provide a new access to mobility investigations up to the superheavy elements in online experiments.

In this chapter, design considerations for such an apparatus for IMS studies on heavy elements will be presented. A brief introduction to resonance ionization of sample atoms via laser beams will be also given in this chapter.

3.1 The experimental method

The spectrometer, like standard drift-tube mass spectrometers [1], consists of a buffer gas cell containing several drift electrodes and a detection part in which vacuum conditions prevail, see Fig. 3.1. During operation, the buffer gas flows continuously through a nozzle on the axis of the drift cell, whereas the cell pressure is held constant at some desired value, usually a few tens of mbar. The detection part of the spectrometer consists of a differential pumping section in which not only pumping out of the buffer gas but also mass analysis and the detection of the ions under investigation occur. Similar concepts were implemented before at the University of Mainz ([50], [51]).

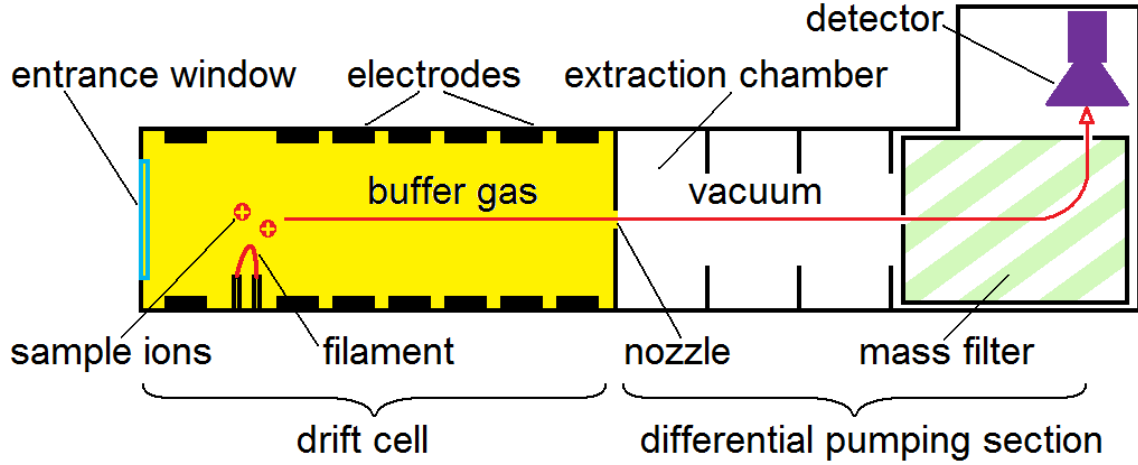


Figure 3.1: Principle of operation of the ion mobility spectrometer for heavy element research.

In online experiments the ions of interest are energetic fusion products that enter the cell through a thin entrance window and get fully stopped inside the cell mainly as singly charged ions [52]. Most heavy elements of interest, however, can be studied in off-line experiments exploiting the resonance ionization spectroscopy methods [30, 53]. In such investigations, no entrance window is needed. The elements are directly evaporated from primed filaments mounted inside the cell and are then resonantly ionized via suitable laser beams, see Sect. 3.2.

All ions existing inside the cell at a certain starting position and time $t_0 = 0$ drift in a uniform electric field towards the nozzle (Fig. 3.1), where the friction force in the emerging buffer gas jet dominates the ion motion [54] such that the ions are extracted out of the cell into the so-called extraction chamber. Subsequently, the extracted ions are transferred using suitable electric fields through the differential pumping section to a mass filter, which transmits exclusively ions of desired charge-to-mass ratios [55, 56]. After passing the mass filter, the ions of interest are transmitted to a particle detector, which registers their arrival time t_a .

Hence, the ions undergo a drift motion inside the cell characterized by the drift time t_d and a flight motion in the differential pumping section characterized by the transit time t_t . The mean arrival time $\langle t_a \rangle$ is just the sum of both quantities:

$$\langle t_a \rangle = \langle t_d + t_t \rangle = \langle t_d \rangle + \langle t_t \rangle. \quad (3.1)$$

In most cases the mean value of the transit time $\langle t_t \rangle$ is negligibly small compared to the mean drift time of the ions $\langle t_d \rangle$.

3.2 Principle of resonance ionization using lasers

In this section, some physical background and the functionality of laser resonance ionization will be briefly reviewed. This method is most favored in this work for ionizing sample atoms in off-line experiments due to its element selectivity features [32, 33]. For more detailed information on this topic, the reader is referred to the numerous textbooks about lasers and laser spectroscopy techniques, e.g. [57, 58, 59].

As a general rule, the laser ionization of a single atom takes place only if it gets excited to energy levels beyond its ionization potential (IP) [31]. Two-step photoionization may be the simplest method for laser ionization of neutral atoms [59]. In this method, the sample atoms are resonantly ionized using two laser beams of different wavelengths in a two-step procedure:

1. Assuming a sample atom is in its ground state (GS) configuration, it first gets excited by a laser beam with a wavelength corresponding to a wavenumber $\bar{\nu}_{12}$.
2. Simultaneously with the first step, another laser beam ionizes the excited atom.

Figure 3.2 (a) shows such an excitation and ionization scenario using an excimer laser-pumped dye laser system. The excitation in the first step is achieved by the dye laser, which provides tunable excitation energies corresponding to wavelengths between 350 nm and 960 nm [58, 60, 61] with photon fluxes $\leq 10^{15}$ photons per pulse and cm^2 , whereas the second step is achieved by the excimer laser of fixed excitation energies. The tunability of the dye laser makes such a laser system very well suited for atomic-level search and for resonance ionization of most known elements. At resonance of the first step, see Fig. 3.2 (b), the highest ionization rates are registered reflecting an efficient population and probable saturation of the excited state (ES). Of course, ionization takes place only if photons of both excitation energies corresponding to $\bar{\nu}_{12}$ and $\bar{\nu}_i$ coincide in space and time at the sample atom. This method is almost element selective [33] due to the diversity in the energy levels of atoms and hence can be applied only to elements of known and suitable excitation schemes. Trans-fermium elements, for instance, remain a big challenge for this technique, which recently showed great strides in heavy element spectroscopy investigations [51, 49, 48]. The ionization efficiency achievable with the two-step photoionization method is treated in Appendix A.1.

Thanks to the pioneering work in atomic physics, spectroscopic data of most elements of the periodic table have been made available in various scientific publications as well as on the world wide web [62]. Envisaging ion mobility measurements on lanthanide elements, suitable excitation levels of some of them are selected and shown in Tab. 3.1. A similar table for actinide elements can be found in Appendix A.2. The bolded states in Tab. 3.1 are chosen for resonance ionization of sample atoms in the mobility measurements carried out in this work. All listed excited states decay into the ground state by emitting photons in the blue and UV range of the electromagnetic spectrum. Their decay time is almost in the nanosecond range [63]. Hence, timing the overlap

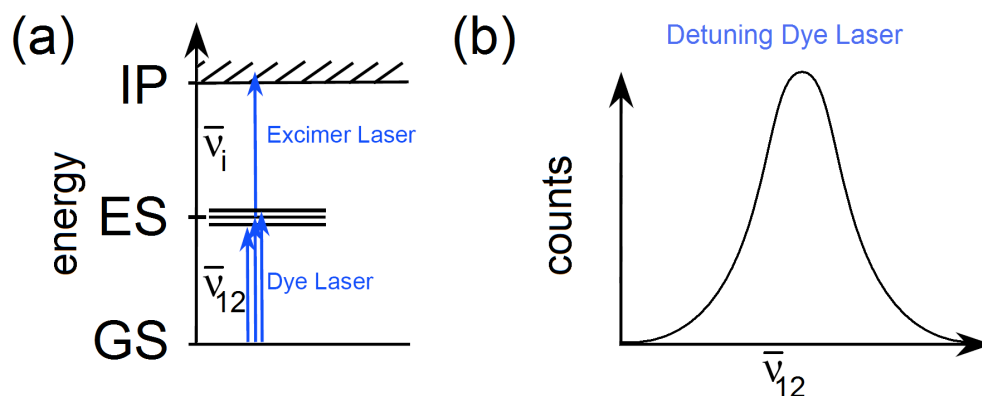


Figure 3.2: Excitation scheme of sample atoms investigated in the mobility measurements. The resonance ionization occurs with two laser wavelengths of energies $\bar{\nu}_{12}$ and $\bar{\nu}_i$ if the sum of both is more than the ionization potential (IP). (a) Search of a suitable excitation energy $\bar{\nu}_{12}$ using the dye laser. In this case, $\bar{\nu}_i$ provided by the excimer laser is kept constant. (b) Detuning the dye laser allows for finding the resonance at which the ion counts registered drastically increase.

of the laser beams becomes mandatory for ionization, especially when working with pulsed laser systems, which usually provide laser pulses of some nanosecond duration.

3.3 Requirements on the design of the drift cell

In order to be used also in online experiments, the ion mobility spectrometer should have a drift cell that fulfills the requirements for buffer gas cells used as ion sources of thermalized fusion products.

First of all, the apparatus has to be efficient enough such that trace amounts of short-lived isotopes can be still detected. One way to increase the apparatus efficiency is to suppress unwanted chemical reactions of the sample ions with the surrounding buffer gas impurities. This can be achieved when only materials suited for ultra-high vacuum chambers are used, thus providing the possibility of baking out the drift cell before beginning any mobility measurement.

For an efficient stopping of energetic fusion products and in order to minimize the spacial distribution of the thermalized ions, one may preferably operate the spectrometer using argon (Ar) as a buffer gas instead of helium (He). At the beginning of the drift path the electrodes inside the cell have to encompass the stopping volume of the reaction products, which amounts, e.g., for Yb^+ ions produced in the nuclear fusion reaction $^{107}\text{Ag}(^{52}\text{Cr}, p3n)^{155}\text{Yb}$ at the velocity filter SHIP [64] at GSI, to about 10^2 cm^3 having lateral extension $\sigma_x \approx 23 \text{ mm}$ at an argon buffer gas pressure of 100 mbar [49]. Therefore ring electrodes of inner diameters more than $3\sigma_x = 69 \text{ mm}$ must be included

Table 3.1: Overview of some lanthanide atomic levels that may be exploited for the two-step photoionization process. The wavelength in air λ_{12} , the wavenumber $\bar{\nu}_{12}$ and the total angular momentum J are given for each energy level. The first row of each group gives the ground state values of the corresponding element. Values taken from Ref. [62].

Element	λ_{12} [Å]	Configuration	Term	J	$\bar{\nu}_{12}$ [cm ⁻¹]
Europium (Eu)		$4f^7 6s^2$	a^8S°	7/2	0
	4661.88		y^8P	5/2	21444.58
	4627.22		y^8P	7/2	21605.17
	4594.03		y^8P	9/2	21761.26
Gadolinium (Gd)		$4f^7 5d 6s^2$	$^9D^\circ$	2	0
	4573.81	$4f^7 5d 6s 6p$	9P	3	21857.475
	4274.17	$4f^7 5d 6s 6p$	9F	3	23389.782
	3684.13	$4f^7 5d 6s 6p$	9P	3	27135.695
Terbium (Tb)		$4f^9 6s^2$	$^6H^\circ$	15/2	0
	4338.41	$4f^9 6s 6p$	(15/2, 1)	13/2	23043.43
	4326.43	$4f^9 6s 6p$	(15/2, 1)	17/2	23107.25
	4318.83	$4f^9 6s 6p$	(15/2, 1)	15/2	23147.92
Dysprosium (Dy)		$4f^{10} 6s^2$	5I	8	0
	4211.72	$4f^{10} 6s 6p$	(8, 1) ^o	9	23736.60
	4194.84	$4f^9 5d^2 6s$		8	23832.07
	4186.82	$4f^{10} 6s 6p$	(8, 1) ^o	8	23877.75
	4045.97	$4f^{10} 6s 6p$	(8, 1) ^o	7	24708.96
	4577.78		(7, 2) ^o	9	21838.55
Holmium (Ho)		$4f^{11} 6s^2$	$^4I^\circ$	15/2	0
	4173.23	$4f^{11} 6s 6p$	(13/2, 2)	13/2	23955.69
	4163.03	$4f^{11} 6s 6p$	(15/2, 1)	13/2	24014.22
	4103.84	$4f^{11} 6s 6p$	(15/2, 1)	17/2	24360.81
	4053.93	$4f^{11} 6s 6p$	(15/2, 1)	15/2	24660.80
	4040.81	$4f^{10} 5d 6s^2$		13/2	24740.52
Erbium (Er)		$4f^{12} 6s^2$	3H	6	0
	4722.69	$4f^{11} 5d^{5/2} 6s^2$	(11/2, 5/2) ^o	7	21168.430
	4151.11	$4f^{12} 6s 6p$		5	24083.166
	4087.63	$4f^{11} 5d 6s^2$		6	24457.139
	4007.96	$4f^{12} 6s 6p$		7	24943.272
	3973.58	$4f^{11} 5d^2 6s$		7	25159.143
	3973.036	$4f^{11} 5d 6s^2$		5	25162.553
	3892.68	$4f^{11} 5d 6s^2$		5	25681.933
	3862.85	$4f^{12} 6s 6p$		6	25880.274
Ytterbium (Yb)		$4f^{14} 6s^2$	1S	0	0
	3987.99	$4f^{14} 6s 6p$	$^1P^\circ$	1	25068.222
	3464.37	$4f^{13} 5d^{5/2} 6s^2$	(7/2, 5/2) ^o	1	28857.014

Table 3.2: HV-potentials used in the electric field calculations, see Fig. 3.3. The filament potential is 954 V in Fig. 3.3 (c) and 800 V in Fig. 3.3 (b). The resulting mean drift field is about 18 V/cm.

U_{22}	U_{21}	U_{20}	U_{19}	U_{18}	U_{17}	U_{16}	U_{15}
1026V	1026V	1026V	1026V	942V	918V	888V	858V
U_{14}	U_{13}	U_{12}	U_{11}	U_{10}	U_9	U_8	U_7
828V	798V	768V	732V	696V	660V	618V	576V
U_6	U_5	U_4	U_3	U_2	U_1	U_{Noz}	
528V	468V	408V	342V	264V	180V	126V	

in the cell design. Additionally, the spectrometer has to be sensitive enough such that mobility variations in the order of 1% among lanthanides, actinides and transactinides can be easily detected. This requirement may be fulfilled for elongated drift regions inside the cell. The drift distance should be large enough that ions will travel a negligible fraction of the total distance before energy equilibration in the drift field is achieved. For an argon pressure between 10 mbar and 100 mbar, the drift region may range between 10 cm and 50 cm as usually taken for scientific IMS instruments [2].

Another important feature of buffer gas cells is the fast extraction of short-lived isotopes. In fact, most known elements exhibit stable isotopes or isotopes of half-lives more than a second, such that fast extraction is not a crucial parameter for mobility measurements. However, the extraction time of the ions has to be less than 100 ms so that certain superheavy elements exhibiting only short-lived isotopes remain accessible via IMS techniques. Usually this goal is easily achieved by adjusting a proper electric field and/or buffer gas pressure inside the drift cell.

3.3.1 Principles of ion extraction

Several simulations have been carried out in order to study the ion extraction mechanism, to optimize the electrode system and to fix the geometry of the drift cell. Electric fields and $^{215}\text{Po}^+$ ion trajectories are calculated using the computer code SIMION [65] and are shown in Fig. 3.3. The SIMION code turned out to be a powerful tool for drift motion simulations [66, 67] by implementing a viscous damping algorithm in the calculations, see Appendix D.2. The corresponding electrode potentials used in these simulations are listed in Tab. 3.2.

Three different configurations during mobility measurements in on-line experiments are shown in this figure. After passing a thin entrance window, the heavy fusion reaction products are stopped in the drift cell at an argon pressure of about 40 mbar. About

87% of the ions thermalize in the 1+ charge state [52] and can be manipulated with suitable electric fields inside the buffer gas cell. For ion extraction now, two different methods are possible:

1. The stopped ions are guided directly along the drift path from the stopping volume until arriving at the extraction nozzle. This method is best suited for trans-fermium elements for which no information on laser excitation schemes is available. A possible candidate element for mobility investigations using this method may be nobelium ($Z = 102$), which can be produced at the velocity filter SHIP [64]. The isotope ^{254}No ($t_{1/2} = 55$ s), for instance, is produced by the fusion reaction $^{208}\text{Pb}(^{48}\text{Ca}, 2n)^{254}\text{No}$ with a production cross section of about $2 \mu\text{b}$ at a projectile energy of 216 MeV [68], which corresponds to a target production rate of ≈ 17 ions per second.

The starting position z_0 and starting time of the ion drift t_0 can be determined using the signal of e.g. a parallel plate counter [69, 70], which can be mounted in front of the entrance window. Alternatively to the method using parallel plate counters, one may be able to deduce relative differences of the radii or mobility of heavy ions and argon ions from relative drift time measurements, see Eq. (2.11). Argon atoms are ionized during the slowing down of the fusion products and can be registered at a different time with respect to the heavy ion itself, providing significantly different mobilities but similar drift paths of both species.

Both scenarios are pursued in Fig. 3.3 (a), where Po^+ ions start to drift at 320 mm from the nozzle along the shown trajectories and get electrostatically focused as the potential gradient increases just 50 mm near the nozzle. For simplicity and purposes of illustration, a transversal sequence of Po^+ ions at the same longitudinal position z , where the stopping volume is located, has been considered.

2. The stopped ions are guided during an accumulation period onto a filament/catcher where they neutralize, see Fig. 3.3 (b). The accumulation efficiency is strongly affected by the spatial distribution of the ions in the cell and by the filament potential, which is decreased by 154 V down to 800 V, while other potentials remain unchanged according to Tab. 3.2. The Po^+ trajectories shown in this figure imply that only a small fraction of the stopped ions hit the tip of the filament where evaporation of elements under test takes place.

During a second period, while the production beam is switched off, the atoms are re-evaporated and resonantly ionized using suitable laser beams before they are guided along the drift path towards the nozzle, see Fig. 3.3 (c). This method, of course, is applicable only for elements of known excitation schemes. Both the accumulation as well as the evaporation and laser ionization efficiencies have a significant effect on the overall efficiency of a such method. However, this technique has the advantage that it is practically background free due to the element-selective laser resonance ionization (see Sect. 3.2 for more details). In addition, the starting time t_0 and the location of the ions are well defined by the laser-vapor interaction time and volume.

The latter method is also well suited for off-line experiments using commercially available lanthanide foils [71] or filaments with trace amounts of heavy actinides as demonstrated using a 4 ng sample of the element fermium [12]. Thus Fig. 3.3 (c) shows the only configuration used for lanthanide mobility investigations, which are the main objective of this work.

3.3.2 Considerations concerning the static electric field

Envisaging mobility spectrometry in on-line experiments, a high time resolution and detection efficiency has to be considered while applying suitable electrode potentials. The electric field inside the cell is a crucial parameter concerning the time resolution of any IMS apparatus, see Sect. 6.3.1. Therefore some considerations have to be made about the electrode system in order to find an optimum electric field for ion extraction.

The influence of the electric field on the extraction efficiency and on the time resolution

The design of the electrode system shown in Fig. 3.3 as well as the corresponding potentials listed in Tab. 3.2 are believed to allow for a mobility resolution of about $\Delta K/K \approx 1\%$, which is necessary for the observation of changes in the momentum transfer collision integral $\Omega^{(1,1)}(T_{eff})$ introduced in Sect. 2.2. However, such a good resolution may be achieved only if both the starting time and the starting position of the ions are very well known. Without further knowledge of these parameters, the resolution will be limited by the ratio of the width of the stopping distribution of the sample ions to the length of the drift path to $> 7\%$ for the electrode system shown in Fig. 3.3. In order to minimize the drift time differences caused by different lateral starting positions of the ions, the potentials are chosen such that the ions drift in a homogeneous electric field of about 18 V/cm before they are focused towards the axis of symmetry near the nozzle. For instance, the Po^+ ions starting at a distance < 12 mm from the axis of symmetry as shown in Fig. 3.3 (a), exhibit a relative difference in the drift time of $\delta t_d/t_d \approx 10^{-3}$, when diffusion phenomena are neglected in the simulations.

To improve the overall efficiency, one may apply radio-frequency (RF) fields [72] to the focusing electrodes near the nozzle, which are characterized by a decreasing inner diameter in Fig. 3.3, instead of the electrostatic focusing mechanism exploited here. RF fields, however, may dramatically distort the arrival time distribution of the ions and make an accurate estimate of the drift path almost impossible.

The potential configuration used in Fig. 3.3 (a) and (c) shows a focusing mechanism by the steadily increasing electric field during the ion drift motion. Due to the non-vanishing width of the conducting nozzle at the potential U_{Noz} , all ions are guided onto this electrode if they arrive at a distance $\geq d_{Noz}/2$ from the axis of symmetry. Here, d_{Noz} stands for the nozzle throat diameter. Those ions make the dominant fraction of the ions transported from the stopping or the ionization volume centered around the

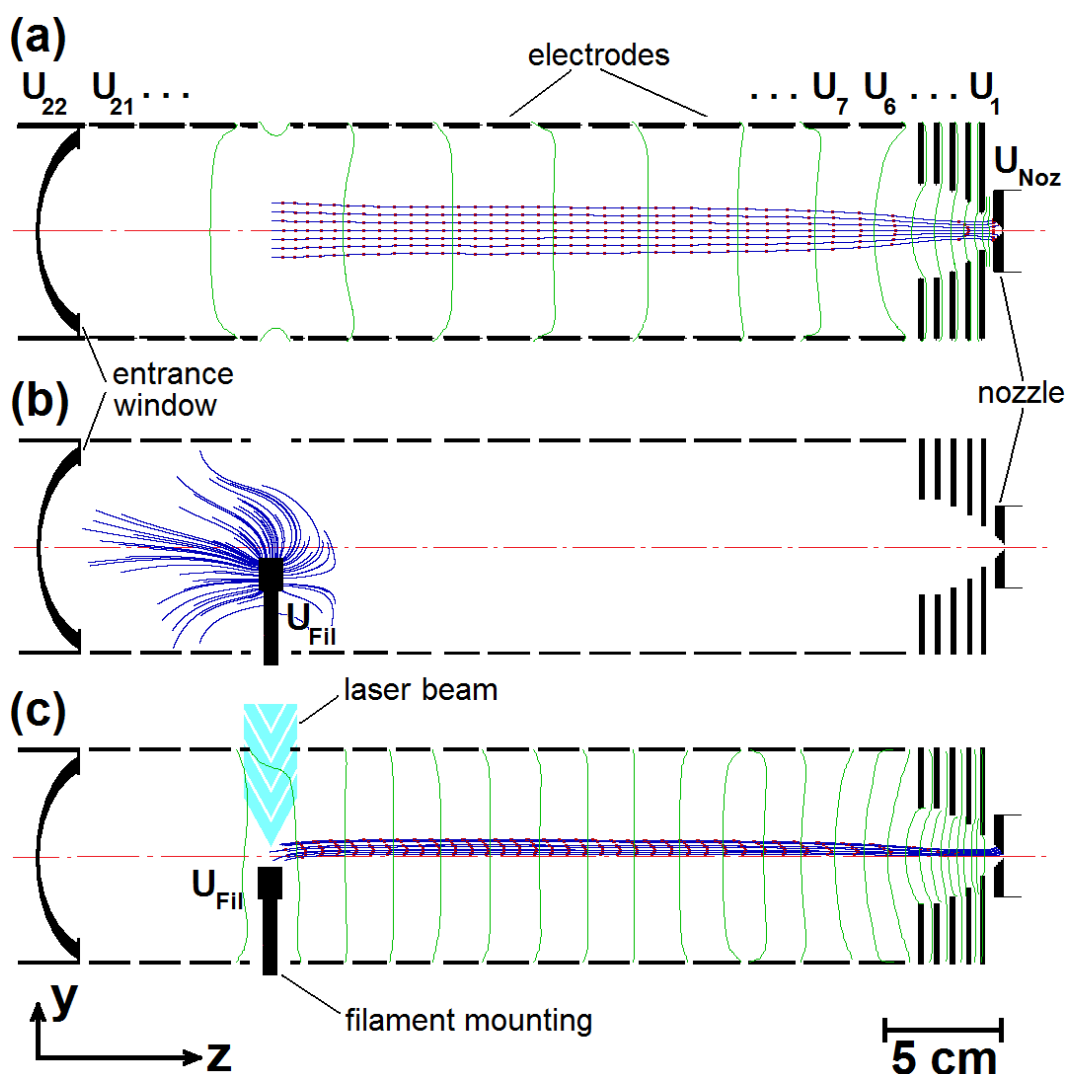


Figure 3.3: SIMION simulations of equipotential lines and $^{215}\text{Po}^+$ ion trajectories for different configurations during mobility measurements in on-line experiments. The corresponding electrode potentials used in the simulations are listed in Tab. 3.2. Heavy ions produced in fusion reactions are stopped in the gas cell at ≈ 40 mbar argon, mostly in +1 charge state, drift in a homogeneous electric field and subsequently are extracted at the nozzle. Such a scenario is pursued in (a), where Po^+ ions start to drift at 320 mm distance from the nozzle along the shown trajectories and get electrostatically focused as the potential gradient increases just 50 mm near the nozzle. Catching the stopped ions by a filament/catcher, evaporating and ionizing them again is shown in (b) and (c), respectively. Since lanthanides of interest are commercially available as thin foils, (c) is the only configuration used in the IMS measurements presented in this work. The time stamps of 1 ms are indicated on each trajectory (—).

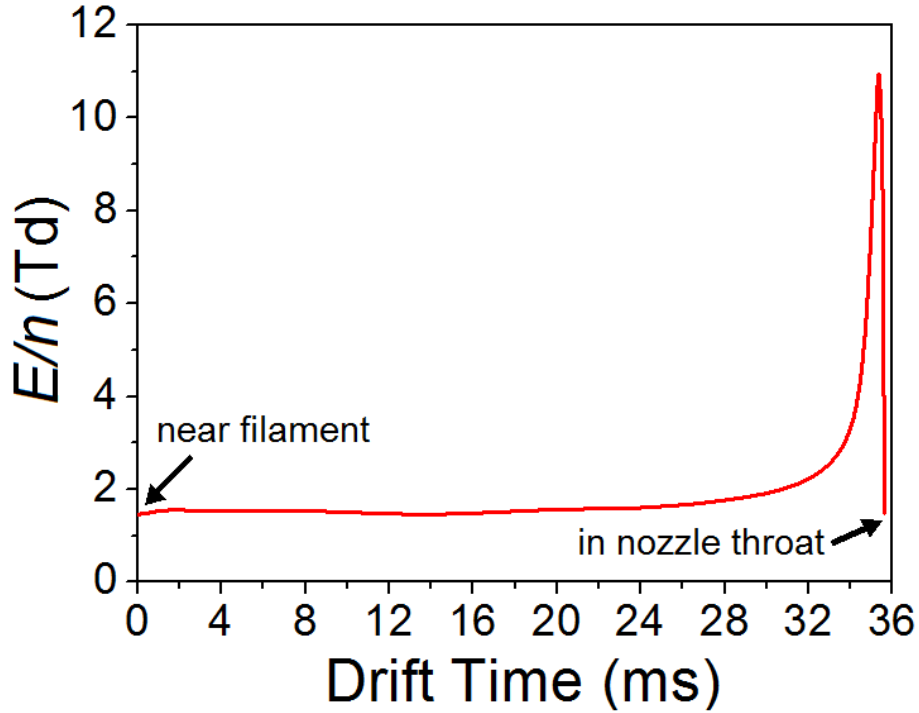


Figure 3.4: E/n parameter vs. the drift time of the Po^+ ions starting above the filament according to case (c) in Fig. 3.3. The ions need only 5% of the drift time to cross the focusing electrodes. The mean E/n amounts to 1.8 Td.

filament position even though high electric fields are set at the focusing electrodes near the nozzle.

In Ref. [73], it has been proposed to slow down the ions in front of the nozzle so that the gas-flow becomes the dominating effect, which would in turn lead to further electrostatic defocusing. A similar idea was followed in the potential configuration shown in Tab. 3.2. The electric field steadily increases from U_{22} to U_1 and decreases between the first electrode and the nozzle, which reduces the mean radial velocity of the ions hitting the nozzle cone to about $\overline{v_{rad}} \approx 7.7$ m/s. In this case, the electrostatic forces can be counteracted by the friction force of the gas flow [54], leading to an efficient extraction of the ions inside the emanating buffer gas.

Satisfying the “low-field” conditions

The average ionic energy acquired from the electric field has to be as low as possible in order to justify the approximations mentioned in Sect. 2.2. Electric field inhomogeneity and high E/n parameters broaden the arrival time distribution of the ions and increase the mobility uncertainty [2]. According to simulations for the case shown in Fig. 3.3 (c), $^{215}\text{Po}^+$ ions drift in an expanded homogeneous low electric field and thereby cross an inhomogeneous 5 cm long region inside the focusing electrodes. In Fig. 3.4 the obtained E/n parameter vs. the drift time of these ions are shown. From this figure, it becomes

clear that crossing the inhomogeneity with E/n parameters up to 11 Td takes only a small fraction of the drift time (5%), due to the relatively high ion velocities in that region. The average ionic energy acquired from the field is still low enough that “low-field” conditions are satisfied, see also Sect. 2.1. Hence, the E/n parameter is assumed to be constant when working with the potential configuration listed in Tab. 3.2. It can be taken equal to its mean value, which in this case amounts to 1.8 Td.

The risk of gas discharges

According to simulations shown in Fig. 3.3, high electric fields in the drift region are present especially beneath the focusing electrodes, which may come close to the critical field for voltage breakdown in argon. For the theoretical description of the gas breakdown, the Townsend equation [74] is widely used,

$$\gamma [\exp(\alpha d^*) - 1] = 1, \quad (3.2)$$

with α and γ being the first and the second Townsend coefficients. This equation represents a steady self-sustained current in a critical field $E_c = HV_B/d^*$. The parameter HV_B and d^* is the breakdown voltage and the gap between two planar electrodes with an infinitely large radius, respectively. Theoretical and experimental values of the Townsend coefficients can be found in e.g. Ref. [74] and [75].

The ignition potential, which is equivalent to the breakdown voltage, depends only on the product of the gas pressure P and the distance d^* [76],

$$HV_B = \frac{c_1 \cdot Pd^*}{\ln(c_2 \cdot Pd^*) - \ln(\ln(1 + \gamma^{-1}))}, \quad (3.3)$$

where c_1 and c_2 are determined experimentally and found to be roughly constant over a range of voltages and pressures for any given gas. Lisovski and co-workers [77] measured potential minima in the Paschen curves of argon at a Pd^* value of about 1.1 Torr cm, which is far below the values expected to be achieved in this work. One may make a rough estimate of the expected breakdown voltage according to [76] by taking $c_1 = 84.78 \text{ VPa}^{-1}\text{m}^{-1}$, $c_2 = 7.93 \text{ Pa}^{-1}\text{m}^{-1}$ and $\gamma = 0.068$. For an electrode gap of $d^* = 0.4 \text{ cm}$, the breakdown voltage amounts to 354 V at 40 mbar argon, which represents another limitation of the E/n parameter achievable in the drift region, see also Appendix C.

3.3.3 Choosing a proper extraction nozzle

The background pressures in the detection part of the spectrometer are defined by the buffer gas pressure inside the cell as well as by the nozzle throat diameter. Generally, higher cell pressures and larger orifice diameters are preferred, which result in higher extraction efficiencies of the sample ions. In such cases, however, an efficient pumping of the detection part has to be ensured in order to keep the transit time t_t as small as possible with respect to the drift time of the ions. Otherwise, lower buffer gas pressures and smaller orifices have to be used.

The gas jet at the nozzle

Assuming a steady, isentropic and one-dimensional ideal gas flow, the ambient pressure in the nozzle throat p_1 remains equal to the background pressure in the extraction chamber until $p_1 = p^*$, the critical pressure, which is given by [78]

$$p^* = p_0 \left(\frac{2}{\kappa + 1} \right)^{\frac{\kappa}{\kappa - 1}}, \quad (3.4)$$

with the isentropic exponent κ and the stagnation pressure at the converging nozzle p_0 . Thereafter, further reduction of the background pressure has no influence on the static pressure in the nozzle throat; the latter remains constant at the value $p_1 = p^*$. Taking p_0 equal to the buffer gas pressure inside the cell $P_{cell} = 40$ mbar, the resulting critical pressure amounts to $p^* = 19.5$ mbar, with the isentropic exponent for argon $\kappa = 1.658$ at 298 K. Thus, the ions of interest are extracted from the nozzle in an argon gas jet of supersonic velocities. Remember that the sonic velocity for argon at room temperature amounts to ([78], p. 156) $v^* = \sqrt{\frac{2\kappa RT}{\kappa + 1}} = 276$ m/s with the gas constant for argon $R = 208.15$ Jkg⁻¹K⁻¹.

For an estimation of the mass flow rate Q (in mbar l/s) through the nozzle, one may use the simple expression given by [79]

$$Q = 14.2 \cdot \frac{P_{cell} \cdot d_{Noz}^2}{\sqrt{MT}}, \quad (3.5)$$

with the nozzle throat diameter d_{Noz} in mm, the atomic mass M of the gas in u, the gas pressure P_{cell} in mbar and the gas temperature T in K. Of course, viscosity effects in real gases are not considered here. For two different nozzles of $d_{Noz} = 1$ mm and $d_{Noz} = 0.5$ mm, one gets gas flow rates for $T = 293$ K of about $Q = 5.2$ mbar l/s and $Q = 1.3$ mbar l/s at an argon pressure of 40 mbar, respectively.

The mean free path in the extraction chamber

Usually, the background pressure drastically decreases within the differential pumping section of the spectrometer, and the pressure inside the extraction chamber is the most critical one when seeking shortest transit time t_t of the ions. Therefore, the mean free path of the ions inside that chamber has to be as large as possible. This can be achieved by keeping the background pressure in the extraction chamber below 10^{-1} mbar Ar. According to [80] the mean free path of an ion λ_{ion} in a specific gas is given by

$$\lambda_{ion} = \frac{1}{n\pi(\xi_{gas} + \xi_{ion})^2}, \quad (3.6)$$

with the gas number density n and the collision radii ξ_{gas} and ξ_{ion} of the colliding spherical particles¹. This equation holds as long as the ions move relatively fast, and

¹ ξ_{gas} and ξ_{ion} can be determined by means of viscosity, mobility or X-ray diffraction measurements. They are in the range between 100 pm and 200 pm for most elements of the periodic table [80, 81, 82, 83, 84, 85].

the gas can be considered at rest. Let us assume a Maxwellian velocity distribution of the particles and that the relative movement of the ions and the gas atoms is small in the emerging gas jet inside the extraction chamber; in this case the mean free path decreases to

$$\lambda_{ion} = \frac{1}{\sqrt{2} n \pi (\xi_{gas} + \xi_{ion})^2}. \quad (3.7)$$

In order to get an idea of λ_{ion} , the coarse assumption of comparable collision radii of the particles is made. Hence, the product of both the pressure and the mean free path is taken to be a gas specific parameter [86, 87] at room temperatures, which leads to ([80], p. 611) e.g. $\lambda_{ion} = 6.4 \cdot 10^{-3} \text{mbar cm/P}_{1section} = 0.13 \text{cm}$ for a background pressure of 0.05 mbar inside the extraction chamber. Consequently, the length of the extraction chamber has to be as short as possible.

3.4 Considerations for the detection part

Most sophisticated IMS devices have a mass-selective detection feature for isotope identification or for determining chemical and structural information about molecules. For purposes of mass spectrometry at an accuracy of about one mass unit, a quadrupole mass filter (QMS) represents a rather low-cost system that may be used instead of e.g. magnetic sector mass spectrometers [88]. Since QMS based mass spectrometry becomes possible only if working at high vacuum conditions [89], the extracted ions have to be guided by suitable electric fields through the differential pumping section from the nozzle up to the mass filter installed in the same vacuum chamber where particle detection occurs.

Different methods [90, 91] may be applied for such a purpose. In contrast to the electrostatic lens system used in Ref. [50], the use of a quadrupole ion guide (QPIG) in the differential pumping section allows for

- efficient gas cooling of the extracted ions [67, 73, 92],
- insensitivity to incidence angle of ions into the mass filter [93],
- controlled suppression of background events due to mass dependent transmission efficiency [93].

Hence, using a quadrupole ion guide in conjunction with a QMS in the detection part of the spectrometer promises highest transmission efficiencies [51, 72] of the ions under consideration.

Working principle of quadrupole ion guides and mass filters

The ion guide, like commercially available quadrupole mass filters, is based on the transversal trapping techniques developed by W. Paul in the 1950s [55, 94]. A detailed

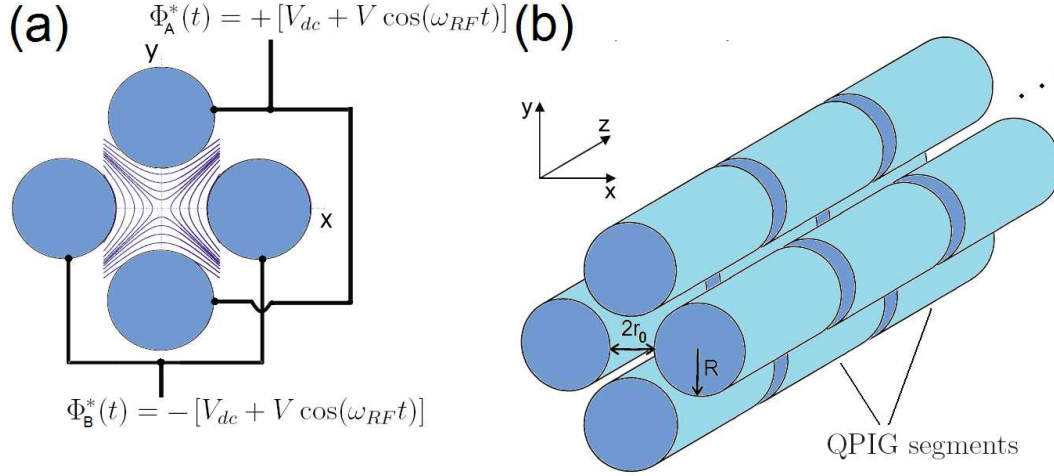


Figure 3.5: (a): The RF voltages applied to the two pairs of a quadrupole ion trap. Also shown are the equipotential lines inside the trap. (b) Geometry of the different quadrupole ion guide segments.

introduction to ion trapping via quadrupolar potentials can be found in Ref. [95]. The simplest quadrupole ion traps consist of two pairs of equidistant and parallel rods as shown in Fig. 3.5. A radio-frequency (RF) voltage Φ^* is applied to opposite rod pairs such that each is 180° out of phase [94] like shown in Fig. 3.5 (a). It is given by a DC voltage V_{dc} and a zero-to-peak voltage V applied with the driving frequency ω_{RF} according to

$$\Phi^*(t) = \pm [V_{dc} + V \cos(\omega_{RF}t)]. \quad (3.8)$$

This potential creates a quadrupole field that alternately focuses in each transverse direction with no axial field component.

In Ref. [96] it is stated that, if circular rods of radius R are used, a good approximation to a quadrupole field and best trapping performance can be obtained when the R/r_0 ratio is equal to 1.145, where r_0 is the radius of the inscribed circle tangential to the inner surface of the rods, see Fig. 3.5 (b).

The operating parameters of such a quadrupole ion trap are governed by the so-called Mathieu parameters a and q , which are defined as

$$a = \frac{8eV_{dc}}{mr_0^2\omega_{RF}^2}, \quad (3.9)$$

$$q = \frac{4eV}{mr_0^2\omega_{RF}^2} \quad (3.10)$$

for singly charged ions of mass m . A mathematical treatment of the ion equation of motion and the calculation of the Mathieu parameters can be found in Ref. [97] and in the references therein.

The ion equation of motion has two types of solution:

1. Stable motion: The ions oscillate transversally with limited amplitudes.
2. Unstable motion: The ions will be lost.

Whether stability exists depends only on the parameters a and q and not e.g. on the velocity of the ions. The operational mode of the quadrupole mass filter is to vary a and q in such a way that only trajectories for the ion mass to be determined are stable. The mass selectivity or mass resolution can be varied by adjusting the a/q ratio to a desired value. For detailed information about quadrupole mass filters, the reader is referred to [55, 97] and the references therein.

In contrast, the ion guide operates at² $a = 0$ and $0 < q < q_{max} = 0.92$ [94] with the consequence that all masses between $\infty > m > m_{min}$ have stable orbits if the ion's charge, V , r_0 and ω_{RF} (see Eq. (3.10)) remain constant. Hence, the QMS can be understood as a narrow band-pass mass filter and the QPIG as a high-pass mass filter with the lowest trapping mass m_{min} .

In order to achieve a guiding effect through the differential pumping section, the QPIG consists of several quadrupole ion traps, the so-called segments “ i_Q ” ($i = 1, 2, 3, \dots$) with continuously decreasing offset potentials U_{i_Q} , see Fig. 3.5 (b). In this way an axial electric field arises, which transmits the transversally trapped ions from the extraction nozzle to the mass filter. The RF voltage of each segment can be expressed as

$$\Phi_{i_Q}(t) = U_{i_Q} \pm V \cos(\omega_{RF}t). \quad (3.11)$$

For a fast transmission of the ions through the quadrupole mass filter, one may need to apply an offset potential U_{QMS} to the QMS rods as well. This leads to the quadrupolar potential for a mass filter

$$\Phi_{QMS}(t) = U_{QMS} \pm [V_{dc} + V \cos(\omega_{RF}t)]. \quad (3.12)$$

Gas cooling inside the extraction chamber

At elevated background pressures inside the differential pumping section, the ions become gradually centered around the axis of symmetry due to collisions with the surrounding gas atoms while traversing the ion guide. This effect, known as buffer gas cooling [98], has the advantage that ions arriving on-axis are efficiently injected into the quadrupole mass filter, thus increasing the transmission of the QPIG.

A simulation of the gas cooling mechanism in the extraction chamber at elevated background pressures can be seen in Fig. 3.6. The $^{215}\text{Po}^+$ trajectories shown there are calculated using the SIMION code [65] and the viscous damping algorithm for gas collisions given in Appendix D.3. The offset potentials of the different QPIG segments

²By setting $V_{dc} = 0$ V in Eq. (3.9).

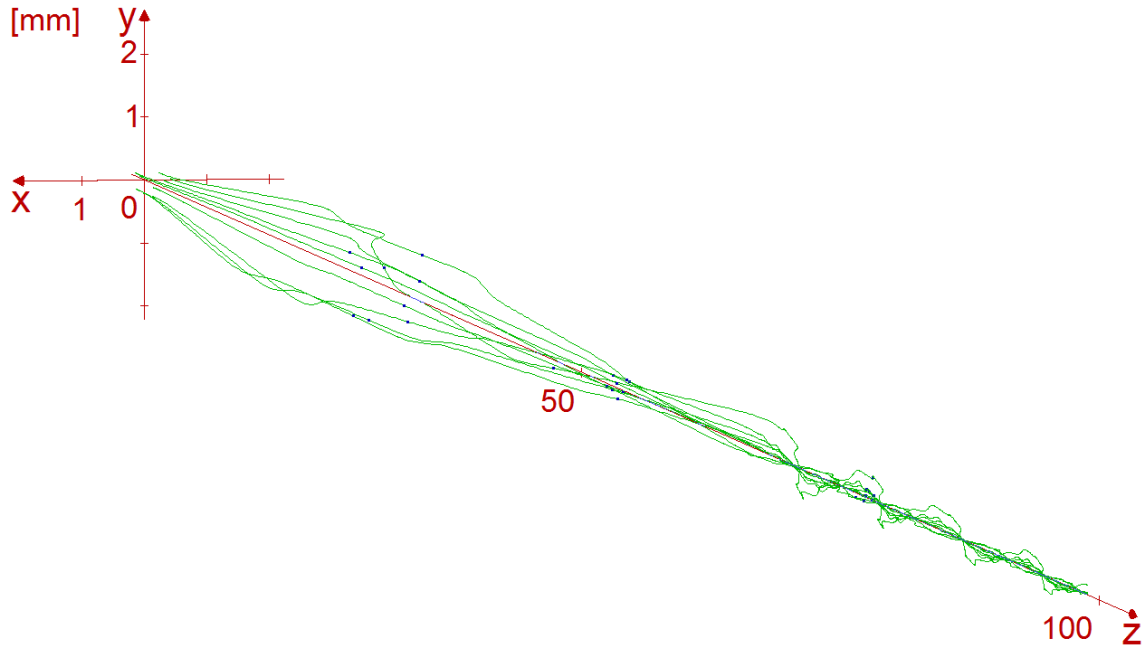


Figure 3.6: SIMION simulation of the gas cooling of $^{215}\text{Po}^+$ ions inside the extraction chamber. The amplitude of the RF voltages is adjusted to 50 V. The ions start 1 mm distant from the nozzle located at the origin of the coordinate system and fly inside a quadrupole ion guide consisting of 6 segments at a guiding electric field of about 8 V/cm along the axis of symmetry. The viscous damping effects implemented in this simulation correspond to a background pressure of $5 \cdot 10^{-2}$ mbar.

result in a guiding field of about 8 V/cm along the axis of symmetry. Of course, the higher the axial field the faster the ions traverse the QPIG. Without a potential gradient between the different segments, the ions would diffuse slowly towards the mass filter, resulting in losses in the overall efficiency as well as in a degradation of the drift time accuracy of the developed apparatus. According to the simulations, most ions are transversally trapped and traverse a distance of 9.7 cm inside the QPIG in less than $40 \mu\text{s}$.

4 The experimental setup

In this chapter, I will introduce the novel ion mobility spectrometer for heavy element research, which has been developed at the University of Munich (LMU). In addition, a laser system used for resonance ionization of the sample atoms and an appendant data acquisition and measurement control system used during this work will be presented.

4.1 The spectrometer

The novel ion mobility spectrometer is sketched in Fig. 4.1. A photograph of the spectrometer is shown in Fig. 4.2. The whole apparatus is fixed on a trolley stand, which provides flexibility concerning possible on-line experiments at the velocity filter SHIP [64]. The IMS apparatus consists of a drift cell and five vacuum chambers, which represent the differential pumping section of the spectrometer. The whole apparatus is pumped out to ultrahigh vacuum pressures using several turbomolecular pumps (TMP) as shown in Fig. 4.1. The drift cell is evacuated using a TMP of 400 l/s pumping speed (type: Pfeiffer, TMU 400M). The latter is decoupled from the cell by a gate valve (type: VAT, DN160) during the mobility measurements, see also Fig. 4.5. In order to drastically decrease the background pressure across the differential pumping section, each of its chambers is separated from the neighboring chambers by a diaphragm of about 3.5 mm inner diameter, thus allowing the use of turbomolecular pumps of low pumping speeds in the differential pumping section. For mass selective detection a commercial quadrupole mass filter (Balzers, QMG 311) in conjunction with a channeltron detector, i.e. a commercial continuous channel electron multiplier (Sjuts, CEM, KBL 15RS) [99] is used. The QMS is equipped with a deflector, with which filtered ions are deflected by 90 degrees before they are focused by an electrostatic lens system onto the detector (see Fig. 4.1). According to the QMS manufacturer, such an operation mode of the quadrupole mass filter allows for highest sensitivities to the desired charge-to-mass ratios. For a proper use of the mass filter and the detector, pressures less than 10^{-5} mbar are required [89] in the so-called detection chamber where both components are installed. Elevated pressures there may destroy the channeltron detector and cause gas discharges between the rods of the mass filter operated at high voltages.

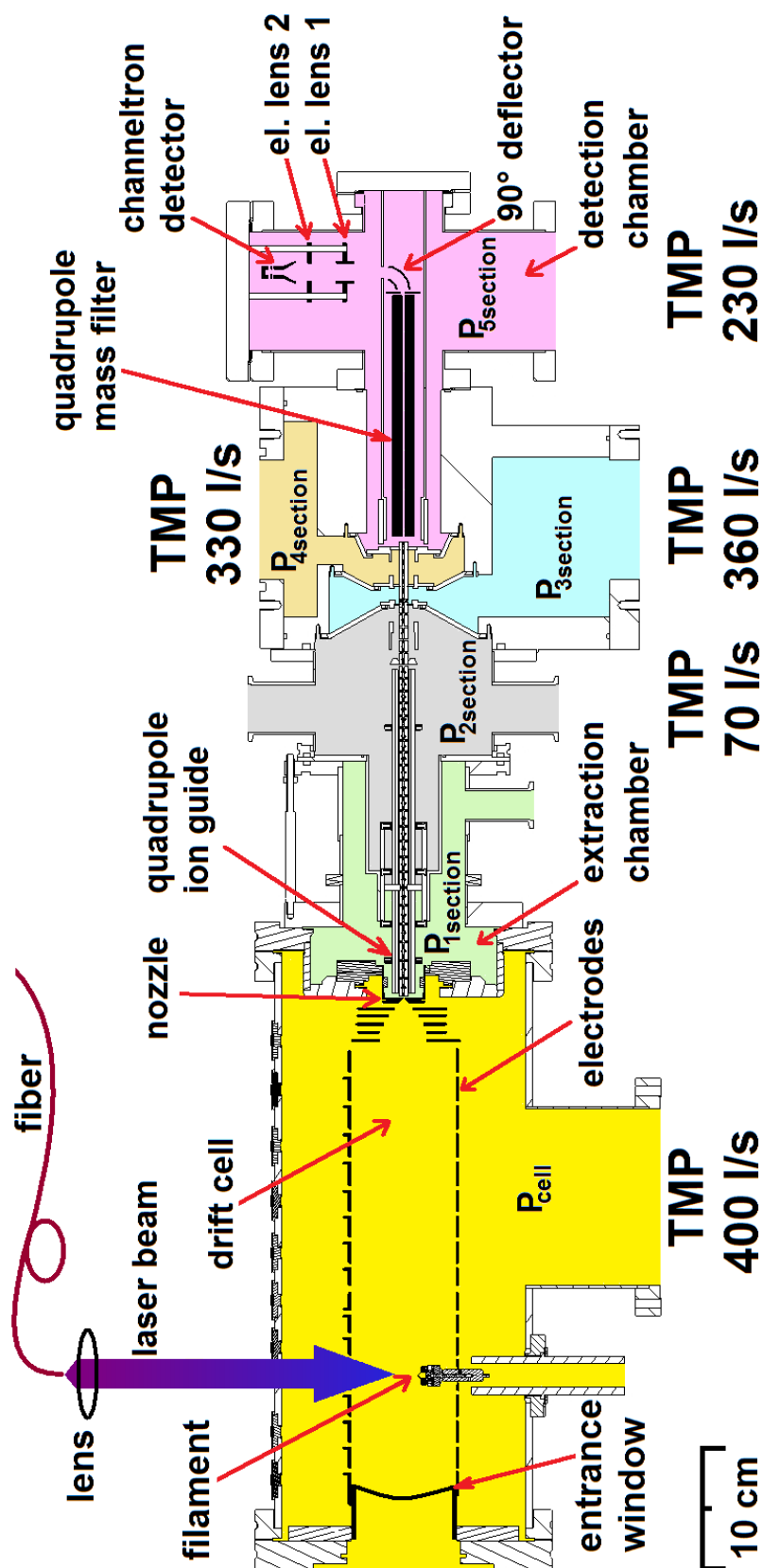


Figure 4.1: Schematic view of the novel ion mobility spectrometer.

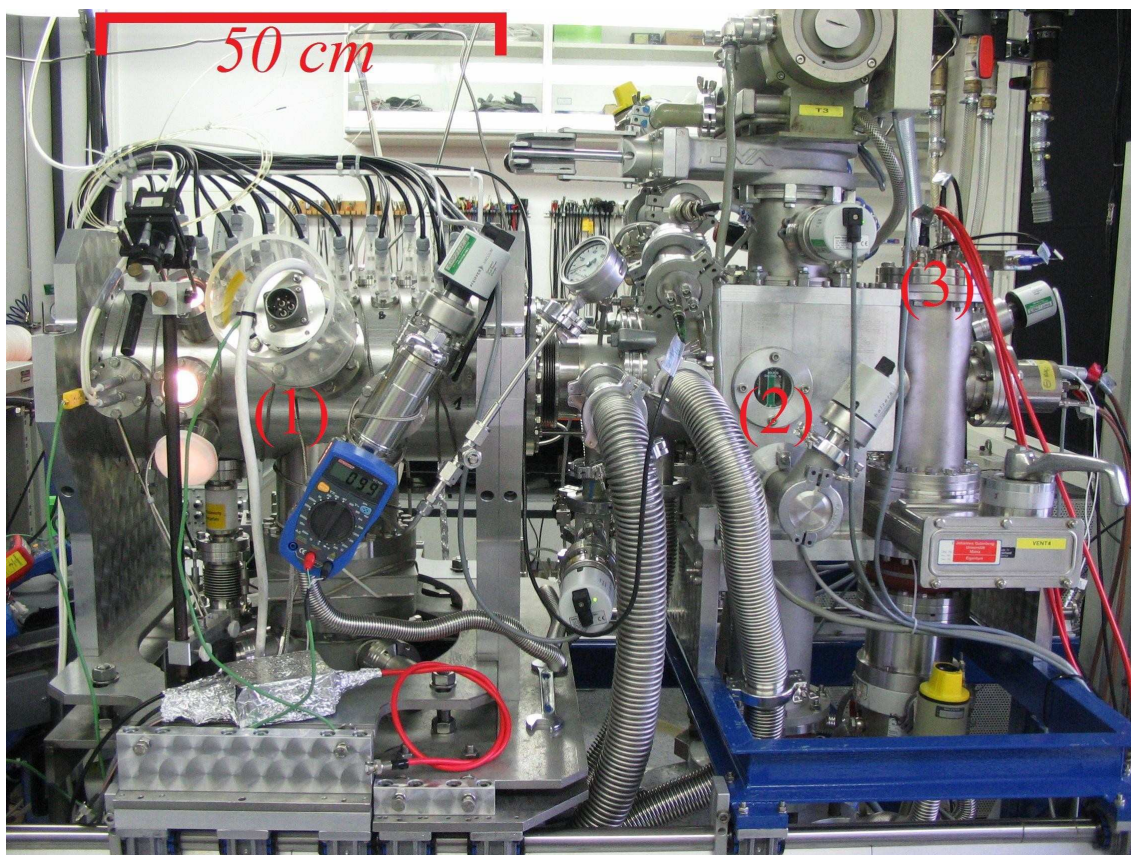


Figure 4.2: Photograph of the novel IMS apparatus. (1)- The drift cell, (2)- The differential pumping section, (3)- The channeltron housing.

When considering the uncertainty of the arrival time distributions, the most critical background pressure is that inside the extraction chamber. A detailed discussion of this issue is provided in Sect. 6.4. For lowest pressures in this chamber, one may use high-performance turbomolecular pumps. Unfortunately, such a concept could not be realized due to geometrical and time restrictions. Nevertheless, during operation, the mentioned turbomolecular pump of 400 l/s pumping speed is used to evacuate this first pumping section. The second pumping section, i.e. the neighboring vacuum chamber, is evacuated using the same TMP assisted by another TMP (Varian, TV 70LP) of 70 l/s pumping speed. Both pumps are connected to their associated vacuum chambers by several KF40 and KF25 bellows. The rest of the detection part is efficiently evacuated using other TMPs of different pumping speeds, ranging between 230 l/s up to 360 l/s as shown in Fig. 4.1.

In the following, the drift cell of the spectrometer and the used quadrupole ion guide will be described in detail. Details on the detection chamber containing the mass filter and the channeltron detector can be found in Ref. [50, 51, 100] and will not be discussed at this point.

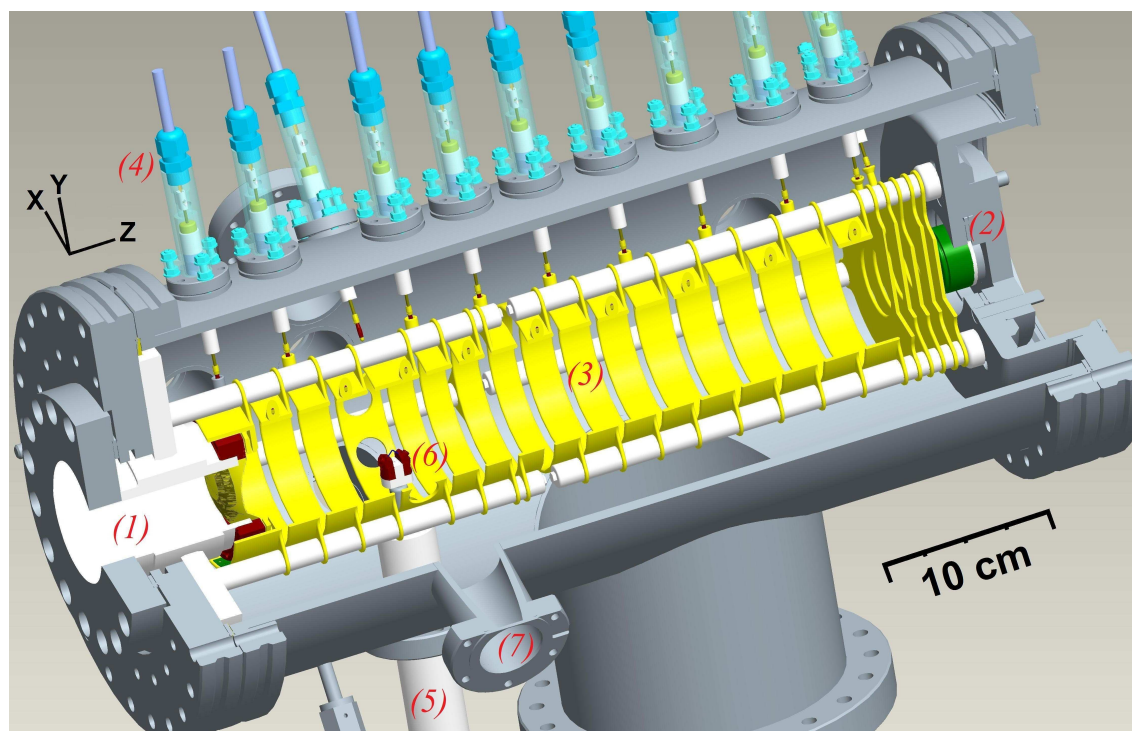


Figure 4.3: Cross-section plot of the drift cell. The main components of the cell are: (1)- CF-63 entrance window flange with an electrical insulator, (2)- CF-63 nozzle flange, (3)- Drift electrodes, (4)- Custom-made electrical feedthroughs, (5)- Ceramic insulator tube for filament mounting, (6)- Catcher/filament mounting, (7)- Fused silica window (six windows in total) for laser resonance ionization purposes.

4.1.1 The drift cell

As mentioned in Sect. 4.1.1, highest gas purities are required inside the drift cell in order to suppress chemical reactions of the sample ions during their drift, see Sect. 7.1.1. Therefore, the cell is made of stainless steel and is equipped exclusively with CF flanges. This feature allows for high baking temperatures of up to 250 °C. For baking purposes, two halogen lamps (type: Osram, 24V, 250 Watt each) are installed inside the drift cell. Several heating tapes (type: Tyco Thermal Controls, KTeS, 100 Watt each) are wrapped around the cell for the same purpose. The heat dissipation of the lamps and the tapes is exploited to evaporate most of the impurities and water molecules on the walls of the cell. The baking procedure is necessary each time the cell is exposed to air conditions and takes place for one day at high vacuum conditions before performing mobility measurements. The cell is evacuated by a turbomolecular pump as shown in Fig. 4.1 coupled to a piston vacuum pump (type: Oerlikon-Leybold, EcoDry M15, 15 m³/h), see also Fig. 4.5.

Table 4.1: Geometry chosen for the electrodes near the nozzle. The inner electrode gaps indicate the separation of each electrode from its neighboring one on the nozzle side. All values are in mm.

Electrodes:	#6	#5	#4	#3	#2	#1
Width:	20	2	2	2	2	2
Inner \varnothing :	90	40	40	34	26	16
Inner electrode gaps:	6	5	5	5	4	4

The drift cell consists of 22 ring electrodes, a nozzle and an entrance window foreseen for on-line experiments. The entrance window is electrically isolated from the ground potential of the cell by a ceramic insulator (VITRONIT®) of 40 mm length and 64 mm inner diameter. However, no entrance window is needed for the performed off-line measurements and therefore is left out so far. The drift region has a total length of 420 mm. The ring electrodes are machined from stainless steel and subsequently have been electropolished to minimize the risk of gas discharges inside the cell. A nested construction of stainless steel rods and ceramic insulators fixes the electrodes on the front as well as on the rear side of the cell as shown in Fig. 4.3. The electrodes are divided into two groups that are fixed independently from each other for easy mounting purposes. At the beginning of the drift path the ring electrodes have an inner diameter of 90 mm in order to contain the stopping volume of the reaction products inside the drift cell. The electrodes near the extraction nozzle, the focusing electrodes, are characterized by a decreasing inner diameter for the electrostatic focusing mechanism described in Sect. 3.3.2. The geometrical constraints chosen for these electrodes are shown in Tab. 4.1.

The nozzle is exchangeable and allows for gas flow adjustment at a desired cell pressure. Two converging nozzles of a throat diameter $d_{Noz} = 1$ mm and $d_{Noz} = 0.5$ mm can be installed. Both are 4 mm thick and exhibit a cone of 90 degree angle. Just like the entrance window, the nozzle is electrically isolated from the cell housing and can be operated at voltages of < 250 V. Six fused silica windows for ionization using laser beams are placed around the stopping volume and a linear actuator for a filament mounting is foreseen (see Fig. 4.3).

Specially designed electric feedthroughs allow to apply the necessary high voltages to the different electrodes. Their design is shown in Fig. 4.4. The feedthroughs are easily connected to the corresponding drift electrodes by using banana plugs. Their effective insulation length with respect to the grounded cell housing amounts to 3 cm. According to the breakdown voltage considerations presented in Sect. 3.3.2, this insulation length theoretically allows to apply highest drift potentials of more than 4 kV at 100 mbar argon.

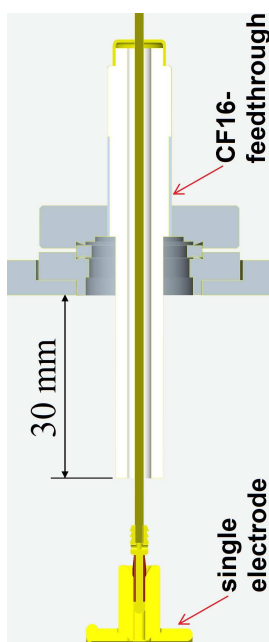


Figure 4.4: The specially designed electric CF16-feedthrough.

4.1.2 The gas supply system

Argon¹ 6.0 is used as a buffer gas and is admitted to the drift cell through a fine-dosing valve, see Fig. 4.5. Gas impurities, especially oxygen and water molecules, may allow for chemical bonds and charge exchange reactions of the ion species and thus may hamper the extraction efficiency of the apparatus. Hence, the buffer gas is further purified by a gas getter system (SAES, model PS4-MT3-R-2) before entering the cell. Exclusively stainless steel gas tubes of 1/4" diameter are used for the supply system. The drift cell is equipped with a residual gas analyzer (RGA) (Leybold Inficon, type TSP TH200) for controlling gas impurities and with a getter pump (SAES, SORB-AC, St 707) containing a getter alloy that is fully activated in the temperature range between 400 °C and 500 °C [103]. A gate valve separates the cell from the turbomolecular pump, which is exploited to evacuate the extraction chamber during operation. A compact capacitance gauge (Pfeiffer, CMR 261) with the corresponding operating and display unit (Pfeiffer, TPG 256A) is used for pressure control. The cell pressure can be registered and regulated up to a level of $5 \cdot 10^{-2}$ mbar at 40 mbar argon.

4.1.3 The quadrupole ion guide

During mobility measurements, the extracted ions are transversally trapped and gas cooled [67] inside the QPIG. The ion guide is installed only 1 mm in front of the

¹The number 6.0 stands for an impurity level less than 1 ppm. The impurity concentrations in the used argon gas can be found in Ref. [101, 102].

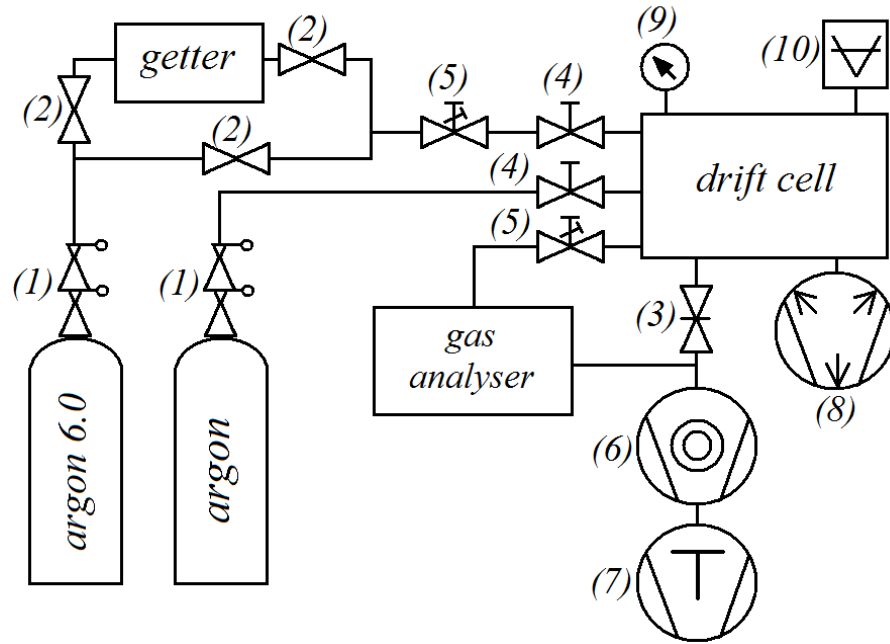


Figure 4.5: Gas supply system of the drift cell. Argon of highest purity level is used as a buffer gas in the mobility experiments. The main components of the gas system are: (1)- Pressure regulators, (2)- Valves, (3)- Gate valve, (4)- Through valves, (5)- Fine-dosing valves, (6)- Turbomolecular pump, (7)- Piston vacuum pump, (8)- Getter pump, (9)- Manometer, (10)- Capacitance gauge, operating and display unit for pressure control. The gas getter as well as the getter pump are used for additional gas purification purposes.

extraction nozzle and disemboques into the mass filter inside the detection chamber. It consists of 28 segments in total and has a length of nearly 38 cm. One part of the used QPIG is shown in Fig. 4.6. Due to geometrical constraints, a less efficient R/r_0 ratio of 0.857 for ion trapping has been achieved. All QPIG rods are made out of brass and have a 3 mm diameter. They are mounted on ceramic bars of 6 mm x 8 mm geometry as shown in Fig. 4.6. The first six segments inside the extraction chamber are 15 mm long and disemboque into the next vacuum chamber containing eight segments of 12 mm and thirteen of 10 mm length. The last segment is about 50 mm long and spans the other vacuum chambers until arriving at the quadrupole mass filter. Diaphragms out of machineable glass ceramics (VITRONIT®) with an inner diameter of about 3.5 mm are used to separate the different vacuum chambers from each other as well as to fix the QPIG inside the differential pumping section. A description of the geometry of the used diaphragms can be found in Ref. [93]. Both the ceramic bars and the diaphragms are coated with a highly resistive layer [99] in order to avoid electrostatic charging on the ceramic surfaces, which may distort the quadrupolar potentials. The electric resistance

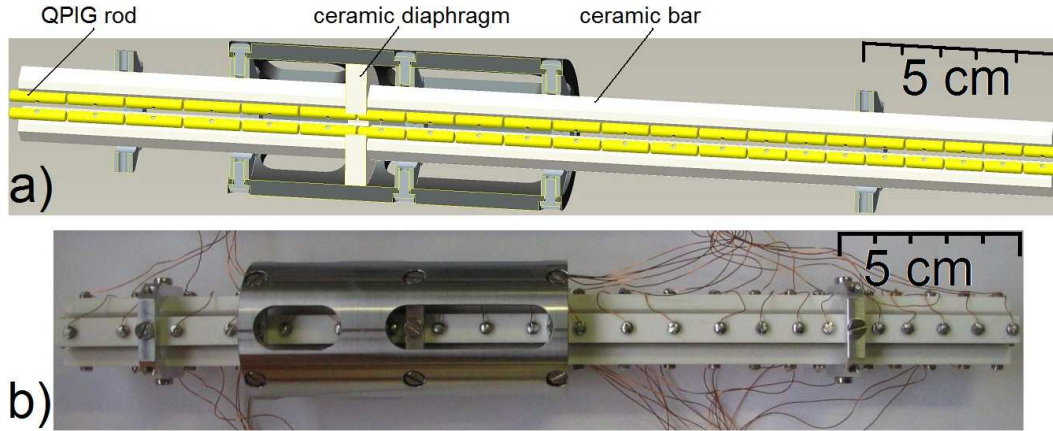


Figure 4.6: (a) The design of the quadrupole ion guide. Only its first 22 segments are shown in this plot. (b) Photograph of one part of the QPIG used in the differential pumping section.

amounts to $> 5 \text{ M}\Omega$ for gaps of 0.5 mm between the neighboring QPIG segments and more than $40 \text{ M}\Omega$ from any QPIG segment to ground.

Figure 4.7 shows the configuration and the electric circuitry with which RF voltages of all QPIG segments are provided. A signal generator (Marconi, type: 2023) coupled to a wide-band RF power amplifier (ENI, model 240L) feeds an RF distributor module with a sinusoidal unipolar voltage of 1.95 MHz frequency and variable amplitudes. Using an induction coil, two bipolar RF voltages, phase *A* and phase *B*, which are 180° phase-shifted to each other with amplitudes of up to 250 V_{pp}^2 , can be achieved in this configuration. They are coupled to the corresponding QPIG segments by a capacitance of $2.2 \mu\text{F}$. Two test-outputs are also foreseen to control and check the resonance frequency of the electric circuit. The offset voltages U_{i_Q} of the different QPIG segments are added to the radio frequency voltages in the distributor module according to the electric circuit shown in Fig. 4.7 (b).

Even though the QPIG and the QMS work independently, they are operated at the same RF frequency of 1.95 MHz. Unsynchronized driver frequencies of both tools, however, are supposed not to strongly affect the efficiency of the apparatus, especially because all ions are gas cooled at the axis of symmetry before getting injected into the mass filter [93].

²Given here is the peak-peak voltage, which is twice the voltage V described in Eq. (3.10).

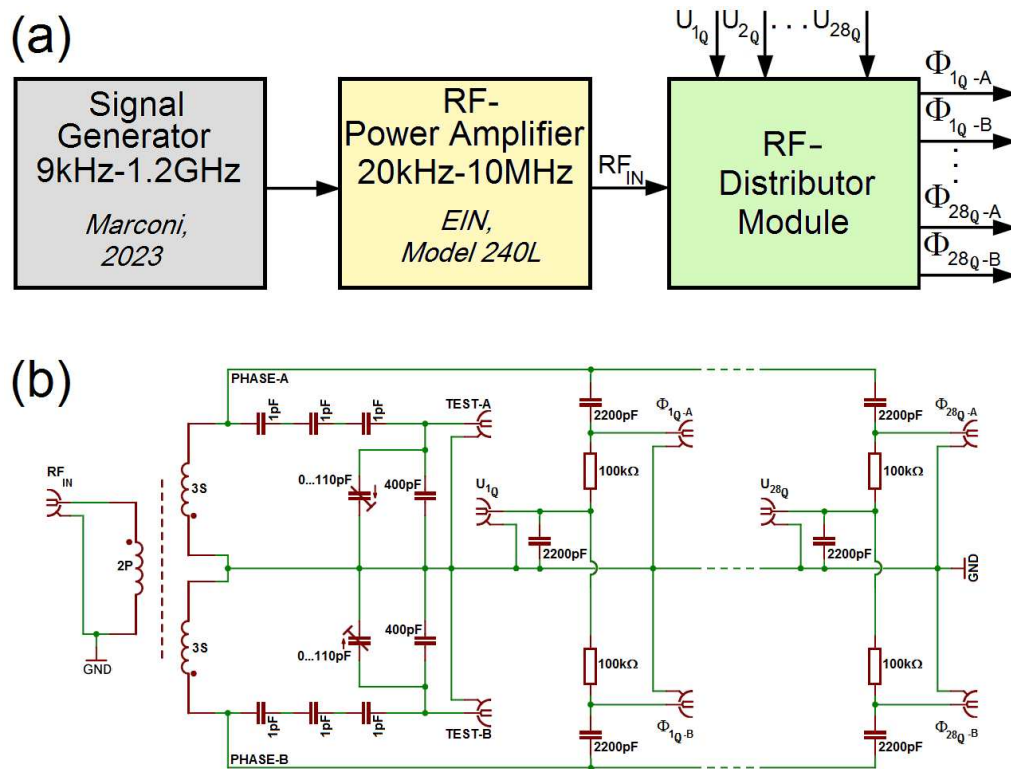


Figure 4.7: The configuration (a) and the electric circuitry (b) used to supply the quadrupole ion guide with RF voltages.

4.2 The laser system

For element-selective laser ionization of sample atoms, an excimer-pumped dye laser system is used. It allows for the two-step photoionization process described in Sect. 3.2. The first excitation step is provided by a tunable dye laser (Lambda Physik, FL 2001). The second step, which leads to ionization of the atoms, is achieved by an excimer laser (Lambda Physik, EMG MSC 103) operated with a XeF gas mixture [104]. The dominant wavelengths provided by the excimer laser are 351 nm and 353 nm. A complete lasing spectrum of this laser can be found in e.g. [105]. Figure 4.8 shows the laser system, which is operated between 10 and 200 Hz. For the mobility measurements carried out in this work, the repetition rate is computer controlled and fixed at 20 Hz, see Sect. 4.3 for more details. At this repetition rate the energy per single shot provided by the excimer laser is about 30 mJ for pulses of about 15 ns duration.

The pumped dye laser is operated almost in the blue range. The diversity of suitable excitation schemes for the different elements of interest (lanthanides) requires the use of different dyes as listed in Tab. 4.2. The used dye concentration in the corresponding solvents as well as the grating order O_g and the onboard step counter N_{st} at which the

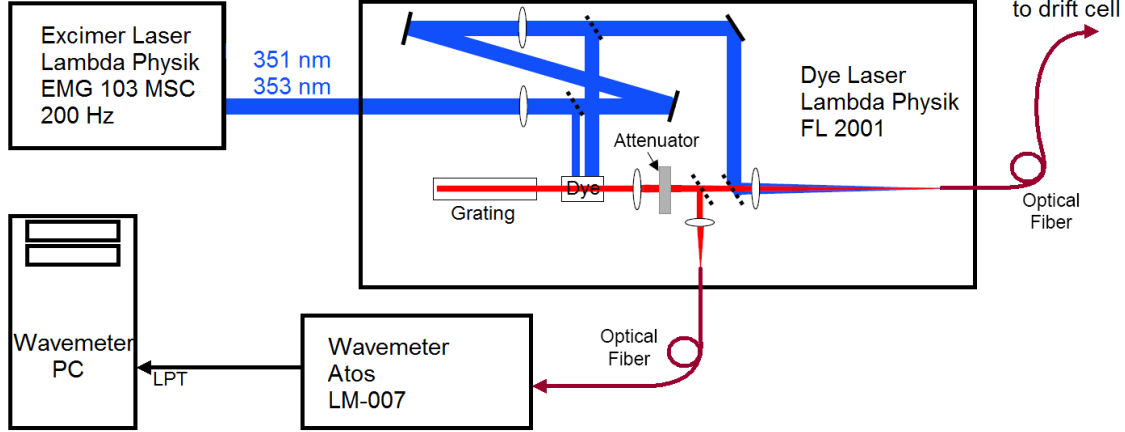


Figure 4.8: The excimer-pumped dye laser system used in the IMS experiment. Both excitation laser beams are coupled into one glass fiber and guided to the drift cell. Another fiber transmits a small fraction of the dye laser light to a wavemeter, which determines the adjusted wavelengths.

Table 4.2: Dye laser parameters used for atomic excitations of certain lanthanides. The numbers N_{st} are easily converted into wavelengths according to Eq. (4.1).

Element	Dye	Concentration [g/l]	Solvent	O_g	N_{st}
Eu	Coumarin 2	0.22	Methanol	6	5510.00
Gd	Coumarin 2	0.22	Methanol	6	5485.88
Tb	Coumarin 2	0.22	Methanol	7	6054.45
Dy	Coumarin 2	0.22	Methanol	6	5490.10
Ho	Exalite 398	0.3	Dioxan	7	5672.65
Er	Exalite 398	0.3	Dioxan	7	5608.49
Yb	Exalite 398	0.3	Dioxan	7	5580.21

desired first excitation step occurs are also shown in the table. A fast and easy way to check the adjusted excitation wavelengths is provided by the relation

$$\lambda_{12} = \frac{N_{st}}{2 \cdot O_g}. \quad (4.1)$$

Depending on the grating order and the lasing wavelengths, the bandwidth of the dye laser is in the range between 5 and 10 GHz [106]. The pulse energies are in the order of 1 mJ. The control program presented in Appendix B.2 allows for tuning the dye laser and finding suitable resonances for photoionization of the sample atoms. The smallest scan steps in that case amount to $0.0042 \text{ nm}/O_g$.

For simplicity's sake, both laser beams are coupled into one 12 m long multi-mode silica glass fiber of $500 \mu\text{m}$ diameter and guided to the IMS experimental setup as shown in Fig. 4.8 and Fig. 4.1. The inefficient coupling mechanism reduces the pulse energies

of the excimer and the dye laser at the end of the fiber to $< 600 \mu\text{J}$ and $< 300 \mu\text{J}$, respectively. Using a biconvex lens of 5 cm focal length and a variable diaphragm, laser beams of 1 to 10 mm diameter can be adjusted. The timing overlap of the different laser wavelengths³ is still guaranteed in spite of different refraction indices [51]. Inside the cell, the ionization volume is mainly determined by the density distribution of evaporated sample atoms above the filament and the parallel laser beams crossing this volume such that both essential quantities for IMS measurements, namely the ion starting position z_0 and time t_0 of each ion, are very well known (see also Fig. 3.3 (c)).

Using a glass plate, a small fraction of the dye laser light is transmitted with a single mode fiber to a wavemeter (Atos, LM-007) [107], which determines the currently adjusted wavelengths with an accuracy of about 0.042 cm^{-1} . The wavemeter is read out by the parallel port of a PC dedicated only for this purpose.

4.3 Signal processing, data acquisition and measurement control system

4.3.1 The data acquisition system

During mobility measurements, several digital and analog signals need to be managed and processed simultaneously such that a listmode data acquisition (DAQ) system is mandatory. Another challenging issue in time critical applications is the synchronization of trigger signals and the proper assignment of the time stamps to each registered event. For that purpose a field-programmable gate array (FPGA) based DAQ system (National Instruments, NI PXI 7833R), which is read out and controlled by a personal computer (PC), has been chosen. Due to the complexity of the developed apparatus, all analog and digital I/O's of this DAQ system are reconfigurable with the National Instruments LabVIEW FPGA module; so later modifications in the signal processing structure remain possible [108].

The behavior of the device is user-defined, providing capabilities such as:

- Complete control over synchronization and timing of all signals and operations within 25 ns time resolution.
- Onboard decision making and triggering.
- Ability to individually configure digital lines as inputs, outputs, counters/timers, pulse-width modulators, flexible encoder inputs or user-defined communication protocols.
- Simultaneous analog input up to 200 kHz and simultaneous analog output up to 1 MHz.

³Eq. (A.4) in Appendix A.1 requires both lasers to coincide within a time much smaller than the relaxation time of the excited state.

The key features of this DAQ system are listed in Tab. 4.3. A NI-VISA server is used for communication between the remote PXI 7833R and the host computer, which interprets the DAQ system as a locally installed VISA device. See Appendix B.2 for details on the developed data acquisition software for mobility measurements.

Table 4.3: Key features of the used FPGA-based data acquisition system with reconfigurable I/O's (Ni 7833R).

Bus type	PXI
Clock frequency	40 MHz
Digital I/O	96
Analog inputs	8 (± 10 V)
Analog outputs	8 (± 10 V)
I/O resolution	16bit
Sampling rate	200 kHz/channel
Operating system	Windows 2000/XP
DAQ software	LabVIEW based

4.3.2 Measurement control system during mobility experiments

Using the DAQ system described above, several modules needed for mobility measurements realized in this work could be simultaneously controlled and read out. The corresponding block diagram is shown in Fig. 4.9.

The gas analyzer (Leybold Inficon, type: TSP TH200) in this figure allows for monitoring residual impurities inside the drift cell before doing any mobility measurements. This unit is controlled by a serial communication port using the manufacturer software TranspectorWareTM [109]. Another PC serial interface is dedicated for monitoring the buffer gas pressure inside the drift cell during mobility measurements. The pressure is registered each time a run for data acquisition is started, see also Appendix B.2. Further details on the pressure monitoring system can be found in Sect. 4.1.2.

The filament as well as the electrode potentials are provided by two HV modules (iseg, type EHQ F030p and EHS F030p) with 16 channels each. Voltages up to +3 kV with an accuracy of ± 0.6 V and a maximum current up to 2 mA per channel can be applied. The iseg modules can be accessed using a CAN bus communication port, which is connected to the host computer via an USB-CAN converter (manufacturer: Peak), see Appendix B.1 for further details.

Element-selective laser resonance ionization techniques described in Sect. 3.2 and Sect. 6.1 are used to create monoatomic ions of interest inside the cell. For that purpose, the excimer laser is controlled and synchronized during its operation with a TTL pulse created by the DAQ system. This signal is converted to a 15 V pulse of 10 μ s width that triggers the laser and defines the moment at which the measurement

time is reset to $t = t_0 = 0$. If needed, other trigger signals can be used to control the excimer-pumped dye laser, which provides excitation wavelengths of atoms under test. The grating of the dye laser is tilted in steps defined by a TTL pulse in a direction determined by a DC voltage of digital amplitudes, both provided by the same DAQ module (see Fig. 4.9).

The control unit (Balzers, QMG 311) allows to externally manipulate the RF potentials of the quadrupole mass filter such that only ions of the desired e/m ratio are transmitted. Ion masses up to 300 u can be selected by setting the corresponding DC potentials from 0 V to 10 V onto a proper connector on the rear panel of this unit. During mass scans, see Appendix B.2, the lowest mass resolution achievable is software limited to 0.1 u. The adjusted ion mass is delivered by the same control unit as a corresponding DC voltage between 0 V and 10 V at another rear panel connector and is read out with 16 bit resolution by the PXI 7833R module.

Each ion that hits the channeltron active surface produces an inverted signal on the 18 nF capacitance coupled to the detector. The produced signals are in the 100 mV range and last less than 10 ns. By using a constant fraction discriminator (Canberra, type: 1428A), each ion signal is converted into a standard NIM signal of 1 μ s width that defines the stop time of the time counter inside the DAQ module. The same NIM signal is also used by a ratemeter (Ortec, model: 661) to visualize the event rates registered by the detector.

For transit time measurements (see Sect. 6.4), the nozzle potential can be triggered using a Fast HV Push-Pull Switch (Behlke, type HTS 151-30-GSM) coupled to two high voltage modules (FUG, type HCE 7-6500 and HCE 35-6500). The DAQ system mentioned before generates a suitable TTL pulse for that purpose and synchronously resets the time counter at the beginning of each triggering cycle. During mobility measurements, however, this trigger option is disabled and the nozzle potential remains constant at only one value. In this case, the static potential of the nozzle can be provided by the same iseg HV modules described before.

4.3.3 Signal processing during extraction efficiency measurements

The same PXI module mentioned before is also used for the extraction efficiency and drift time measurements described in Sect. 5.1. A schematic view of signal processing during these experiments is shown in Fig. 4.10. In these experiments α decays are registered using a bare silicon photodiode. The diode signals are amplified by a charge sensitive preamplifier (Canberra 2004) such that the resulting pulse amplitude is proportional to the total charge created in the initial ionizing event. The preamplifier conversion factor amounts to 9 mV/MeV. In a next step the pulse is shaped using a spectroscopy amplifier (Ortec 451) with a total gain of 119. For better noise and pile-up suppression the shaping time is fixed at 2 μ s [110]. Subsequently, a peak-detector developed by the electronic workshop at the University of Munich in Garching is used as a linear gate and stretcher. It accepts pulses in the range from 0.01 V to 10 V and

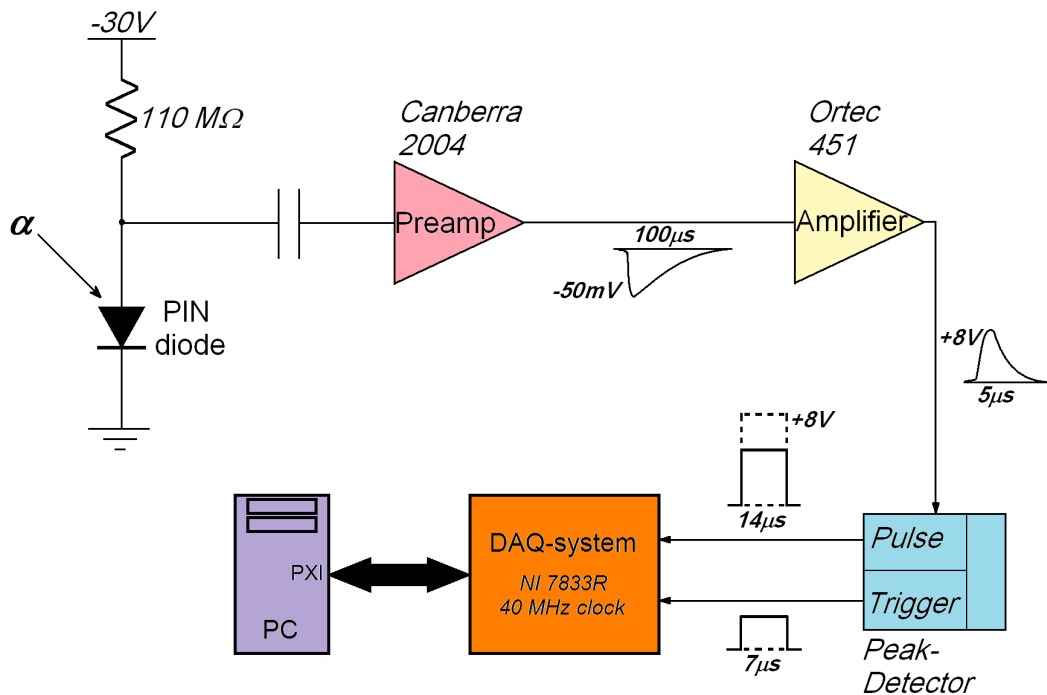


Figure 4.10: Block diagram of the data acquisition system used for the extraction efficiency and drift time measurements described in Sect. 5.1.

generates an analog output level with equal amplitude and a TTL norm trigger. The rise time of the analog level is $< 1 \mu s$ and its width is adjustable in a range $< 100 \mu s$. The distortion of the energy resolution due to pulse stretching is less than $< 0.4\%$ of the input pulse. The such obtained signal is digitized using the already introduced FPGA-based data acquisition system, which in conjunction with the developed list-mode DAQ software (see Appendix B.2) allows to register α decays both energy and time resolved.

5 Preparatory experiments

Extensive test experiments are carried out in order to optimize the spectrometer for the envisaged mobility measurements in the lanthanide region. At first, the drift cell has been separately tested using a radioactive recoil source. Subsequently, it has been coupled to the detection part for which best suited guiding potentials have been extracted. A rough estimation of the overall efficiency of the apparatus is then given at the end of this chapter.

5.1 Extraction efficiency measurements employing a ^{223}Ra recoil source

Especially for on-line experiments or if dealing with sub-microgram quantities of the sample elements, the most critical parameter of the IMS apparatus that has to be considered is the detection efficiency. Online experiments with trace amounts of short-lived superheavy elements become only feasible and realistic if an overall efficiency of $\gtrsim 1\%$ is guaranteed [49]. In the following, test experiments using a ^{223}Ra recoil source for determining the extraction efficiency of the drift cell will be presented.

5.1.1 The ^{223}Ra recoil source

Extensive tests are carried out in order to investigate the influence of the drift cell potentials and the gas flow at the nozzle on the extraction efficiency of heavy ions. Using a radioactive ^{223}Ra recoil source inside the cell may be the simplest method for doing that. This source is proved to be best suited for such experiments, since it allows for detecting recoiled ions after their extraction at the nozzle. The decay scheme of the ^{223}Ra isotope is shown in Fig. 5.1. Further details on the recoil source and how it is constructed and bred can be found in Ref. [50].

First of all, the α spectrum of the source is registered in vacuum ($\sim 10^{-6}$ mbar) with a bare silicon PIN-photodiode (Hamamatsu, S3590-19, (10×10) mm²) at a distance of 40 mm from the ^{223}Ra source. A diaphragm of 5 mm diameter is fixed at the surface of the PIN diode in order to achieve a better α energy resolution. The diode signals are acquired and analyzed as described in Sect. 4.3.3. In vacuum measurements, only the sum of the registered events and their corresponding energies are important. At a reverse-biasing of 30 V the energy resolution of the used PIN-photodiode amounts

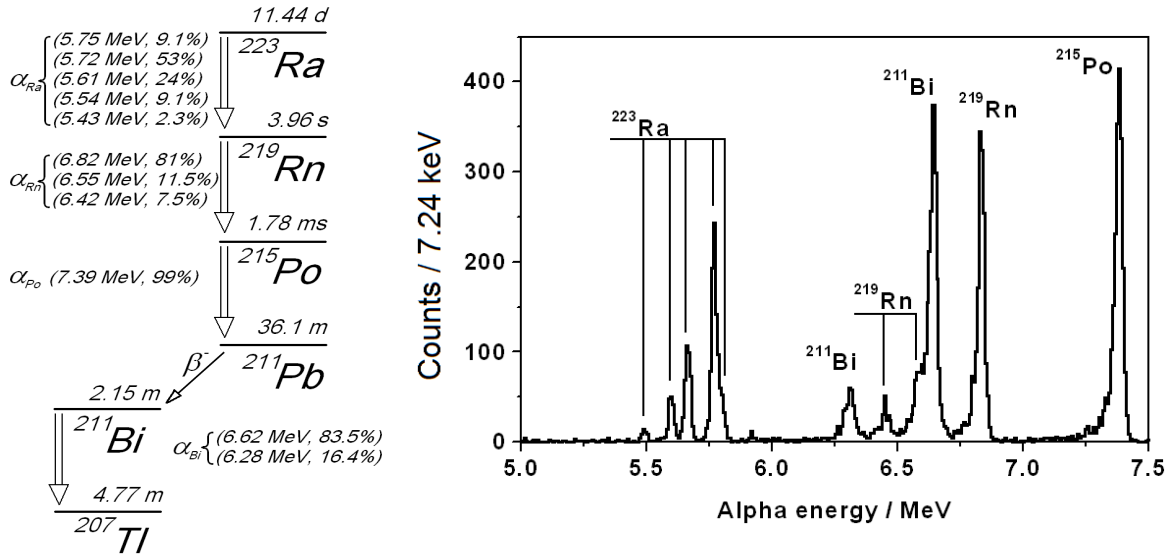


Figure 5.1: Recoil ion source. Left: Decay chain. Only dominant lines are listed. Right: Corresponding α energy spectrum (in vacuum) registered with the data acquisition system shown in Fig. 4.10 and the software described in Appendix B.2.

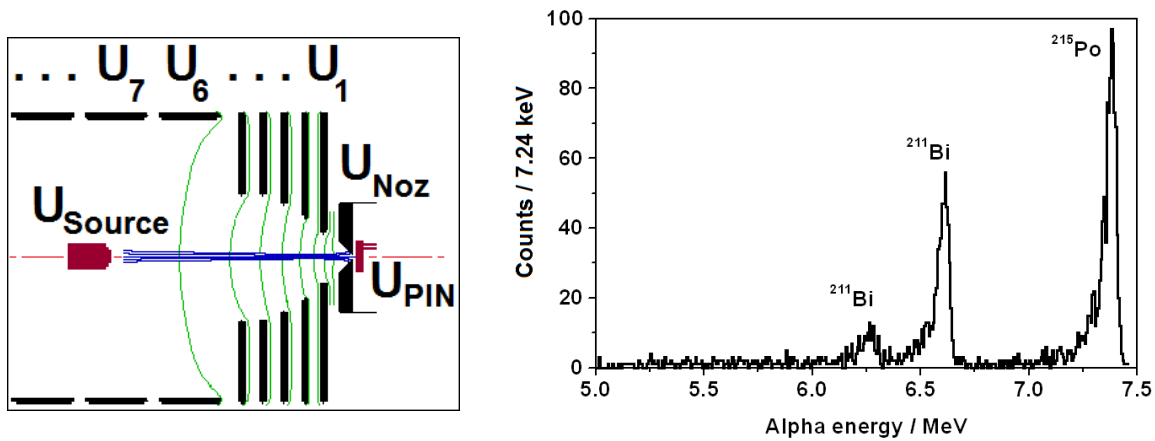


Figure 5.2: Left: Trajectories of $^{215}\text{Po}^+$ ions drifting inside the buffer gas cell. Right: Decay energy spectrum of the extracted recoil ions at a buffer gas pressure of 20 mbar. In this case, the source is placed at the centerline of the drift cell at a source-nozzle distance of $d_{\text{SN}} = 79$ mm.

Table 5.1: HV potentials used for the extraction efficiency measurements. The remaining electrode potentials are fixed at 404 V, see Fig. 5.2. The potential U_{PIN} and U_{Noz} is the potential of the detector and of the nozzle, respectively. The potential U_{Source} stands for the potential of the ^{223}Ra source.

$U_7[\text{V}]$	$U_6[\text{V}]$	$U_5[\text{V}]$	$U_4[\text{V}]$	$U_3[\text{V}]$	$U_2[\text{V}]$	$U_1[\text{V}]$	$U_{Noz}[\text{V}]$	$U_{PIN}[\text{V}]$
324	284	244	204	160	108	52	16	0

to $\Delta E_\alpha \approx 28 \text{ keV}$ (FWHM). The characteristic energy spectrum obtained is shown in Fig. 5.1. Afterwards, the source is mounted at the central axis of the drift cell at a variable distance d_{SN} from the extraction nozzle (see left panel of Fig. 5.2). The radioactive daughter isotopes recoiling out of the source are stopped as singly charged ions in the argon buffer gas at a pressure of about 60 mbar and are guided by a suitable electric field towards the nozzle. After extraction, the ions are deposited onto a PIN diode, which now is placed 1 mm behind the nozzle. The number of deposited ions is detected via their subsequent α decay. Figure 5.2 (right) shows a typical α energy spectrum of the extracted recoil ions. Only the ^{223}Ra daughter isotopes appear in the spectrum, since no direct α particles can reach the detector. The absence of the ^{219}Rn peaks is attributed to the noble gas properties of this element, which does not stick on the detector surface. Due to its short half-life $t_{1/2}^{\text{Po}} = 1.78 \text{ ms}$ all measurements are performed with ^{215}Po , the second decay daughter of ^{223}Ra .

5.1.2 Optimization of the source potential

Initially, electrode potentials are chosen, which are 2/3 smaller than those used for mobility measurements (Tab. 3.2) minus an offset of 68 V. The resulting potential configuration is listed Tab. 5.1. Higher electrode potentials could not be applied in the extraction efficiency experiments due to the absence of suitable electric feedthroughs at that time. Nevertheless, this potential configuration results in ion trajectories comparable to the Po^+ trajectories shown in Fig. 3.3 (a). At a suitable source potential and small drift distances, the recoiling ^{215}Po ions can be efficiently extracted and detected.

Figure 5.3 shows the rate of extracted ^{215}Po ions as a function of the source voltage. If the source potential U_{Source} is set below the potential of the surrounding electrode ($U_2 = 108 \text{ V}$), all recoil ions are guided back onto the source. Increasing U_{Source} results in an increase of the registered ^{215}Po rate, which has its optimum at about 118 V. Further increase of the source potential causes a decrease of the ^{215}Po rate due to the high radial velocities of the ions inside the nozzle cone. After fixing the source voltage, the potentials applied to all electrodes may be optimized in an iterative way. The best potential configuration found is listed in Tab. 5.1.

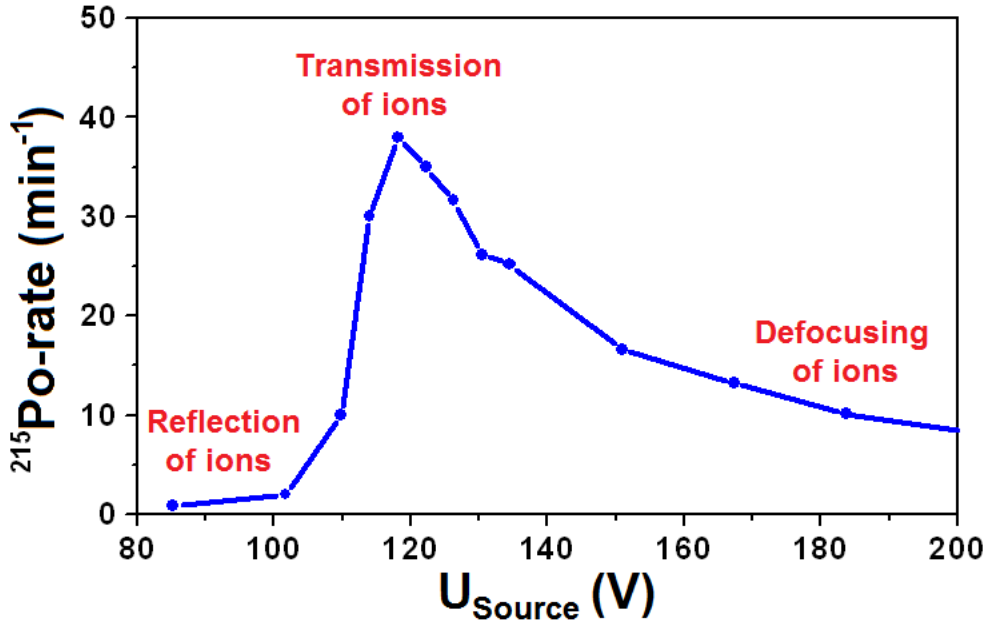


Figure 5.3: Registered ^{215}Po rate as function of the Ra-source potential. Measurements are performed at a source-nozzle distance of 29 mm and an argon pressure of 40 mbar. See Tab. 5.1 for the corresponding electrode potentials.

5.1.3 Determination of the extraction time

The steep onset of the registered ^{215}Po rate in Fig. 5.3 allows for a pulsed extraction of polonium ions. Potential differences of $\approx 20\text{ V}$ to the optimum U_{Source} are sufficient to switch between “reflection” and “transmission” of the ions. The potential of the recoil source is switched using two high voltage modules coupled to a fast high voltage transistor switch, which is triggered by the FPGA module (see Sect. 4.3 and Appendix B.2). At the beginning of each 40 ms cycle, a reset of the FPGA time counter is enforced. Pulse structure and registered ^{215}Po decay events are shown in Fig. 5.4. In this triggering mode, extraction time and α energy can be assigned to each registered event. The extraction time t_{ex} of the Po ions from the drift cell has been deduced by fitting the exponential decay $f_{\text{Po}}^d(t) = a_1 + a_2 \cdot \exp\left[-(\ln 2/t_{1/2}^{\text{Po}})(t - t_{ex})\right]$ and the exponential growth $f_{\text{Po}}^g(t) = a_1 + a_2 \cdot \left\{1 - \exp\left[-(\ln 2/t_{1/2}^{\text{Po}})(t - t_1 - t_{ex})\right]\right\}$ to the first and second half-cycle of the spectrum shown in Fig. 5.4, respectively. Identical fit parameters for offset a_1 , amplitude a_2 and $t_{1/2}^{\text{Po}}$ are used in both fits. The onset of the “transmission” period amounts to $t_1 = 20\text{ ms}$. Increasing the source-nozzle distance from $d_{SN} = 14\text{ mm}$ to $d_{SN} = 79\text{ mm}$ results in an increase of the extraction time from $t_{ex} = 0.5\text{ ms}$ to $t_{ex} = 4.3\text{ ms}$.

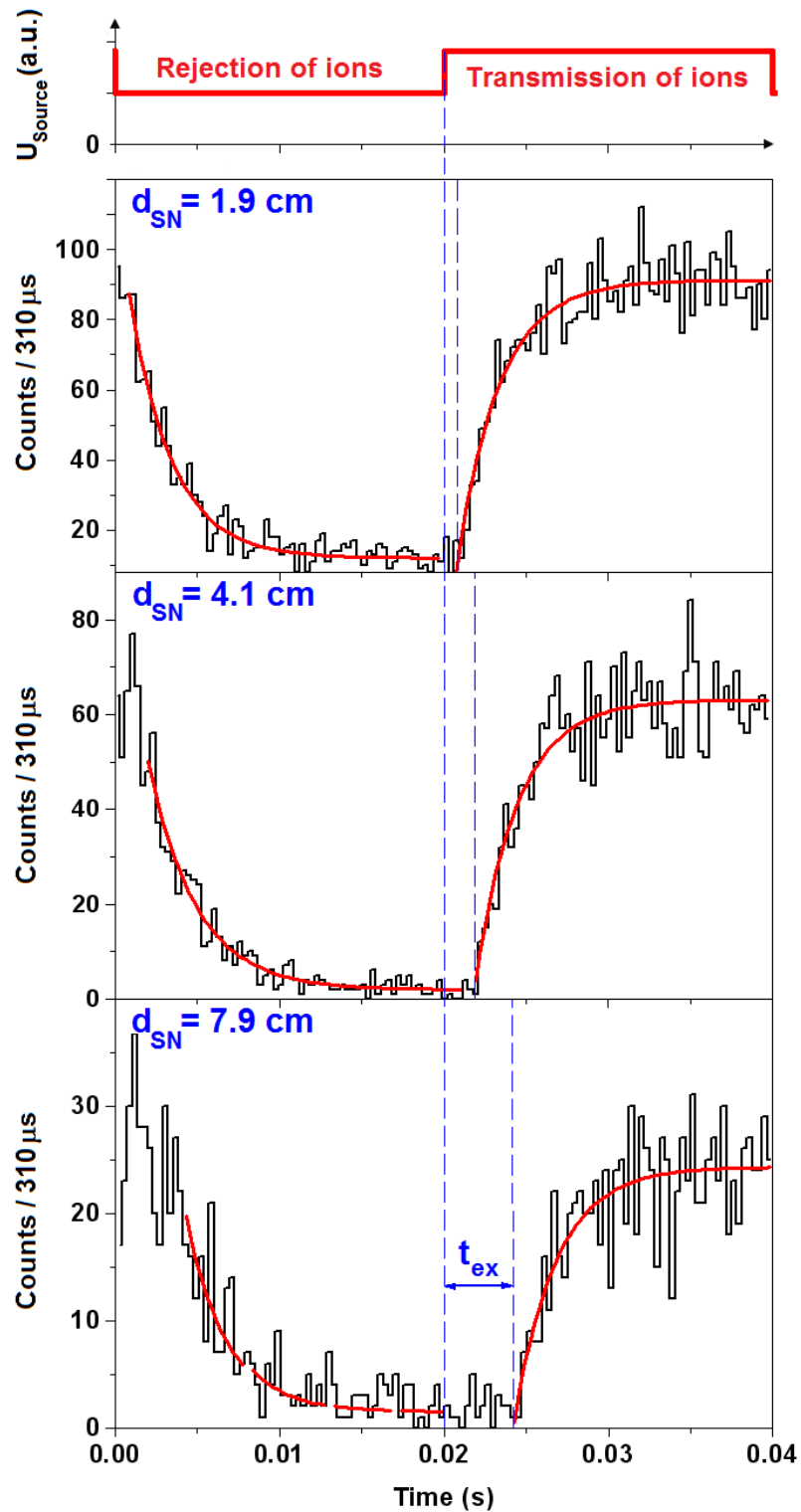


Figure 5.4: Determination of the extraction time of $^{215}\text{Po}^+$ ions at different source-nozzle distances d_{SN} . Measurements are carried out at 40 mbar argon using an electric field configuration corresponding to Tab. 5.1.

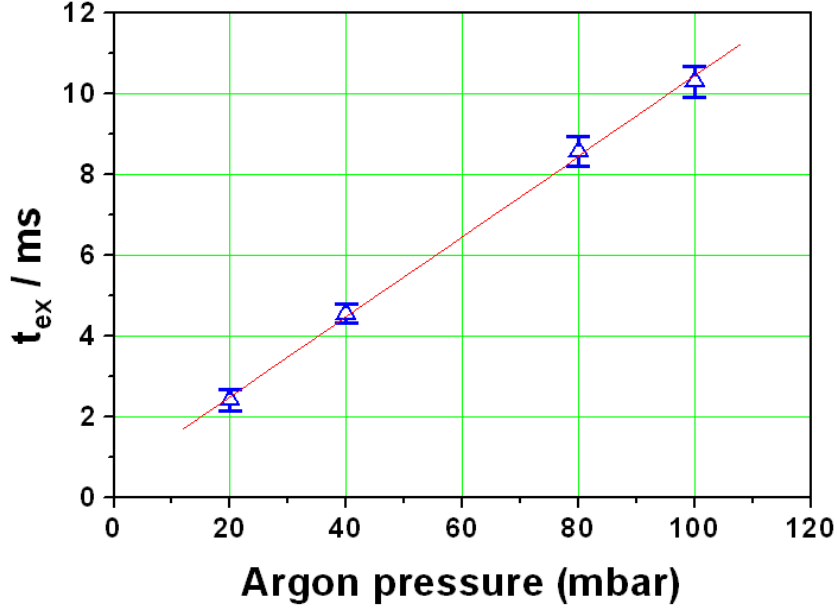


Figure 5.5: Extraction time t_{ex} of $^{215}\text{Po}^+$ ions at different buffer gas pressures. The source-nozzle distance is fixed at 79 mm. The applied electrode potentials are shown in Tab. 5.1. The solid line is a linear fit to the experimental data.

A linear dependence of the extraction time on the buffer gas pressure is observed in a range from 20 mbar to 100 mbar at a fixed source-nozzle distance, see Fig. 5.5. The error bars are dominated by statistical fluctuations of the α decays due to a low count rate after nearly 6 half-lives of ^{215}Po .

5.1.4 Determination of the extraction efficiency

The extraction efficiency ε_{ex} is given by the ratio of the number N_{Po}^{ex} of extracted to stopped (N_{Po}^{stop}) ^{215}Po ions. The latter can be determined if the source activity A_{Ra} is known according to

$$N_{Po}^{stop} = \int_{\Delta t_m} dt (A_{Ra} \cdot \varepsilon_{Po}^{esc}) \quad (5.1)$$

with the measurement time Δt_m (few minutes) and the escape efficiency $\varepsilon_{Po}^{esc} = 14.5\%$ [50] of polonium ions recoiling out of the ^{223}Ra ($t_{1/2}^{Ra} = 11.44$ d) source. The efficiency ε_{det} for the detection of α particles emitted by Po ions on the detector surface is assumed to be about 50 %, hence:

$$N_{Po}^{ex} = \frac{N_{Po}^{det}}{\varepsilon_{det}} \quad (5.2)$$

with N_{Po}^{det} denoting the number of detected Po ions after extraction during a measurement time equal to Δt_m . Corrections have to be applied for the decay of the Ra source

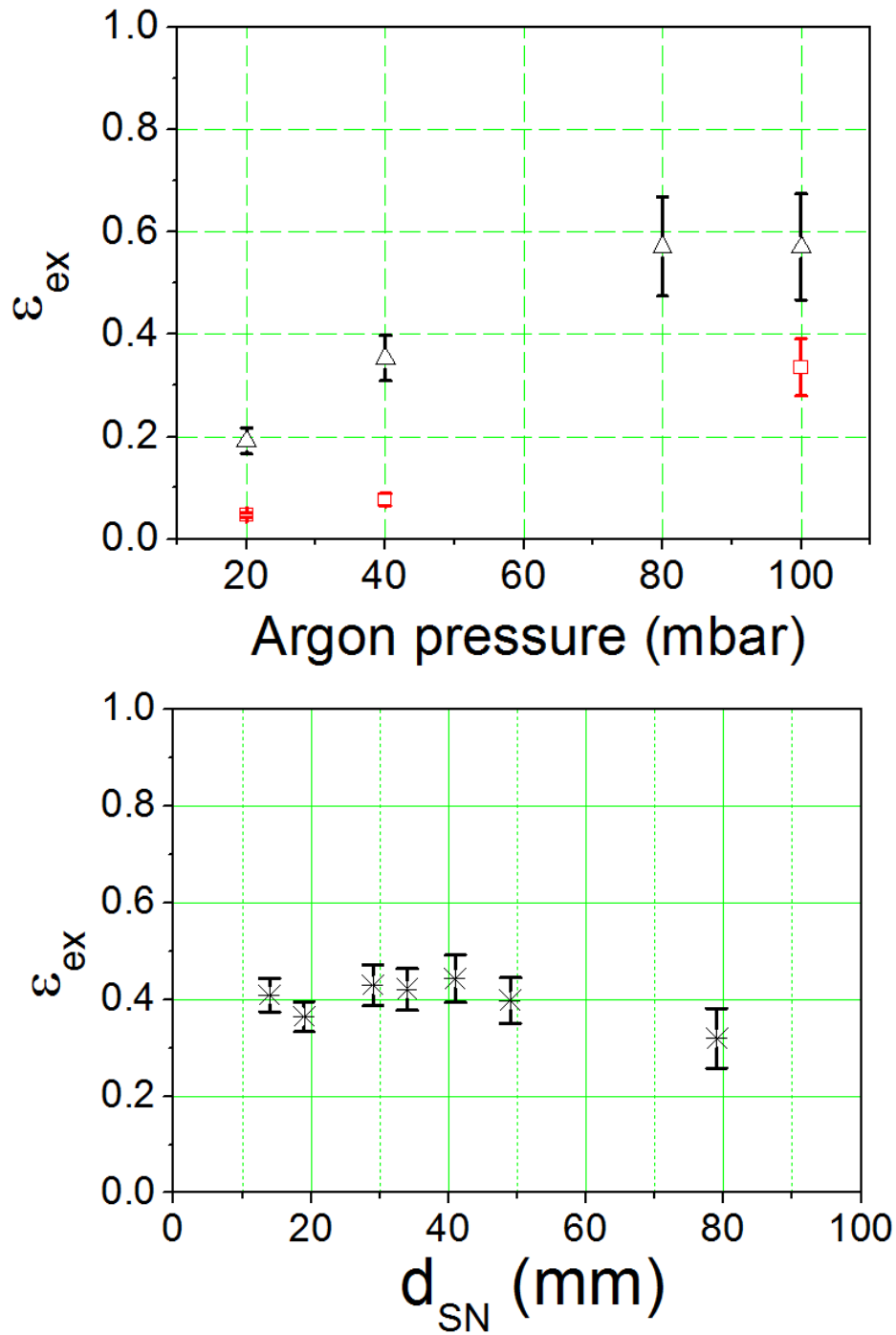


Figure 5.6: Upper plot: Extraction efficiency of $^{215}\text{Po}^+$ ions at different buffer gas pressures for two different nozzle throat diameters of 1 mm (Δ) and 0.5 mm (\square). The source-nozzle distance is fixed at 79 mm. HV settings as shown in Tab. 5.1 are used. Lower plot: Extraction efficiency (1 mm nozzle) vs. different source-nozzle distances d_{SN} at 40 mbar argon. The potentials listed in Tab. 5.1 are used during the measurements, whereas the source potential is optimized to give highest count rates at each adjusted d_{SN} .

during the period t between the determination of A_{Ra} and the extraction efficiency measurement and for the decay of ^{215}Po during the extraction time t_{ex} :

$$\varepsilon_{ex} = \frac{N_{Po}^{ex} \cdot e^{\lambda_{Po} \cdot t_{ex}}}{N_{Po}^{stop} \cdot e^{-\lambda_{Ra} \cdot t}} \quad (5.3)$$

The decay constants of ^{223}Ra and ^{215}Po are denoted by λ_{Ra} and λ_{Po} , respectively.

The extraction efficiency ε_{ex} for ^{215}Po ions is determined as a function of the buffer gas pressure for nozzles of 1 mm and 0.5 mm diameter and is shown in Fig. 5.6. It increases with the buffer gas pressure up to $(57 \pm 10)\%$ at 80 mbar for the larger nozzle, which reflects the strong influence of the friction force acting on the ions at the nozzle cone on the extraction efficiency. The uncertainty in the determination of the extraction time t_{ex} dominates the error bars in this plot. In contrast to the model used in Ref. [50], no neutralization of polonium is assumed in this work. Neutralization depends strongly on the buffer gas purity, which has not been measured for the used setup so far. The extraction efficiency of the cell at 40 mbar argon is about 10% less than the one claimed in Ref. [51] for a similar but smaller drift cell [50] if the same gas purity and a neutralization efficiency of polonium of $0.5_{-0.35}^{+0.15}$ [50] is assumed.

At low pressures the extraction efficiency using the 0.5 mm nozzle is almost 4 times less than in case of a 1 mm nozzle throat (see Fig. 5.6, upper plot). This may be explained by the lower gas flow achievable with the smaller orifice, which in turn cannot create enough gas friction that could counteract the defocusing electrostatic forces on the ions inside the nozzle cone. According to measurements, however, this factor decreases to 1.7 at 100 mbar argon and thus promises further efficiency increase without the need for high-performance turbomolecular pumps in the extraction chamber if working at higher pressures. This again indicates that both the electric field and the gas flow at the nozzle cone strongly influence the extraction efficiency.

In addition, increasing the source-nozzle distance at stationary E/n conditions causes an increment in the ion drift time t_d . In Ref. [50] it is stated that each elapsed 40 ms correspond to a mean ion displacement of 4 mm from the axis of the drift cell due to diffusion phenomena. Since only ions arriving at the nozzle throat within a distance $\leq d_{Noz}/2$ from the symmetry axis are efficiently extracted, ion diffusion results in smaller extraction efficiencies, as is generally known [1]. The diffusion losses for the envisaged mobility measurements could not yet be measured with the ^{223}Ra recoil source, since then t_d has to be increased to about 20 half-lives of ^{215}Po , which implies negligible count rates when working with source activities of usually 4 – 10 kBq.

Figure 5.6 (lower plot) shows the extraction efficiency (1 mm nozzle) of Po ions at 40 mbar argon as a function of different values for d_{SN} . During the measurements, the potentials listed in Tab. 5.1 are used, whereas the source potential is optimized to give highest count rates at each adjusted source nozzle-distance. Inside the focusing electrodes the efficiency stagnates at about 40% and decreases due to diffusion losses to $(32 \pm 6)\%$ at $d_{SN} = 79$ mm.

5.2 Commissioning and optimizing the detection part of the spectrometer

In the following, the optimization procedures of the detection part of the spectrometer will be explained. The main goal of such test experiments is to achieve lowest background pressures inside the differential pumping section and to allow for an efficient detection of the sample ions using the channeltron detector installed inside the detection chamber.

5.2.1 The background pressures inside the differential pumping section

It becomes clear from the considerations presented in Sect. 3.3.3 that the background pressure inside the differential pumping section has to be as small as possible in order to guarantee a negligibly small transit time of the ions from the nozzle to the detector compared with their drift time inside the gas cell. For controlling the buffer gas flow through the nozzle at a constant cell pressure, two nozzles of 0.5 mm and 1 mm throat diameter have been tested. It has been found that the nozzle with an orifice of 0.5 mm diameter is best suited for the envisaged mobility measurements when using the setup arrangement described in Sect. 4.1, because it delivers lowest possible background pressures inside the different vacuum chambers of the spectrometer. The latter pressures vs. the cell pressure when using the nozzle of 0.5 mm throat diameter are shown in Fig. 5.7. The extraction chamber has a background pressure of $P_{1section} < 0.06$ mbar for cell pressures below 60 mbar. The pressure in the detection chamber $P_{5section}$ remains essentially uninfluenced by pressure variations in the cell and stagnates at the 10^{-6} mbar level. The latter is well below the critical pressure, at which the QMS can still be operated [89]. The most important background pressure, however, is the one prevailing in the extraction chamber $P_{1section}$. Most of the IMS measurements presented in this work are carried out at 40 mbar Ar, resulting in a background pressure of 0.045 mbar in the extraction chamber. Since the ion path in this chamber is about 10 cm, only a limited number of ion-atom collisions may be expected to take place in that pumping section and remains uncritical for drift time measurements, see also Sect. 3.3.3. The background pressures in the other vacuum chambers are much less than $P_{1section}$, such that further ion-atom collisions in these chambers may not have any significant effect on the ion transit time.

5.2.2 The potential configuration inside the detection part

Gas discharges between two electrodes of the drift cell are exploited to produce enough argon ions, which could be taken for optimizing the guiding potentials inside the detection part of the spectrometer. A rough potential configuration for the ion guide segments, the QMS rods, the 90° deflector, the electrostatic lenses and the channeltron

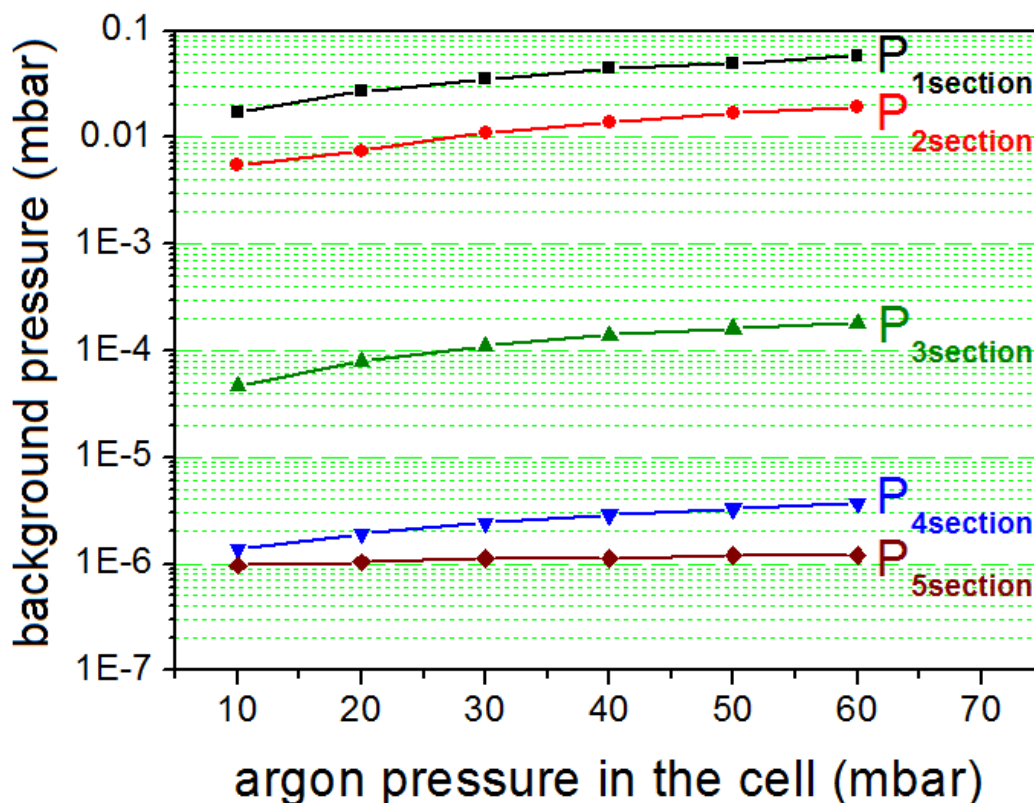


Figure 5.7: Background pressure in the different pumping sections of the apparatus as shown in Fig. 4.1 vs. the buffer gas pressure in the cell. Only the nozzle of 0.5 mm throat diameter is used.

detector (see Fig. 4.1) could be extracted from earlier experimental setups using similar detection chambers [50, 51]. After tuning the potentials to give highest count rates in the detector, a subsequent fine tuning could be performed using the heavier erbium ions created inside the cell via laser resonance ionization techniques, see Sect. 6.1. The potential configuration used in the detection part of the apparatus is schematically shown in Fig. 5.8 and the corresponding best suited potentials resulting in highest ion count rates are listed in Tab. 5.2. The potential gradient between the nozzle and the first QPIG segment is 180 V/cm. The offset potentials for the first six segments inside the extraction chamber decrease in 10 V steps, since a relatively small mean free path of the ions is expected there when compared with the other vacuum chambers of the detection part (see Fig. 5.7). One may further increase the potential gradients inside the extraction chamber, which definitely result in a faster ion transfer, but such an increment bears the risk of gas discharges between the corresponding QPIG segments. In the subsequent pumping sections, the offset potentials for the remaining 22 QPIG segments are decreased in ca. 2.1 V steps until arriving at a grounded diaphragm, which belongs to the mass filter housing. The potential gradient for these QPIG segments is

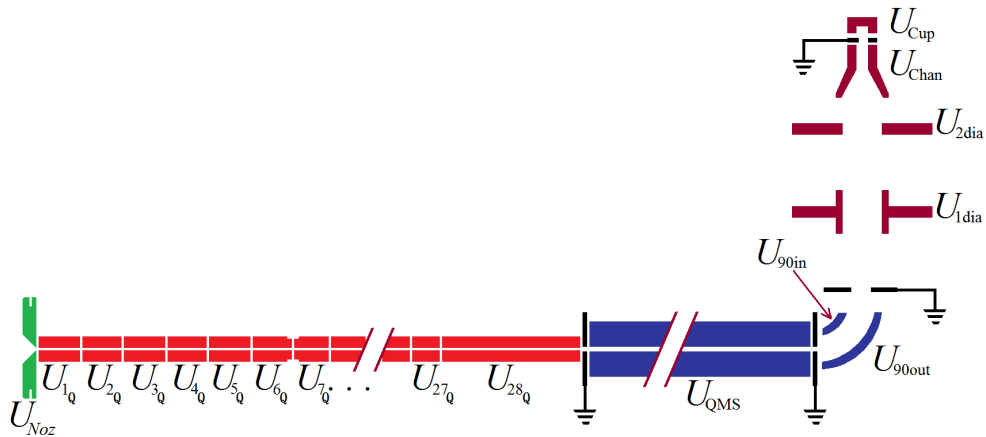


Figure 5.8: The different static potentials used in the detection part of the IMS. In case of the QPIG and QMS, these potentials are additionally applied as offsets to the quadrupolar potentials in order to push the trapped ions through the differential pumping section.

sufficient for a fast ion transfer due the vacuum of $\leq 10^{-2}$ mbar prevailing in the corresponding pumping sections. The QMS itself has an offset potential of $U_{QMS} = -26.2\text{V}$. All transmitted and filtered ions are deflected by 90 degrees and then focused by an electrostatic lens system onto the channeltron detector inside the detection chamber, see Fig. 4.1 and Fig. 5.8. The channeltron detector operates at -2.62kV bias voltage, resulting in a gain of $> 2 \cdot 10^8$ [99], which makes further pulse preamplification dispensable. For more detailed information about such single ion detectors based on electron multiplication by secondary emission, the reader is referred to [100, 111, 112] and the references therein. The detector end cap is operated at a bias voltage of $+180\text{V}$ in order to better collimate and attract the produced secondary electrons by each ion event. The most critical value in the potential configuration shown in Fig. 5.8 is that of the deflector. It is essential to optimize the corresponding potentials U_{90in} and U_{90out} , such that highest count rates of the heavy ions of interest are registered. Such an optimization procedure is shown in Fig. 5.9 (left plot) for erbium ions created via RIS methods presented in Sect. 6.1. The deflector potential U_{90out} is fixed at a constant value of -30.8V , whereas U_{90in} is decreased from -50V down to -180V . The best suited value for the latter potential is about -116V . The optimal and efficient RF amplitude for trapping and guiding heavy ions through the pumping sections is found to be 100V_{pp} , see Fig. 5.9 (right plot). Unlike heavy ions, all singly charged ions with masses less than $m_{min} \approx 46\text{u}$ have unstable trajectories inside the QPIG and cannot be transmitted to the QMS at this RF amplitude according to Eq. (3.10). Increasing the RF voltage amplitudes beyond this optimum does not only increase the risk of gas discharges in the first pumping section, but also decreases the transmission efficiency of the ion guide, due to the retarding effects such potentials create between the nozzle and the first QPIG segment.

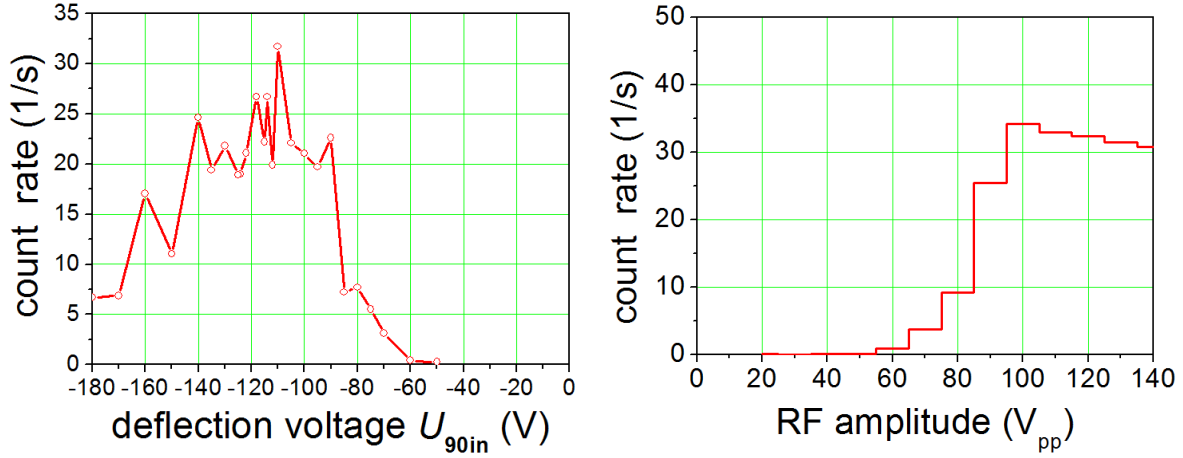


Figure 5.9: Optimization of the potential configuration inside the detection part using resonantly ionized ^{174}Er . Left: Determination of the optimal deflection voltage U_{90in} . Right: Determination of the optimum RF voltage of the ion guide.

Table 5.2: Static potentials used in the detection part of the apparatus, see Fig. 5.8.

U_{Noz}	U_{Q1}	U_{Q2}	U_{Q3}	U_{Q4}	U_{Q5}	U_{Q6}	U_{Q7}	U_{Q8}
126V	108V	98V	88V	78V	68V	58V	47.6V	45.5V
U_{Q9}	U_{Q10}	U_{Q11}	U_{Q12}	U_{Q13}	U_{Q14}	U_{Q15}	U_{Q16}	U_{Q17}
43.3V	41.1V	39.0V	36.8V	34.6V	32.5V	30.3V	28.2V	26.0V
U_{Q18}	U_{Q19}	U_{Q20}	U_{Q21}	U_{Q22}	U_{Q23}	U_{Q24}	U_{Q25}	U_{Q26}
23.8V	21.7V	19.5V	17.4V	15.2V	13.0V	10.9V	8.7V	6.6V
U_{Q27}	U_{Q28}	U_{QMS}	U_{90in}	U_{90out}	U_{1dia}	U_{2dia}	U_{Chan}	U_{Cup}
4.4V	2.2V	-26.2V	-116.2V	-30.8V	-70.5V	-204.5V	-2620V	180.0V

5.3 Determination of highest possible E/n parameters

The E/n parameter is basically determined by the working pressure, at which the mobility measurements will take place, and by the geometrical constraints of the drift cell, which predefines the upper limit of applicable electric fields at that pressure. It may become quite difficult to predict the critical voltage for gas discharges for a complex electrode system like the one used in the drift cell. The investigation of gas discharges using parallel electrode plates as shown in Appendix C provides too optimistic reference values of breakdown voltages, because the potential gradients between the neighboring

electrodes are less critical to gas discharges than those between the electrodes and the walls of the drift cell. This holds especially for electrodes near the entrance window with highest potentials. The highest risk for discharges, however, exists at the pins of the electrical feedthroughs described in Sect. 4.1.1 and at the filament mountings shown in Fig. 4.3.

Test experiments have shown the potential configuration listed in Tab. 3.2 to be applicable only at cell pressures ≥ 40 mbar Ar. In fact, working at elevated cell pressures relieves the situation for gas discharges according to Eq. (3.3) and allows for an efficient ion extraction as demonstrated in Sect. 5.1.4. In this work, however, cell pressures up to 40 mbar are envisaged in order to avoid higher background pressures inside the differential pumping section, see Sect. 5.2. For measurements at pressures below 40 mbar or when testing different E/n parameters, all electrode potentials listed in Tab. 3.2 have to be scaled by a factor F (often $1/3$ or $2/3$) according to

$$U^* = [(U - U_{Noz}) \cdot F] + U_{Noz}, \quad (5.4)$$

with the nozzle potential $U_{Noz} = 126$ V. In this equation, U denotes the potential of a certain drift electrode and U^* its corresponding scaled potential. Such a scaling of the potentials allows for producing ion trajectories similar to those shown in Fig. 3.3 (a) and simultaneously for adjusting the drift time of the ions in a range between 10 ms and 100 ms, see Sect. 6.3. Most mobility measurements are carried out at 40 mbar, at which the potential configuration listed in Tab. 3.2 could be realized. This configuration results in an E/n ratio of 1.8 Td. Highest values for E/n are obtained at 20 mbar and 10 mbar with a mean value of 2.4 Td and 4.8 Td, respectively.

5.4 Estimation of the overall detection efficiency of the IMS apparatus

For simplicity reasons, the ion production process is disregarded and the detection efficiency ε_{tot} of the apparatus is defined as the ratio of detected ions N_{det} vs. the number of ions N_{ion} existing inside the cell at the beginning of each measurement cycle

$$\varepsilon_{tot} = \frac{N_{det}}{N_{ion}}. \quad (5.5)$$

Assuming no chemical or charge exchange reactions occur during the ion drift, this efficiency can be factorized into 4 contributions according to

$$\varepsilon_{tot} = \varepsilon_{ex} \cdot \varepsilon_{QPIG} \cdot \varepsilon_{QMS} \cdot \varepsilon_{det}. \quad (5.6)$$

ε_{ex} is the extraction efficiency discussed before. For the electrode potentials listed in Tab. 5.1, this amounts to $(8 \pm 1)\%$ for the 0.5 mm nozzle at 40 mbar argon. As mentioned in Sect. 5.1.4, the interplay between the gas flow and the electrostatic field inside the nozzle cone seems to have a big impact on the extraction efficiency. From this point of view, ε_{ex} is expected to decrease when working at relatively higher electric fields than those resulting from Tab. 5.1.

ε_{QPIG} stands for the ion guiding efficiency. Ions trapped inside the QPIG are efficiently guided through the different pumping sections due to the gas cooling mechanism, which forces the ions to stay at the minimum of the quadrupolar potential. However, ions may hit the first QPIG segments while they get extracted in the supersonic gas stream inside the extraction chamber. Therefore, ε_{QPIG} is expected to be in the range between 40 % and 100 % similarly to the guiding efficiency claimed in Ref. [51].

ε_{QMS} is the QMS transmission efficiency. It decreases with increasing mass resolution, due to the fluctuations in the ion oscillations inside the quadrupole potential of the QMS. This efficiency depends also on the ion mass [89] such that it should be determined for each measurement series. At a moderate QMS resolution, ε_{QMS} is estimated to be $(30 \pm 10)\%$ as has been obtained in Ref. [50].

ε_{det} denotes the detection efficiency of the channeltron detector in conjunction with the deflection electrodes and the lens system shown in Fig. 5.8. In former investigations [50], this efficiency was found to have a best value of $(56 \pm 5)\%$, which is assumed to hold also for the described apparatus with the optimized potentials listed in Tab. 5.2.

Hence, the overall efficiency is expected to be in the range between $(0.5 \pm 0.2)\%$ and $(1.3 \pm 0.5)\%$ at a cell pressure of 40 mbar argon when using the 0.5 mm nozzle, which still allows for mobility measurements using primed filaments in off-line experiments [51, 113]. However, further improvements and tests have to be performed in order to be efficient enough for mobility investigations in the region of actinides and transactinides in online experiments. The ion extraction and detection efficiency achievable can be increased by about a factor of 10 if working at higher cell pressures and using larger extraction nozzles. To achieve this goal, an efficient pumping of the detection part of the apparatus is mandatory.

6 Investigation of the time resolution by RIS methods

Extensive test experiments using laser resonance ionization techniques at certain lanthanide elements are carried out to determine the time resolution of the spectrometer in advance of systematic mobility studies. Special emphasis is put on the influence of the cell pressure and of the laser beams on the time resolution as well as on the arrival time distributions. A sizable part of this chapter is dedicated to discuss the consequences of such an influence and to present the strategy followed in this work to guarantee mobility measurements of high precision.

6.1 Creation of sample ions by RIS methods

In order to obtain sample ions in off-line experiments, the elements of interest should be available in a pure form of macroscopic quantities. Using electrochemical deposition techniques [114], lanthanide as well as actinide (up to fermium) filaments can be produced. The elements, usually in the form of hydroxides in solutions, are deposited on a tantalum carrier foil of 25 – 50 μm thickness and subsequently covered by a 1 – 2 μm titanium layer. More details on this method and its benefits for laser spectroscopic investigations at heavy elements can be found in Ref. [114] and [115]. Another alternative may be the vacuum evaporation-condensation techniques described in Ref. [116], which actually allow for the production of radioactive targets for nuclear accelerator experiments. The evaporant is heated in the evaporation source up to a temperature which causes the generation of a vapor cloud. This cloud propagates in vacuum towards the carrier foil, where it is condensed in form of a thin film of desired area densities. More details on this topic can be found in Ref. [117, 118].

Since this work focuses on the mobility of lanthanide elements, neither of both techniques has been extensively tested with the developed spectrometer. Instead commercially available lanthanide foils of 99.9% purity [71] are used. In the mobility measurements carried out, the sample foil is fixed between two clamps of the filament mounting through which a current of $< 5\text{ A}$ can flow (see Fig. 6.14). The power supply (DELTA Elektronika, ES030-5) used for filament heating is galvanically isolated from the network such that a filament potential can be applied according to Fig. 3.3 (c). Usually 25 μm thin foils (25 mm x 1 mm) are used in order to minimize the heat output inside the drift cell. During mobility experiments, the filament temperatures are determined with an uncertainty of $\leq 50\text{ K}$ using a pyrometer (Keller Pyro, type: PB06 AF3).

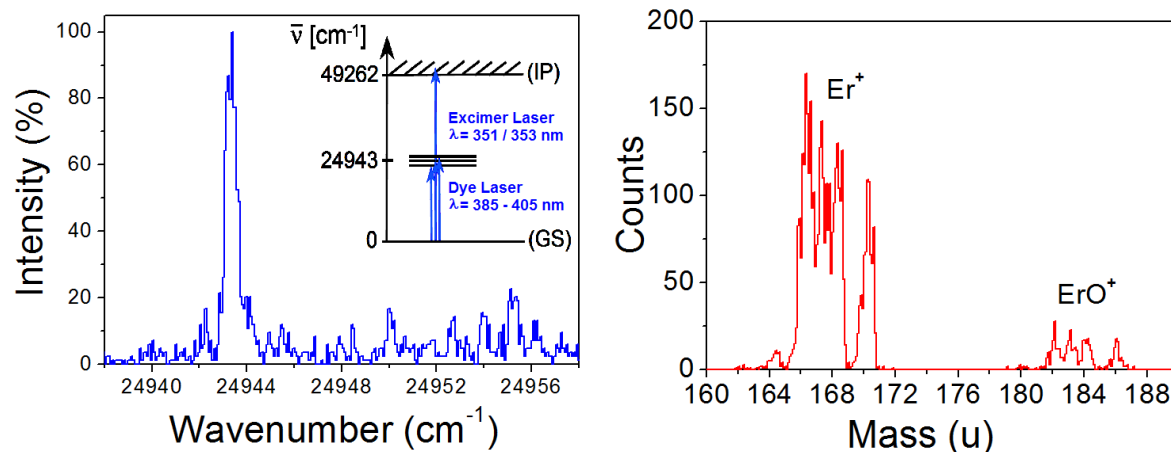


Figure 6.1: Left: Laser resonance ionization spectrum for ^{168}Er at 19 mbar buffer gas pressure ($E/n = 1.2 \text{ Td}$). Right: Mass spectrum when ionizing erbium ($E/n = 2.4 \text{ Td}$, 20 mbar Ar).

Exploiting the Resonance Ionization Spectroscopy method described in Ref. [30, 53], an almost background-free ionization can be easily achieved, see also Sect. 3.2. With this method, the evaporated atoms of interest are resonantly ionized using laser beams of suitable wavelengths provided by the excimer-pumped dye laser system described in Sect. 4.2. The ionization process takes place only once per single laser shot of $\Delta t \approx 15 \text{ ns}$ duration, which allows for a precise determination of the starting time t_0 . The such created ions drift in a homogeneous electric field inside the cell, get extracted, mass selected by the QMS and subsequently detected by the channeltron detector (see Sect. 4.1 and Sect. 5.2).

6.2 Identifying the signals of sample ions

After admitting argon gas into the drift cell, heating up the sample filament up to $T_{Fil} = 1250 \text{ K}$ and applying appropriate potentials to the different spectrometer electrodes, one may try to determine the excitation wavenumber $\bar{\nu}_{12}$ of the element of interest based on the literature values given in Tab. 3.1.

The vapor above the filament is exposed to the laser beams described before, whereas the first excitation energy corresponding to $\bar{\nu}_{12}$ is varied such that a resonance spectrum like the one shown in the left plot of Fig. 6.1 is obtained. By studying such spectra, it has been found that the used wavemeter is out of tune and needs to be re-calibrated, since all measured resonances of different lanthanide elements are about 2.6 cm^{-1} shifted to higher energies compared to the literature values.

Figure 6.1 (left plot) shows the corrected resonance spectrum of ^{168}Er measured at an E/n ratio of 1.2 Td . The resonance peak of 0.6 cm^{-1} width is found at

$\bar{\nu}_{12} = 24943 \text{ cm}^{-1}$. Lasing energies of only $6 \mu\text{J}$ per pulse are sufficient to saturate the selected excitation state of Er. The non-resonant second step is provided by the excimer laser beam ($102 \mu\text{J}$ per pulse). Increasing the dye laser intensity more than necessary enhances the multiphoton ionization probability [59] and may indirectly result in broadened arrival time distributions of the investigated ions.

The right plot of the same figure shows a mass spectrum of singly charged erbium. In this case $\bar{\nu}_{12}$ is fixed at the Er resonance obtained before and the mass resolution is adjusted such that neighboring isotopes are efficiently suppressed. The stable erbium isotopes $^{162,164,166,167,168,170}\text{Er}$ as well as their oxides can be clearly identified in this spectrum. During their drift inside the cell, Er^+ may react with residual impurities and thereby create erbium oxides according to Eq. (7.4).

Further resonance and mass spectra of the investigated elements are shown in Fig. 6.2 and Fig. 6.3. Most of the spectra have been measured using ($25 \mu\text{m} \times 1 \text{ mm} \times 25 \text{ mm}$) lanthanide strips. The only exception is europium, which could be provided only as $100 \mu\text{m}$ thick foils. The obtained first step resonances of the different elements are $\bar{\nu}_{12}(^{174}\text{Yb}) = 25068.2 \text{ cm}^{-1}$, $\bar{\nu}_{12}(^{165}\text{Ho}) = 24660.8 \text{ cm}^{-1}$, $\bar{\nu}_{12}(^{156}\text{Dy}) = 21838.6 \text{ cm}^{-1}$, $\bar{\nu}_{12}(^{159}\text{Tb}) = 23107.3 \text{ cm}^{-1}$, $\bar{\nu}_{12}(^{156}\text{Gd}) = 21857.5 \text{ cm}^{-1}$ and $\bar{\nu}_{12}(^{151}\text{Eu}) = 21761.3 \text{ cm}^{-1}$. The non-resonant second step is provided by the UV light of the excimer laser.

The corresponding mass spectra (right plots in the same figures) are measured with a moderate QMS resolution such that enough events are registered but neighboring isotopes are efficiently suppressed. Depending on the residual impurities inside the cell, molecules of the different isotopes [119] are formed. Besides terbium, the elements have been consecutively tested such that clear mass spectra are obtained. Otherwise, if more than one sample element is evaporated, difficulties may arise while identifying the registered peaks, especially in the presence of residual gas impurities, see chapter 7.

6.3 The arrival time distribution

Figure 6.4 shows the arrival time distribution (ATD) of Er^+ at an E/n ratio of 2.4 Td and an argon pressure of 20 mbar . The erbium ions are created by the two-step photoionization process described before. Most ATD peaks of the monoatomic ions under investigation have a Gaussian-like shape, see Fig. 6.4. However, solving the differential equation governing the drift and diffusion of the ions in drift tubes provides satisfying predictions of the ATD profiles. A commonly used formula in the ATD analysis is given by ([2], p. 90)

$$\Phi(0, z, t) = \frac{\hat{s} \cdot A_0 \cdot \exp(-\alpha_c t)}{4\sqrt{\pi D_L t}} \left(v_d + \frac{z}{t} \right) \cdot \left[1 - \exp\left(-\frac{\rho^2}{4D_T t}\right) \right] \exp\left(-\frac{(z - v_d t)^2}{4D_L t}\right) \quad (6.1)$$

with the following parameters:

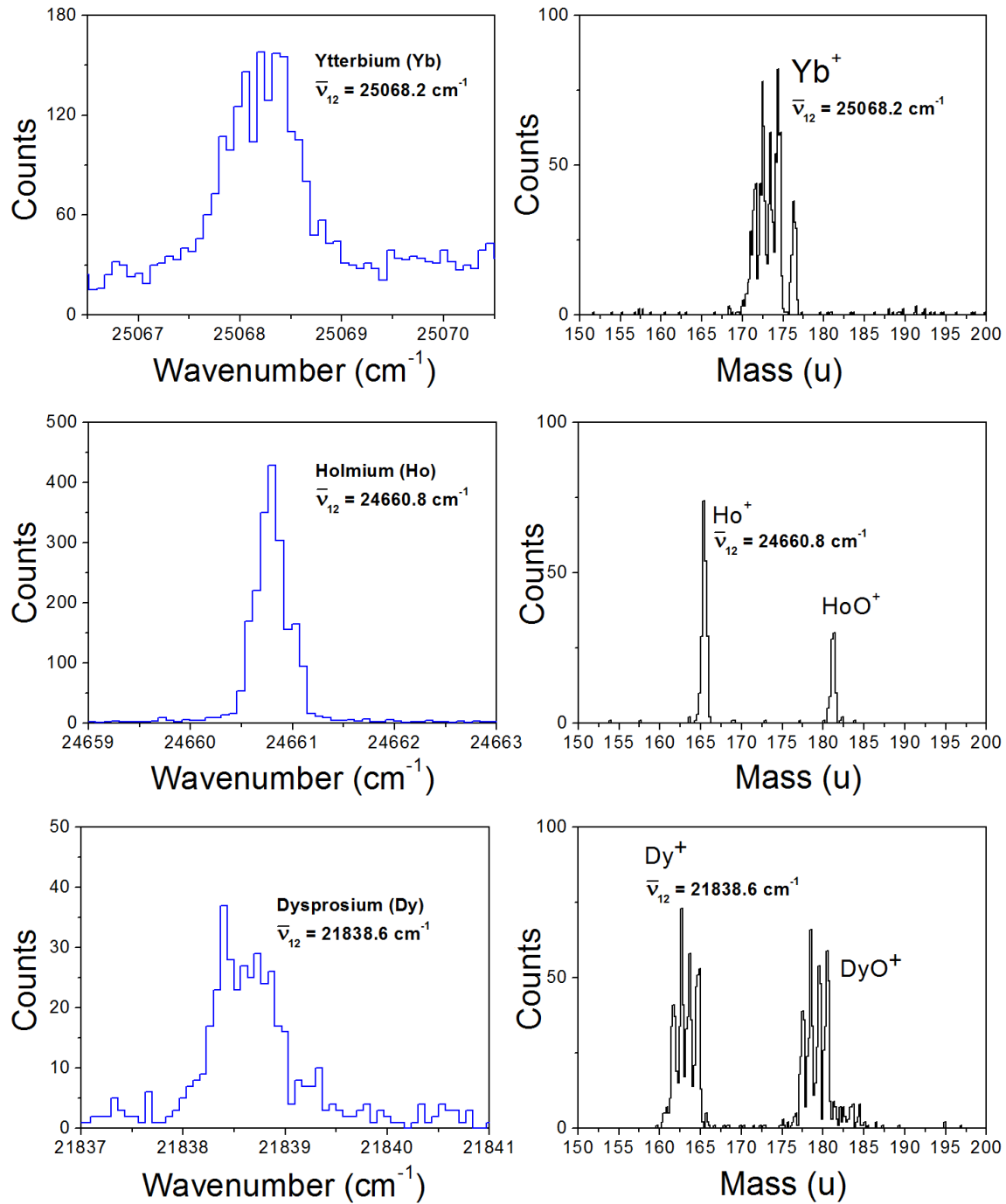


Figure 6.2: Left column: Laser resonance ionization spectra for ^{174}Yb , ^{165}Ho and ^{156}Dy at 40 mbar buffer gas pressure ($E/n = 1.8 \text{ Td}$). The resonance peaks correspond to the wavenumber $\bar{\nu}_{12}$. Right column: The corresponding mass spectra measured at the same pressure and E/n ratio.

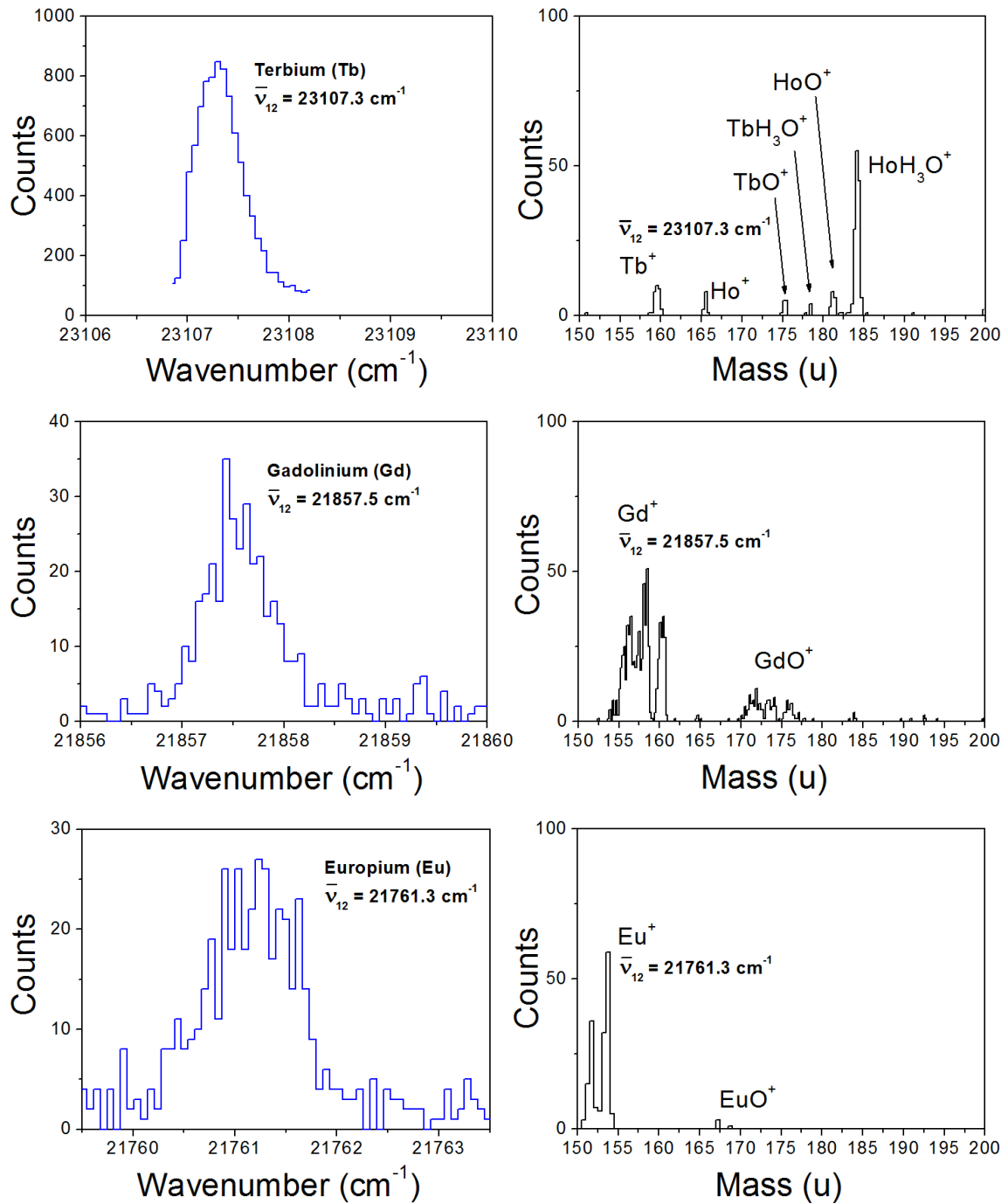


Figure 6.3: Left column: Laser resonance ionization spectra for ^{159}Tb , ^{156}Gd and ^{151}Eu at about 40 mbar buffer gas pressure ($E/n = 1.8 \text{ Td}$). The resonance peaks correspond to the wavenumber $\bar{\nu}_{12}$. Right column: The corresponding mass spectra measured at the same pressure and E/n ratio.

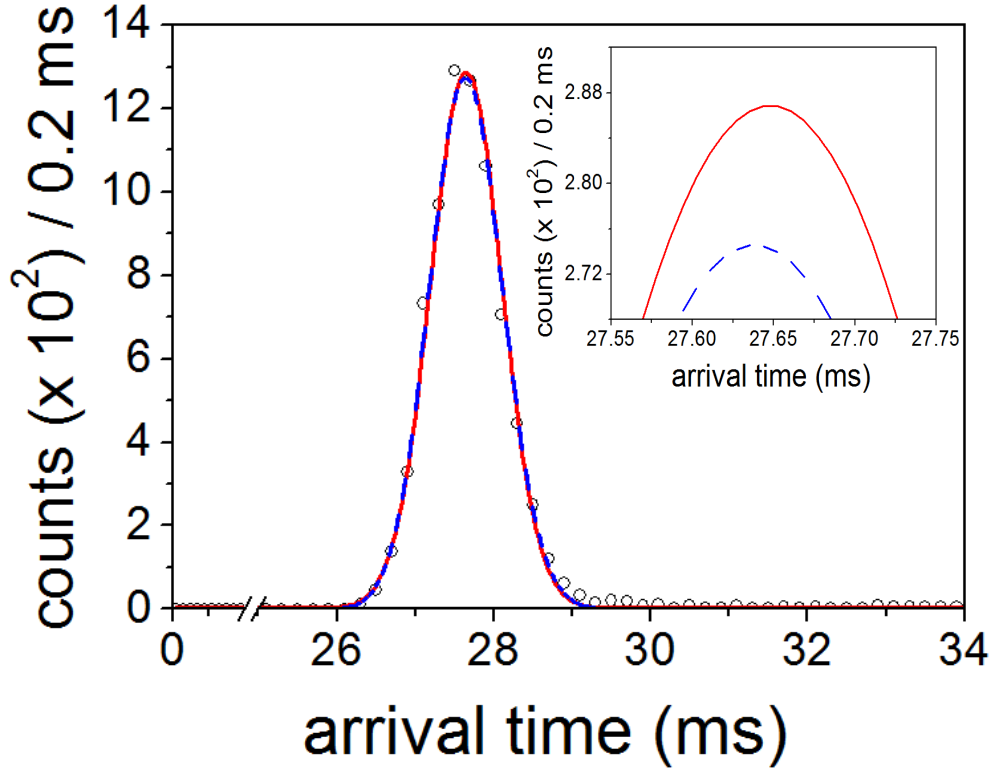


Figure 6.4: The arrival time distribution of Er^+ at an E/n ratio of 2.4 Td and an argon pressure of 20 mbar. The solid line is a Gaussian fit of the Er^+ data, whereas the dashed line represents a fit according to Eq. (6.2). In the upper corner the same plot is magnified around the peak maximum for distinguishing both fits.

$\Phi(0, z, t)$ is the experimentally measured flux of ions as a function of the time t and drift distance z .

\hat{s} denotes the initial ion surface density of the delta-function input of ions. This planar source density is given by the number of ions N_{ion} created instantaneously at $t' = 0$ and $z' = 0$ in a thin disk of radius ρ according to $\hat{s} = N_{ion}/\pi\rho^2$.

A_0 is the area of the nozzle throat given by $A_0 = \pi d_{Noz}^2/4$.

α_c describes the frequency of chemical reactions that lead to ion losses inside the drift cell.

D_L and D_T are the longitudinal and transversal diffusion coefficients of the ions.

v_d is the drift velocity of the ions.

This equation considers only ions of the single species introduced from an ion source in periodic delta functions, whereas none is produced by reactions in the drift space. Allowed, however, is the loss of ions in chemical reactions producing other species,

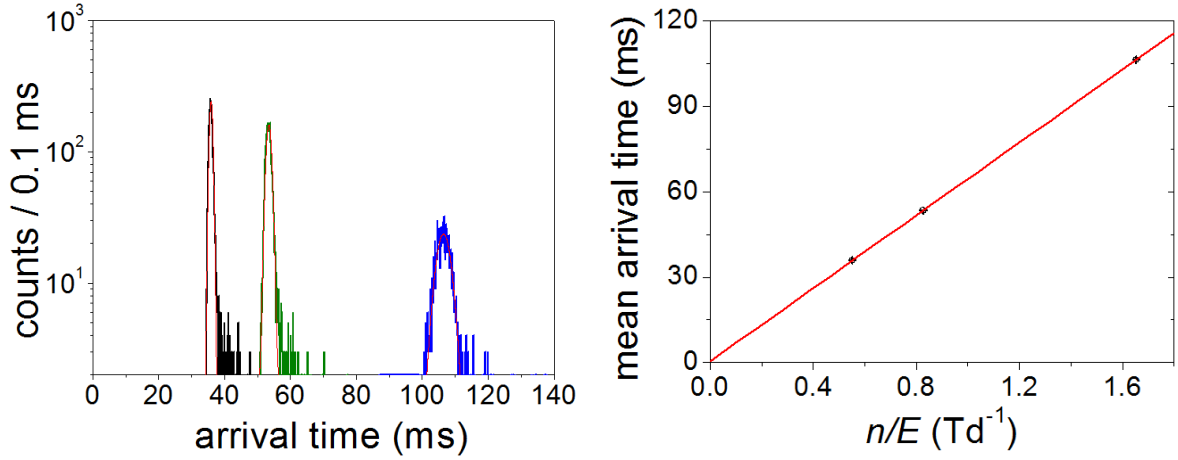


Figure 6.5: Left: Superimposed time spectra of $^{174}\text{Er}^+$ obtained at different E/n values (from left to right: 1.8 Td, 1.2 Td and 0.6 Td) but for the same counting time of 1000 s and at the same cell pressure of 40 mbar Ar. The peak tailing is caused by slow molecular ions that dissociate to give Er^+ within the supersonic gas jet inside the extraction chamber. Right: The linear dependence of the mean arrival time obtained from the left plot on the $(E/n)^{-1}$ value.

which may influence the ATD peak shape [120, 121]. In most IMS measurements, low ion densities can be assumed such that space charge repulsion effects can be neglected and therefore are not accounted for in this equation. At small E/n values, the two diffusion coefficients, D_L and D_T , are equal to one another ($D_L = D_T = D$) and are simply related to the ion mobility K by the Nernst-Townsend-Einstein relation, Eq. (2.2). Furthermore, postulating that created ions do not undergo reactions in the noble gas legitimates to set the reaction frequency parameter α_c equal to zero.

Assuming that Eq. (6.1) describes very well the ionization volume of 4 mm diameter, and that most investigated ions have a mobility of $K_0 \approx 1.9 \text{ cm}^2/\text{Vs}$ at room temperature, the factor $\left[1 - \exp\left(-\frac{\rho^2}{4D_T t}\right)\right]$ may be approximated by $\left(\frac{\rho^2}{4D_T t}\right)$ for an expected mean drift time > 10 ms. Equation (6.1) may be then simplified into

$$\Phi(0, z, t) = \frac{\hat{s} \cdot A_0 \cdot \rho^2}{16\sqrt{\pi} (Dt)^{3/2}} \left(v_d + \frac{z}{t}\right) \exp\left(-\frac{(z - v_d t)^2}{4Dt}\right). \quad (6.2)$$

Gaussian data fits as well as fits according to Eq. (6.2) are shown in Fig. 6.4. For an unambiguous assignment of both fits, the same plot is magnified around the peak maximum and shown in the upper corner of the figure. The Gaussian peak is found to be at (27.648 ± 0.011) ms. Taking the statistical errors into account, the latter value is found to be in good agreement with the corresponding value determined by Eq. (6.2), and henceforward only Gaussian fit routines are used in the ATD analysis.

The influence of the electrostatic drift field on the arrival time distributions could be experimentally verified using resonantly ionized ^{174}Er starting inside the cell at a distance of 32 cm from the extraction nozzle. In these experiments, different E/n parameters have been tested as described in Sect. 5.3 resulting in the superimposed time spectra shown in Fig. 6.5 (left plot). The guiding potentials inside the extraction chamber are decreased in $\Delta U_Q = 2.16$ V steps instead of the usually used 10 V steps. The time spectra illustrate the increasing effects of peak broadening by longitudinal diffusion and intensity loss due to transverse diffusion as the electric field is decreased. For instance, decreasing E/n from 1.2 Td to 0.6 Td in Fig. 6.5 (left plot) results in ion diffusion losses of about 15 % at 40 mbar argon. Increasing E/n values, however, does not necessarily induce higher extraction efficiencies, since the latter strongly depend on the friction forces acting on the ions arriving at the nozzle cone as discussed in Sect. 5.1.4.

In Fig. 6.5 (right plot), the mean arrival time $\langle t_a \rangle$ of $^{174}\text{Er}^+$ obtained from the left spectra of the same figure are shown vs. the corresponding $(E/n)^{-1}$ values. The linearity of the drift velocity v_d on the applied electric field according to Eq. (2.1) can be easily inferred from this plot, since $v_d \propto 1/t_d$. The linear fit in this plot intersects with the time axis at a non-zero value of $580 \pm 40 \mu\text{s}$ corresponding to a mean transit time $\langle t_t \rangle$, which the ions exhibit inside the detection part of the spectrometer. A much more precise method for determining $\langle t_t \rangle$ is described in Sect. 6.4. The mean value of the transit time obtained in that part is about 3 times smaller than the one obtained from Fig. 6.5 (right plot), which is traced back to the different guiding potentials used in these two cases.

Additionally, it has been observed that increasing the cell pressure at the same electric field results in a linear increase of the drift time and consequently a linear decrease of the mobility K of Er^+ as expected from Eq. (2.5). Such a linearity behavior has already been shown in Fig. 5.5 for ^{215}Po ions drifting in argon.

6.3.1 The time resolution

The time resolution is proportional to the drift field, but inversely proportional to the temperature [122]. According to the Einstein relation (Eq. (2.2)), the diffusion coefficient is proportional to the gas temperature at “low-field” conditions. At a constant E/n value, relatively high gas temperatures result in broadened ATD peaks and reduce the time resolution of the spectrometer. In addition, decreasing the drift field causes the ions to drift for a longer time period inside the cell, which results in broadened peaks due to diffusion (compare the time spectra shown in Fig. 6.5 (left plot)). Hence, the major factors determining IMS peak shape are the initial time distribution of the bundle of ions starting to drift inside the cell and the diffusional broadening of the bundle as it travels to the detector [123]. If the initial time distribution of the ions is

of Gaussian shape, the resolving power $\langle t_d \rangle / FWHM_{t_d}$ can be calculated as [124, 125]

$$R_d = \langle t_d \rangle / FWHM_{t_d} = \frac{1}{\sqrt{\left(\frac{w_0}{\beta P_{cell}}\right)^2 + \left(\frac{16 \ln 2 k_B T}{q E d_d}\right)}}, \quad (6.3)$$

with the drift cell pressure P_{cell} , the ion charge q , the drift distance d_d , the electric field strength E and the absolute temperature T . The parameter w_0 in Eq. (6.3) describes the temporal FWHM of the initial time distribution of the ions created via RIS methods, whereas the coefficient $\beta = t_d / P_{cell}$ is a linearity constant that can be obtained by measuring the time spectra at different buffer gas pressures. The term $\left(\frac{w_0}{\beta P_{cell}}\right)^2$ in Eq. (6.3) describes the contribution to the resolving power solely due to the temporal shape of the initial pulse. The contribution caused by diffusion for an infinitely narrow initial pulse is given by the term $(16 \ln 2 k_B T / q E d_d)$ [123].

Equation (6.3) shows that at constant T and E , the resolving power generally increases with pressure. However, for the narrowest initial pulse width w_0 , it rapidly stagnates at a value, which is mainly determined by the applied electric field E , the temperature T and the drift distance d_d [124]. For ionization using laser beams of 1 mm diameter, the term $\left(\frac{w_0}{\beta P_{cell}}\right)^2$ in Eq. (6.3) is about 200 times smaller than the diffusion term $(16 \ln 2 k_B T / q E d_d)$ and may be neglected [6]. Hence, the electric field strength E is the only parameter that limits the resolving power for a specific drift length at room temperature. The highest applicable field E_{max} , however, is practically limited by the insulation length of the used electrical feedthroughs inside the drift cell, see Sect. 4.1.1. The field E_{max} is found to be about 18 V/cm at 40 mbar argon, which results in the highest achievable resolving power of ≈ 45 for $q = e$, $d_d = 32$ cm and $k_B T = 25$ meV.

Instead of Eq. (6.2), using Gaussian fit routines in the analysis of measured time spectra allows for a rather good prediction of the ATD mean $\langle t_a \rangle$ and its corresponding standard deviation σ_a . By neglecting the peak broadening due to the initial time distribution of the ions, the resolving power may be related to the normalized standard deviation of the arrival time $\sigma_a / \langle t_a \rangle$ via

$$R_d = \frac{1}{2.35 \cdot \sigma_d / \langle t_d \rangle} \approx \frac{1}{2.35 \cdot \sigma_a / \langle t_a \rangle}, \quad (6.4)$$

whereas the normalized standard deviation of the drift time $\sigma_d / \langle t_d \rangle$ is approximated by $\sigma_a / \langle t_a \rangle$. The latter approximation is justifiable only for a negligibly small transit time t_t with respect to the drift time t_d , see also Sect. 6.4. The normalized standard deviation of the arrival time obtained with the developed apparatus is found to be one order of magnitude less than the one obtained in Ref. [51] and [113]. The drift cell described in these references is designed mainly for laser spectroscopy experiments on the actinides and transactinides and has not been optimized for mobility measurements. It exhibited a relatively smaller drift distance d_d , which inevitably results in higher $\sigma_a / \langle t_a \rangle$ values even though other experimental parameters like P_{cell} , T and E are approximately equal to the parameters presented in this work.

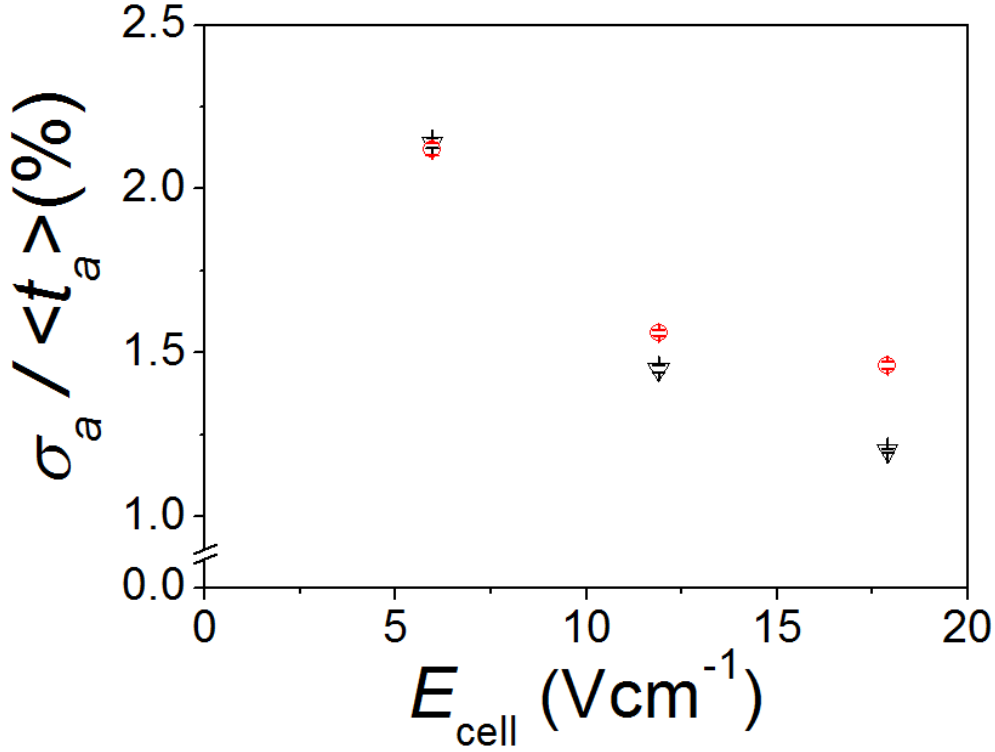


Figure 6.6: Normalized standard deviations of ATDs $\sigma_a / \langle t_a \rangle$ for Er^+ drifting in 40 mbar argon vs. different electric fields inside the cell. The higher values at the same fields (\circ) are obtained when the potential difference between the neighboring QPIG segments inside the extraction chamber is decreased to 2.16 V instead of the usually applied 10 V (∇).

Figure 6.6 shows $\sigma_a / \langle t_a \rangle$ values for Er^+ vs. different electric fields inside the cell. The time spectra are obtained by using a narrow ionizing laser beam of 1 mm diameter shining on the top of the Er-filament at 32 cm distance from the extraction nozzle. Generally, increasing the field results in smaller $\sigma_a / \langle t_a \rangle$ values ($\sim \sqrt{1/E_{\text{cell}}}$) as can be inferred from Eq. (6.3) and Eq. (6.4). Nevertheless, the potential gradient between the QPIG segments is found to be a crucial parameter, which strongly influences the time spectra at a background pressure of $P_{1\text{section}} = 4.5 \cdot 10^{-2}$ mbar in the first pumping section. Increasing the potential gradient between the QPIG segments in that section results in significantly smaller transit time values, and hence in less peak broadening due to diffusion. In Fig. 6.6, the higher value (marked in red) at the same drift field is obtained when the potential difference between each neighboring QPIG segments inside the extraction chamber is set to $\Delta U_Q = 2.16$ V. For mobility measurements, however, smallest line widths are envisaged such that ΔU_Q is increased to 10 V (triangles in the same figure) between the first six QPIG segments. In fact, increasing ΔU_Q would reduce the transit time values further and further, resulting in less diffusional broadening of the ATD peaks. Elevated ΔU_Q values, however, bear the risk of gas discharges between

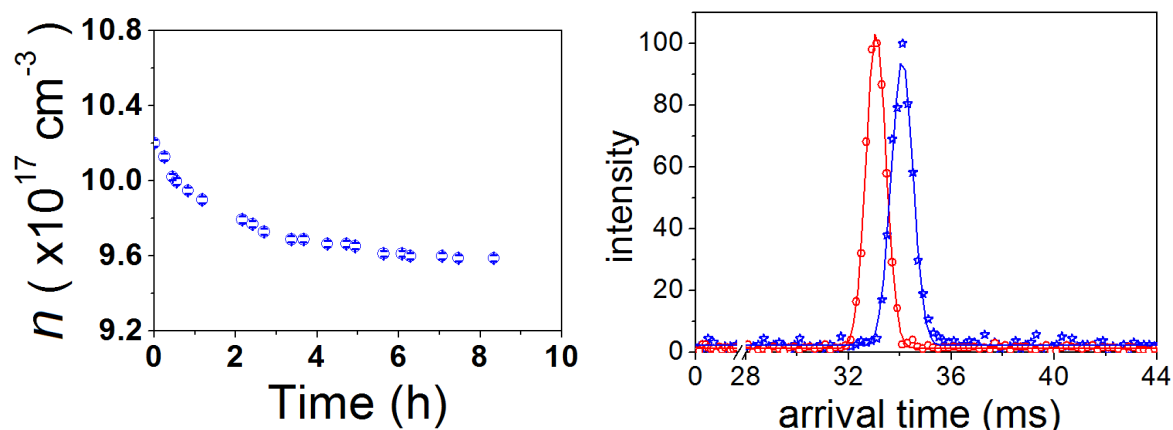


Figure 6.7: Left: Gas number density n obtained for a cell pressure of about 40 mbar and a filament temperature of $T_{Fil} = 1220$ K. Right: ATDs of Ho^+ ions drifting in ≈ 40 mbar argon at a mean field of 17.9 V/cm. The pressure difference of about 1.3 mbar leads to a time shift of 1 ms in the measured ATD peaks.

the QPIG segments and have not been tested so far. According to Fig. 6.6, diffusion processes inside the extraction chamber may deteriorate the relative width of the ATD peaks and result in a lower resolving power of the apparatus, especially at small guiding potentials and elevated background (see also Sect. 6.4).

Furthermore, the cell pressure is an important parameter as well, not only due to Eq. (6.3), but also because it is desirable to keep the drifting ions in the “low-field” limit such that the Einstein relation (Eq. (2.2)) still applies. At high fields the mobility depends on the drift voltage, such that it is considerably more difficult to relate the mobility to the geometry [2]. So in order to substantially increase the voltage across the drift tube, it is necessary to increase the buffer gas pressure.

6.3.2 Pressure effects

Equation (2.5) states that the mobility K is inversely proportional to the gas number density n , which corresponds to a certain pressure at a fixed temperature T . Gas temperature variations cause pressure changes and may result in erroneous mobility data. During the measurements, the gas temperature is manually recorded using a type K thermocouple (B+B Thermo Technik, type K, NiCr-Ni) installed in about 15 cm distance from the sample filaments, whereas the cell pressure, monitored by a compact capacitance gauge in conjunction with its operating unit, is read out by the VI program presented in Appendix B.2.

Before starting any mobility measurement, it is essential to wait until the gas temperature and the cell pressure equilibrate. Figure 6.7 (left plot) shows a typical trend in

the gas number density n after adjusting the desired pressure and starting to evaporate from the sample filaments (at $t=0$). According to the plot, reasonable low density variations are achieved after 6 to 8 hours in case of 40 mbar argon, which make the mobility measurements rather time consuming.

The right-hand plot of the same figure shows two arrival time distributions of evaporated and resonantly ionized holmium drifting in about 40 mbar argon. The diameter of the laser beam providing the first excitation step ($\bar{\nu}_{12} = 24660.8 \text{ cm}^{-1}$) is kept quite small (2 mm) in order to get sharp ATD peaks (see the next section for more details). The time shift of 1 ms between both spectra is caused by the pressure difference of about 1.3 mbar between the measurements carried out with the same filament. Nevertheless, such time shifts may be neglected at equilibrated pressures. For instance, 4 hours after gas admittance into the cell operated at 40 mbar Ar (as shown in the left plot of Fig. 6.7), the pressure variation over time amounts to 0.01 mbar/10 min, which corresponds to a time shift of about 10 μs for measurements carried out sequentially within 10 minutes.

6.3.3 The influence of the laser beams

The normalized standard deviation of measured arrival time distributions is found to be strongly affected by the dimensions of the ionization volume above the filament. Figure 6.8 shows the $\sigma_a/\langle t_a \rangle$ values vs. different laser beam diameters used for ionizing evaporated erbium at 40 mbar argon. In these measurements, both laser excitation wavelengths are coupled into one multi-mode silica glass fiber and guided to the IMS experimental setup as shown in Fig. 4.8.

Obviously, decreasing the beam diameter enhances the time resolution and decreases the normalized standard deviation of the arrival time distributions. This behavior may be traced back to the spatial distribution of the ions inside the ionization volume. Especially the variety in the longitudinal starting positions of the investigated ions strongly influences the ATD peak broadening as predicted by Eq. (2.3).

For studying the transversal extension of the ionization volume, the two excitation wavelengths may be decoupled from each other by using two optical fibers of the same length. Hence, ionization takes place only in the volume above the filament where the two laser beams overlap. Time spectra of Ho^+ ions drifting in 43.5 mbar Ar are shown in Fig. 6.9. The upper distribution is obtained while decoupling the two excitation wavelengths as proposed before. In this scenario, the intersection angle of the beams is about 143° . The diameter of the laser beam providing the first excitation step is reduced to 0.8 mm, whereas the beam of the excimer laser is kept quite large (6 mm) to guarantee its spatial overlap with the first one. The resulting normalized standard deviation is found to be 1.6%. Surprisingly, a better result is obtained if both laser beams are coupled into only one fiber. The lower distribution in the time spectrum shown in Fig. 6.9 is obtained for the same conditions as the case mentioned before. The main difference now is that both excitation wavelengths are provided by one laser

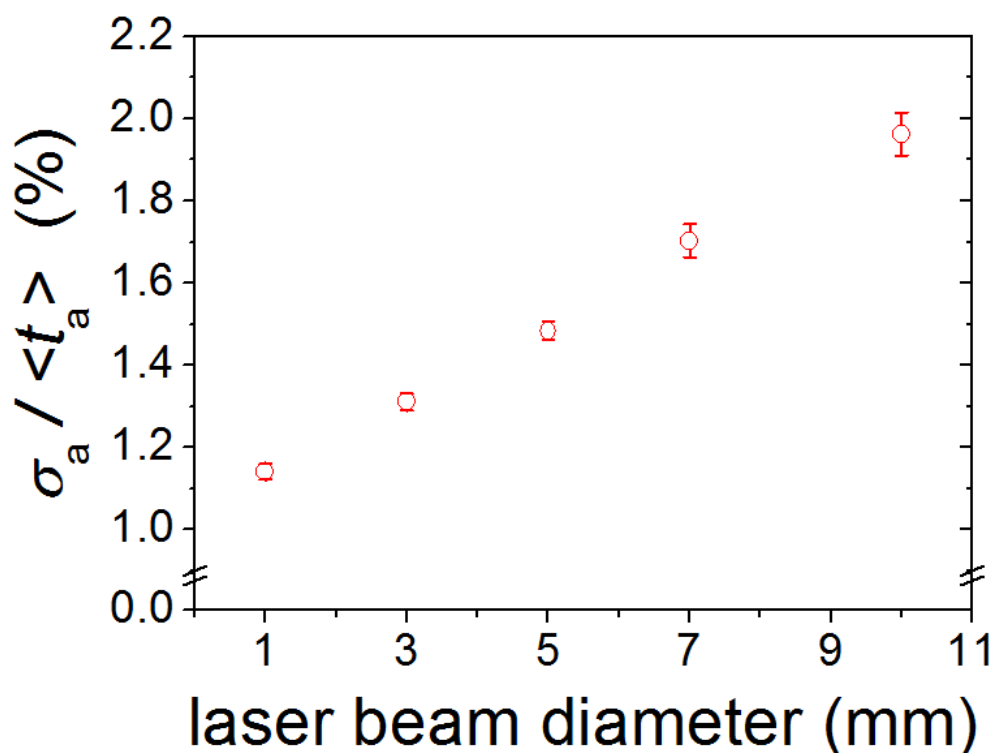


Figure 6.8: The normalized standard deviation $\sigma_a / \langle t_a \rangle$ for Er^+ vs. laser beam diameter. The measurements are carried out at $E/n = 1.8 \text{ Td}$ and 40 mbar cell pressure. The drift distance is about 32 cm.

beam of 0.8 mm diameter shining on the top of the filament. The low number of registered counts in this spectrum is due to a misalignment of the laser focus with respect to the optical fiber, see Fig. 4.8. In both mentioned cases, the photon flux for the excitation step corresponding to $\bar{\nu}_{12}$ is attenuated in order to avoid multiphoton ionization processes of sample atoms, which may occur anywhere along the laser beam inside the cell. However, coupling of the excitation wavelengths into one fiber according to Fig. 4.8 results in a normalized standard deviation $\sigma_a / \langle t_a \rangle$, which is decreased by a factor 1.45 compared to the case of crossed laser beams.

6.3.4 Ionization above the filament

Figure 6.10 (a) shows the measured count rates of evaporated and resonantly ionized erbium vs. different starting positions above the 3.5 mm narrow filament. For the performed 2D-scans, a laser beam containing both excitation wavelengths is used. Its diameter is fixed to 3 mm, such that a sufficiently high count rate even far away from the filament can be obtained. The white areas in the plots stand for missing measurement results due to geometrical constraints. The count rates as well as their spatial distribution depend on the filament temperature [50, 126]. The velocity of the evaporated atoms due to convection is estimated to be 100 m/s [51], whereas the mean

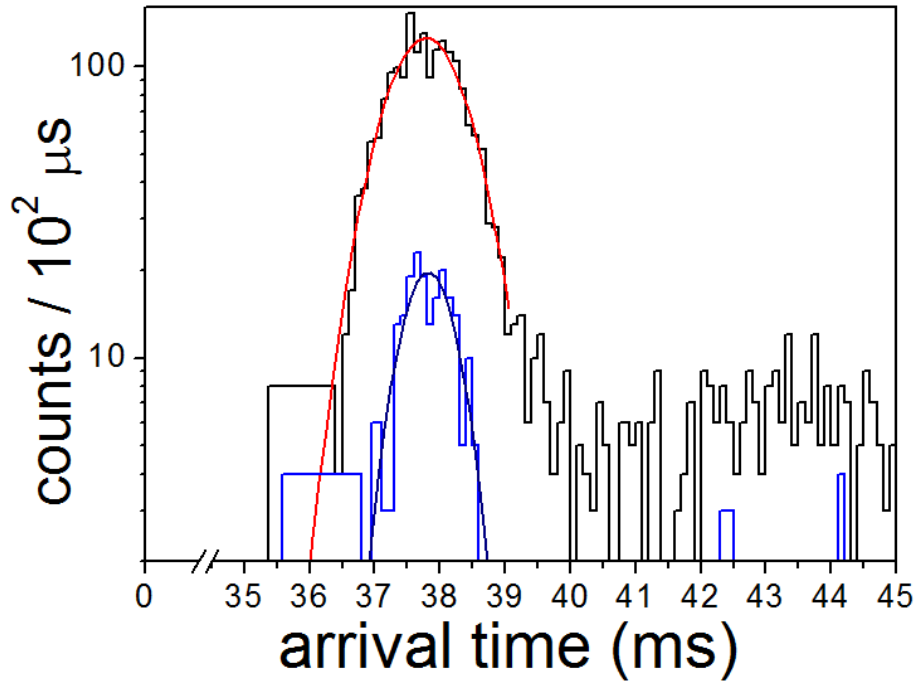


Figure 6.9: ATD of Ho^+ ions drifting in 43.5 mbar argon at $E/n = 1.7 \text{ Td}$. The upper distribution is obtained when ionizing holmium by two crossed laser beams of suitable wavelengths. The first excitation step is set at the Ho resonance $\bar{\nu}_{12} = 24660.8 \text{ cm}^{-1}$ according to Tab. 3.2. The lower distribution is obtained when both wavelengths are coupled into one laser beam as shown in Fig. 4.8.

velocity gained by diffusion is negligibly small (0.1 m/s) [50]. The highest count rates are obtained above the filament as expected.

Generally, shorter drift distances result in decreased ATD means $\langle t_a \rangle$ as can be seen in Fig. 6.10 (b). The filament is operated at an optimized potential of 954 V according to Tab. 3.2, which produces an almost homogeneous electric field within the drift region. Nevertheless, the latter gets perturbed in the immediate vicinity of the filament, such that drifting ions lose or gain velocity depending on their starting position. One may divide the plot into two main regions: one on the right-hand side characterized by relatively small drift times and another one dominated by increased ATD means on the left. The distance between the different isolines shown in the timing landscape implies the magnitude of the ATD means to change at different positions (y, z) . This change has to be as small as possible during the envisaged mobility measurements in order to reduce systematic errors.

According to Fig. 6.10, the optimum position for resonance ionization would be $(y, z) = (6 \text{ mm}, 4 \text{ mm})$, since then relatively large count rates without significant variations in the $\langle t_a \rangle$ values due to small position variations are expected. The normalized standard deviation $\sigma_a / \langle t_a \rangle$ at this position amounts to about 1.2% when using laser beams of 3 mm diameter.

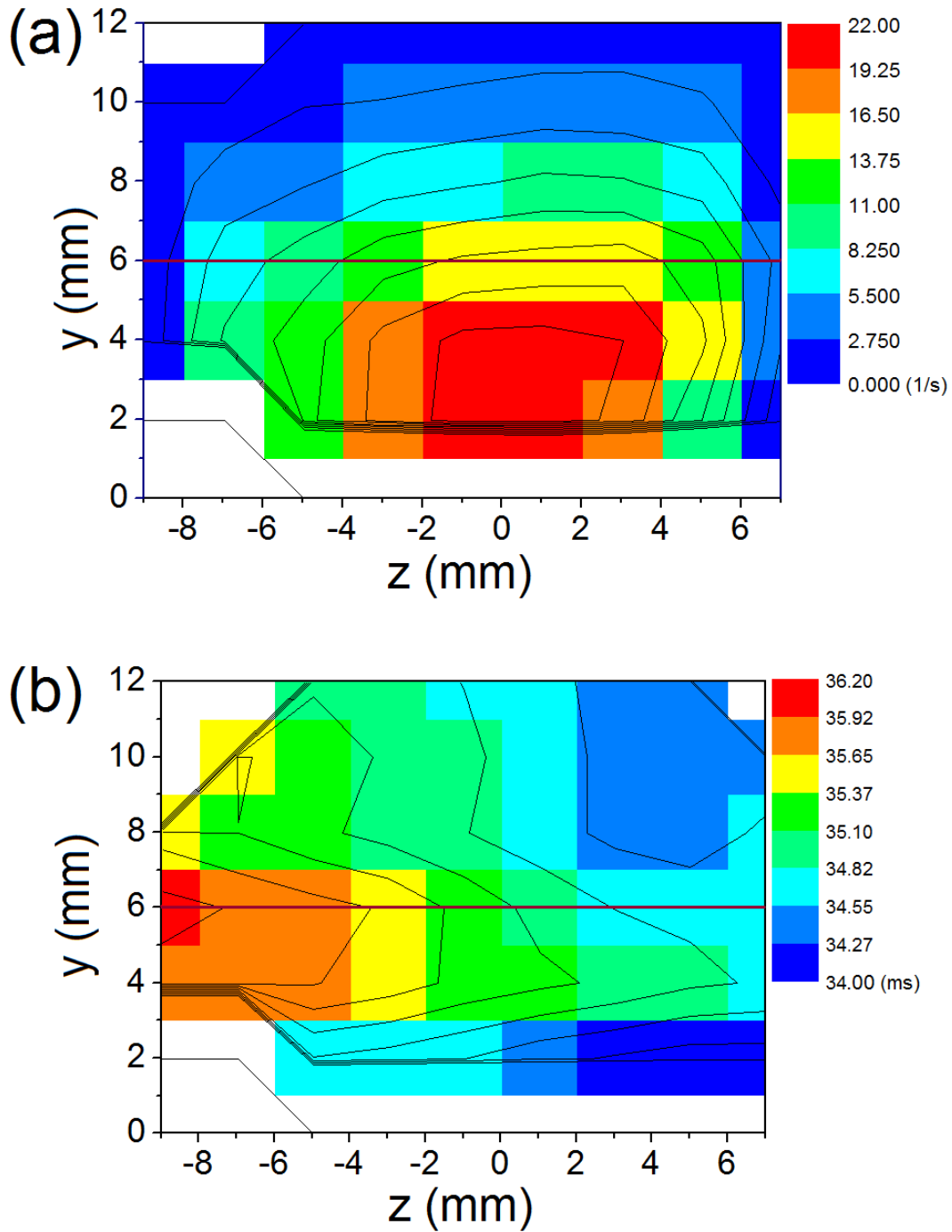


Figure 6.10: (a): Count rates (in $1/s$) of evaporated and resonantly ionized erbium vs. their starting positions above the filament. Also shown are the iso-lines of the registered count rates. The measurements are performed at a cell pressure of 40 mbar and an E/n parameter of 1.8 Td. The filament temperature amounts to 1100 K. In the plot, the Er filament is located at the origin of the coordinate system and the ions always drift towards increasing z values. (b): The corresponding means of the arrival time $\langle t_a \rangle$ (in ms). The symmetry axis of the drift cell is marked in both plots at $y = 6$ mm.

6.4 The transit time of extracted ions

According to Eq. (3.1), the drift time of the ions inside the cell is obtained from their arrival time t_a and the transit time t_t , which the ions need for traveling from the nozzle to the channeltron detector. The latter time offset t_t is negligibly small in most IMS devices. In the apparatus described here, however, it may become important, especially at elevated background pressures in the extraction chamber.

Exploiting the triggering feature of the nozzle potential, separation of the two ATD components becomes possible, as will be explained in the following. Figure 6.11 (a) shows calculated trajectories of $^{215}\text{Po}^+$ drifting in 40 mbar argon. Except the nozzle voltage, all electrode potentials are applied according to Tab. 3.2. In this plot, two nozzle potentials of $U_{Noz} = +216\text{ V}$ and $U_{Noz} = +126\text{ V}$ have been used. All ions are defocused in the first case and subsequently hit the first electrode, whereas in the other case the ions are transmitted to the extraction nozzle. If the ions are transmitted, broad and Gaussian-like ATD peaks are obtained (see Fig. 6.11 (b)), which holds for all mobility measurements presented in this work. Figure 6.11 (b) shows such a time spectrum (black histogram) measured for Ho^+ drifting in 40 mbar argon. It should be mentioned that $t_0 = 0$ in this plot does not refer to the starting time of the ions as it usually used to be (at the mentioned conditions, the drift time of holmium ions is expected to be in the range between 34 ms and 36 ms). By implementing the triggering scenario described above, one may reject most of the ions arriving at the nozzle and allow only a few of them to be transmitted.

During the transit time measurements with Ho^+ ions, U_{Noz} is triggered between +216 V and +126 V by a fast HV switch coupled to two HV modules as described in Sect. 4.3. The electric circuitry of this switch can be seen in Fig. B.3. The pulse structure of the nozzle potential is shown in the upper part of Fig. 6.11 (b). All ions get lost by applying $U_{Noz} = +216\text{ V}$, whereas at the switching time $t_1 = 16.4\text{ ms}$, the residual drifting ions begin to traverse the distance of $d_r \approx 7\text{ mm}$ between the first electrode and the nozzle throat. The fastest Ho^+ ions are then registered after a time delay of $t_{delay} = 450\text{ }\mu\text{s}$. For more clarity, the obtained time spectrum (blue histogram in the same figure) is called the transit time spectrum. It shows a risetime of about $60\text{ }\mu\text{s}$, which is mainly determined by the spatial distribution of the ions close to the nozzle at the time of the switching of the potential and their diffusion within the remaining distance d_r . The fall time of the nozzle potential of about $2\text{ }\mu\text{s}$ is small in comparison to the risetime of $60\text{ }\mu\text{s}$ and can be neglected. The standard deviation of the transit time distribution is obtained by a Gaussian fit from the left up to nearly one σ to the right side of the peak. The tail of this spectrum is dominated by diffusion of delayed ions arriving at the nozzle cone when ion transmission is enabled.

In Fig. 6.12, the standard deviations obtained from the analysis of the arrival time distributions and of the transit time spectra are shown. As can be seen in this figure, the width of the ATD peaks may be reduced at elevated pressures [125] in accordance with Eq. (6.3) but this seems to be a small effect. Noteworthy is also the effect of the guiding electric field $E_{1section}$ inside the extraction chamber, which gives new insights into the

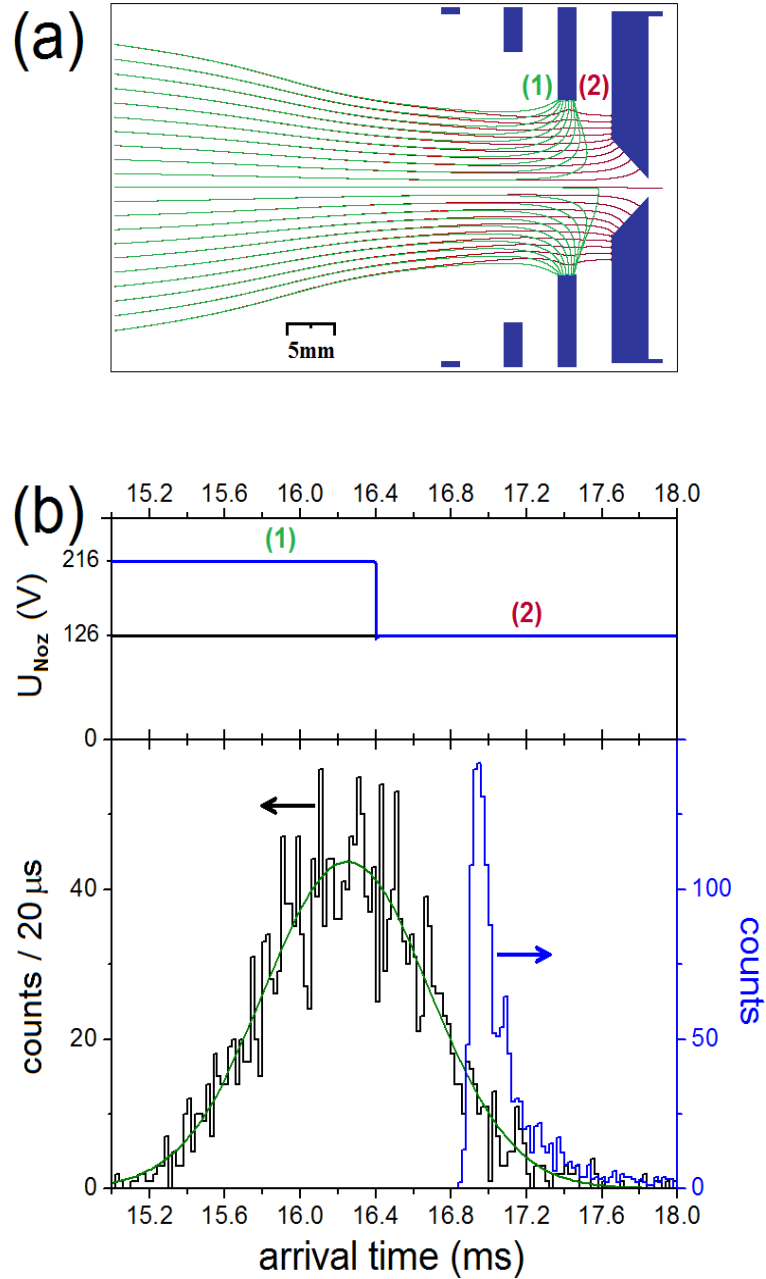


Figure 6.11: Principle of transit time measurements. (a): Trajectories of $^{215}\text{Po}^+$ drifting in 40 mbar argon obtained with the computer code SIMION. In the simulations, two nozzle potentials of +216 V (1) and +126 V (2) have been tested. The potentials of the remaining electrodes are according to Tab. 3.2. (b): Measured ATDs of Ho^+ drifting in 40 mbar argon at an $E/n = 1.8 \text{ Td}$. The black histogram is obtained in the transmission mode where a static potential $U_{\text{Noz}} = +126 \text{ V}$ is applied. Note that $t_0 = 0$ for this plot does not refer to the starting time of the ions. Triggering U_{Noz} according to this plot results in the time spectrum of the blue histogram, which allows to determine the mean transit time of the ion distribution in front of the nozzle at the time of the potential switching to the detector.

diffusion phenomena prevailing there. The ATD peaks get broadened by decreasing the latter from 6.3 V/cm (circles) to 1.4 V/cm (squares in the same figure). The widths (in terms of σ) of the transit time spectra are roughly one order of magnitude smaller than those in the corresponding arrival time distributions. The temporal broadening in the transit time peaks is caused by ion diffusion in the remaining drift distance and in the first pumping section, where small mean free paths for gas collisions are expected, see Sect. 3.3.3. For an increased guiding field $E_{1section} = 6.3$ V/cm (corresponding to $\Delta U_Q = 10$ V, which is the standard configuration for mobility measurements presented in chapter 8), smaller widths of the transit time peaks may be achieved at 40 mbar Ar, which reflect the big impact of the remaining drift distance d_r on the transit time spectra. Applying a weak guiding field of 1.4 V/cm (corresponding to $\Delta U_Q = 2.16$ V) results in an increased storage time of the ions inside the extraction chamber especially at a high background pressure. One may conclude that the impact of the diffusion inside the ion guide on the ATDs is rather small if high potential gradients are chosen between the neighboring QPIG segments according to Tab. 5.2.

The time delay t_{delay} is found to be strongly affected by the parameter E/n . It is clear that most of this time elapses during the ion drift inside the cell. Measuring t_{delay} at two different E/n values may be sufficient to determine the mean transit time at $(E/n)^{-1} \rightarrow 0$ (compare Fig. 6.5) at which the drift time needed for traversing the distance d_r may be neglected. For instance, Fig. 6.13 shows the obtained time delay in the transit time spectra measured for two different E/n values, but for the same cell pressure and at the same guiding field inside the extraction chamber of $E_{1section} = 6.3$ V/cm. Applying the highest possible potentials results in a time delay $t_{delay} = 450$ μ s at an E/n value of about 1.8 Td. In Fig. 6.13, the intersection of the linear fit with the time axis delivers a mean transit time of $\langle t_t \rangle = t_{delay}((E/n)^{-1} \rightarrow 0) = (182 \pm 12)$ μ s. The latter does not depend on the E/n parameter and is expected to be similar within the given errors for all kind of ions, for which the mobility have been measured in this work. It has to be subtracted from the ATD means in accordance with Eq. (3.1) in order to get the corresponding mean drift time $\langle t_d \rangle$.

6.5 Consequences drawn from time resolution studies

It has been demonstrated in Sect. 6.3.2 that smallest changes in the buffer gas pressure or rather the gas temperature lead to significant time shifts in the arrival time distributions of the same element. This effect dominates all measurements taking place immediately after buffer gas admittance into the drift cell. Therefore, it is highly important to wait more than 6 hours before beginning with the proper mobility investigations, since then variations of the pressure and the gas temperature would be equilibrated and therefore not any more have a big impact on the systematic errors of the mobility data. In addition, a realignment of the sample lanthanide filament is required each time the latter is installed inside the cell. This procedure may result in different filament positions, on the one hand with respect to the electrodes, and on

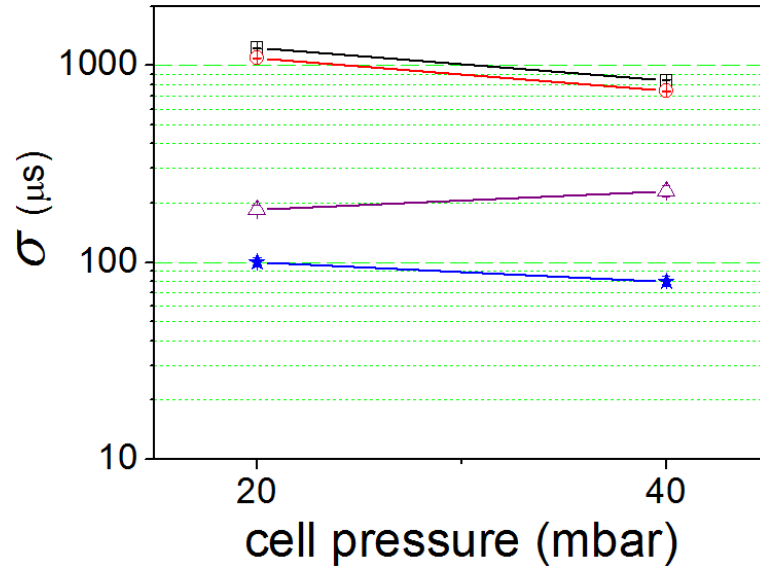


Figure 6.12: Temporal standard deviation σ of the arrival time and of the transit time peaks for different guiding potentials in the QPIG sections as function of the buffer gas pressure. The measurements are carried out at an E/n value of 1.2 Td. The standard deviation for the ATD peaks (\square) and (\circ) and for the transit time peaks (\triangle) and (\star) correspond to a different potential difference between the neighboring QPIG segments inside the extraction chamber, which is set to $\Delta U_Q = 2.16$ V and 10 V for the upper and lower curves, respectively.

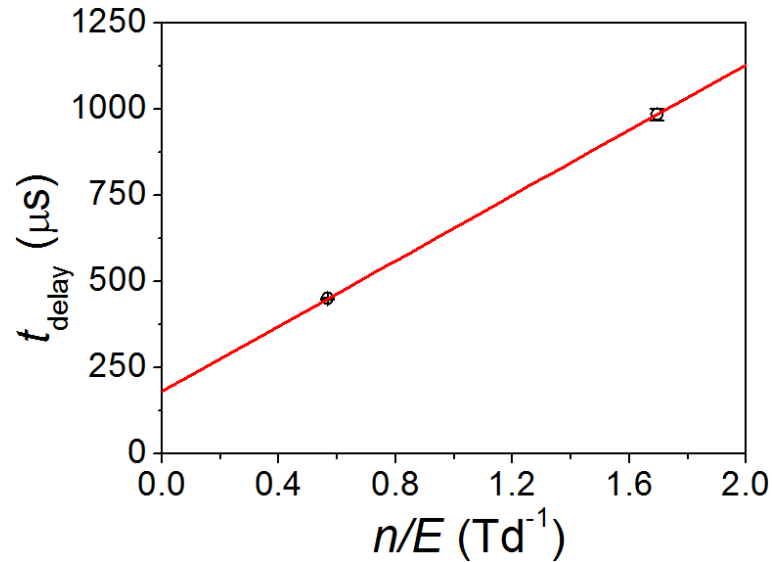


Figure 6.13: A method to determine the transit time of sample ions. As an example, the plot shows the obtained time delay t_{delay} of Ho^+ drifting in 41.7 mbar argon at different E/n values. For $(E/n)^{-1} \rightarrow 0$, the drift time the ions need to traverse the distance d_r may be neglected such that the intersection of the linear fit with the time axis delivers the desired mean of the transit time $\langle t_t \rangle = t_{\text{delay}}((E/n)^{-1} \rightarrow 0)$.

Table 6.1: Melting point T_m [127] and vapor pressure P_{vap} at a temperature of $T = 1100$ K [128] of some lanthanide elements. Values are sorted with respect to the vapor pressures.

	Yb	Eu	Dy	Ho	Er	Tb	Gd
T_m [°C]	824	822	1411	1472	1529	1359	1313
P_{vap} [Torr]	18	0.8	$2.1 \cdot 10^{-5}$	$8.0 \cdot 10^{-6}$	$1.3 \cdot 10^{-6}$	$2.2 \cdot 10^{-9}$	$7.0 \cdot 10^{-10}$

the other hand with respect to the ionizing laser beam. However, different filament positions result in modified electric fields as well as in different starting positions of the ions, which make any comparison of lanthanide mobilities less convincing. Also the differences in the evaporation temperatures of the investigated elements may affect the mobility of the ions near the filament and hence impair the reproducibility as well as the accuracy of the measurements.

The easiest way to reduce such systematic errors is to measure the mobility of all considered elements in one run and at the same conditions. This method, however, has proven to be quite challenging, partly due to the failure of the element identification procedure presented in Sect. 6.2. The achievable mass spectra are then difficult to interpret, because the isotopic mass of certain elements may coincide with the molecular mass of oxides and hydroxides of other lanthanides under consideration (see also Sect. 7.1.1). Furthermore, the different elements investigated in this work, i.e. Yb, Er, Ho, Dy, Tb, Gd and Eu have entirely different vapor pressures at a given temperature T , as can be seen in Tab. 6.1 and cannot be easily combined with each other. For instance, the vapor pressure of Gd at $T = 1100$ K is several orders of magnitude less than the one of Yb, which renders the combination of both elements into one multi-filament not advisable. The Yb foil would immediately burn out, whereas no Gd signals can be registered due to the higher temperature required for an efficient Gd evaporation.

This problem can be overcome by using multi-filaments consisting of thin foil strips of only one or two lanthanide elements and a reference element, which are ordered to achieve a sandwich structure as schematically shown in Fig. 6.14. The single strips are usually $25 \mu\text{m}$ thick, 1 mm wide and 25 mm long. Holmium, chosen as a reference element, is permanently included in all used multi-filaments in order to normalize all obtained time spectra to the arrival time distributions of Ho^+ ions. The element holmium is well-suited, because it has only one stable isotope and can be clearly identified in the mass spectra and also due its evaporation temperature, which is not too high as for Gd and not too low as it is the case for Yb and Eu. In such a way, elements of considerably different evaporation temperatures may be investigated independently.

Figure 6.15 shows superimposed mass spectra obtained after laser resonance ionization of evaporated gadolinium and holmium atoms. The measurements are performed in a consecutive manner such that atoms of only one element are resonantly ionized for each obtained mass spectrum. The used Gd-Ho multi-filament is heated up to $T_{Fil} =$

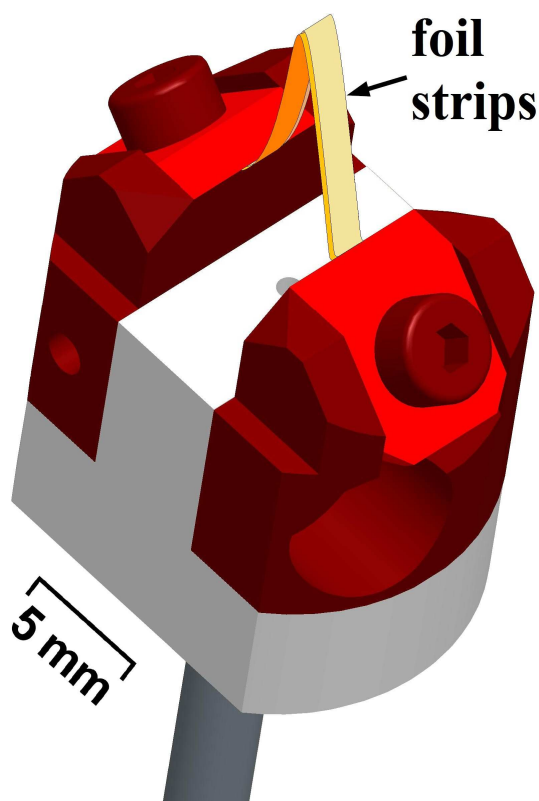


Figure 6.14: Example of multi-filaments as used during mobility experiments.

1220(50) K in order to produce enough Gd vapor. According to this figure, both Ho^+ as well as Gd^+ can be clearly distinguished from each other by combining the element-selective laser resonance ionization technique with the isotopic mass separation methods.

Nevertheless, working with multi-filaments containing element isotopes of similar masses bears the risk of being unable to clearly assign the obtained ATDs to the corresponding elements. Furthermore, gas impurities enhance the formation of molecular ions of the relevant elements, which may hamper the isotope selectivity of the QMS. It is therefore preferable to avoid the combination of elements, which may deliver complicated mass spectra in conjunction with their corresponding molecules. Stable gadolinium isotopes, for instance, may react to give GdO^+ with masses that coincide with the masses of the different stable ytterbium isotopes. Therefore, studying the chemical reactions of the sample ions and how the mass and time spectra are influenced by such effects gains importance, especially when working with several lanthanide elements at the same time.

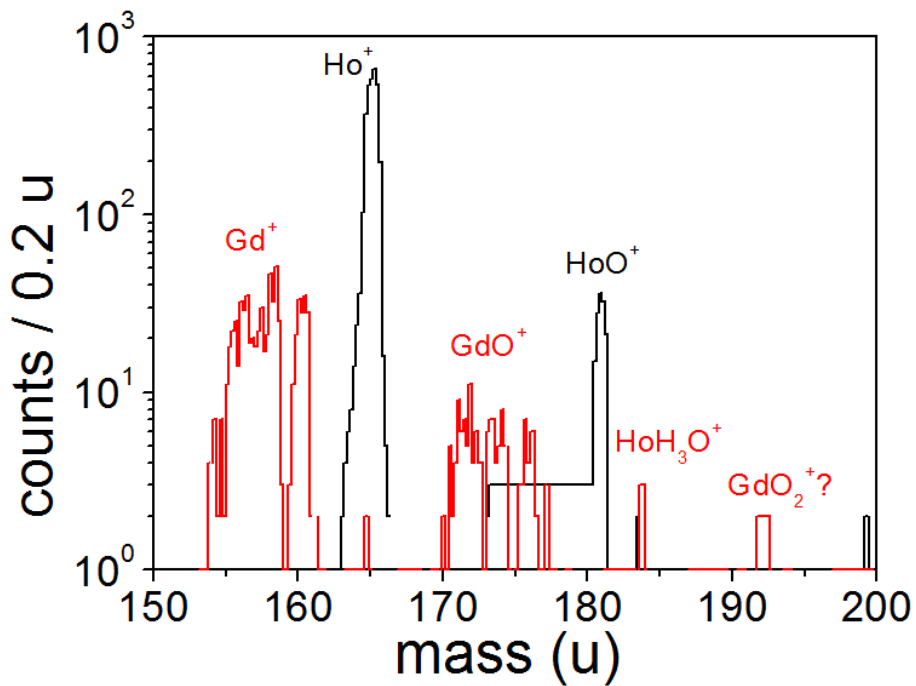


Figure 6.15: Superimposed mass spectra obtained after laser resonance ionization of evaporated gadolinium (red histogram) and holmium (black histogram) atoms. The HoH_3O^+ peak in the gadolinium spectrum is due to reactions of the simultaneously evaporated holmium with water ending up with hydroxide molecules, which are non-resonantly ionized by the UV light of the excimer laser (see Sect. 7.1.1). The measurements are performed by working with a Gd-Ho multi-filament at a cell pressure of $P_{cell} = 42$ mbar and an E/n parameter of 1.8 Td.

7 Investigation of ion loss processes and background events

In this chapter, ion loss processes due to chemical reactions and the origin of background events that may perturb the mobility measurements will be explained. Studying such processes facilitate the interpretation of the time spectra and allows for an unambiguous identification of the sample ions when working with multi-filaments.

7.1 Ion loss processes due to chemical reactions

Besides diffusion and electrostatic defocusing of the ions at the nozzle throat, there are many other processes that may contribute to ion losses inside the drift cell. For instance, the ions of interest may react with gas impurities or other evaporated filament constituents and get lost for further investigations. Such reactions can be classified into three main categories:

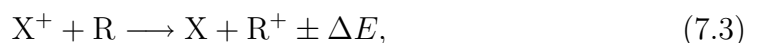
1. Immediately after evaporation, sample atoms X react with gas impurities R to give neutral molecules according to



Bound atoms are considered to be lost for laser resonance ionization as described in Sect. 3.2. However, such molecules existing inside the ionization volume are non-resonantly ionized by the UV light of the used excimer laser, i.e.



2. Ionized lanthanide atoms may undergo chemical reactions and thereby produce charged molecules that, however, are filtered out by the used quadrupole mass filter.
3. Also charge transfer reactions [129] may contribute to ion loss processes via neutralization of the sample ions according to [130]



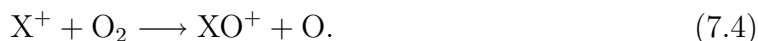
where the energy defect ΔE is made up from the relative kinetic energy of the initial particles.

In addition, the ion loss process due to three-body recombination reactions $X^+ + e^- + \text{Ar} \longrightarrow X + \text{Ar}$ between successfully ionized atoms and free electrons may affect the overall efficiency [91]. For simplicity's sake, such a reaction loss may be included in the evaporation efficiency of filaments and will not be considered in the following discussion.

7.1.1 Chemical reactions

Lanthanides show pronounced similarities in their chemical properties due to the common outer electronic configuration they share [131], as well as due to their similarity in size. In aqueous solutions they tend to adopt the +3 oxidation state [127] that several years ago caused their classification and eventual separation to be an extremely difficult endeavor [132].

During the mobility measurements, gas impurities such as O_2 and H_2O molecules may strongly hamper the awaited signals of the lanthanide ions of interest. Most obtained oxides are created in chemical reactions during the drift of the monoatomic ions



Also the formation of trivalent metal hydroxides has been observed especially for the elements terbium and holmium ending up with XH_3O^+ molecular ions, which are subsequently registered at masses being 19 u heavier than the sample ions. Such hydroxide molecules have been measured in previous experiments [50] for Gd^+ ions, whereas the formation of XO^+ and $\text{XO}(\text{H}_2\text{O})^+$ molecules has been reported in Ref. [113]. Even though oxide as well as hydroxide ions do not much disturb the arrival time distributions due to the mass selective detection feature of the described IMS apparatus (compare the mass spectrum in Fig. 6.15), it may be essential to suppress such chemical reactions by increasing the gas purity inside the cell.

For instance, Fig. 7.1 shows two mass spectra obtained for relatively different gas purities after laser resonance ionization of evaporated gadolinium atoms. Baking out the drift cell for 24 hours at a temperature of 130 °C and activating the getter pump during the measurements helps to enhance the gas purity and to suppress efficiently the chemical reactions and hence increase the extraction efficiency of the sample ions. This scenario is represented by the mass spectrum exhibiting significant contributions of monoatomic Gd ions in Fig. 7.1. Otherwise, if the getter pump has not been activated, most created Gd^+ get lost for mobility investigations due to chemical reactions with gas impurities as shown in the same figure. Of course, such loss processes strongly depend on the chemical reactivity of the sample element, which is quite diverse for the investigated rare earth elements¹. At higher purity levels of the buffer gas, not only oxides but also hydroxide molecules may disappear from the mass spectra such that a clear assignment of the Gd^+ arrival time distributions is achieved. In addition, due

¹Europium, for instance, is one of the most reactive rare earth elements, which rapidly oxidizes in air unlike erbium or holmium [127].

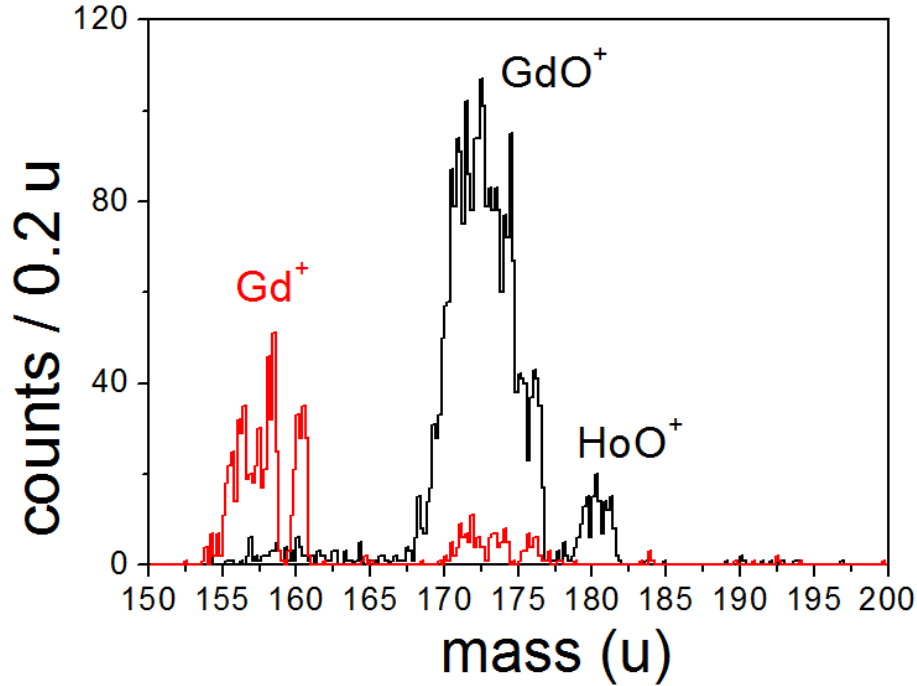


Figure 7.1: Superimposed mass spectra obtained at a scan speed of 10 s/u after laser resonance ionization of evaporated gadolinium atoms. Most created Gd^+ ions oxidize (black histogram) if the requirement of highest gas purities is not fulfilled. Less oxides but high count rates of sample ions are obtained (red histogram) after baking the drift cell to a temperature of 130 °C for 24 hours and activating the getter pump. The spectra are obtained by evaporating gadolinium atoms from a Gd-Ho multi-filament at a cell pressure of $P_{cell} = 40$ mbar ($E/n = 1.8$ Td, $T_{Fil} = 1220$ K).

to the fact that molecular ions are larger in size than monoatomic ions, the latter are detected earlier than their chemical products.

In the simplest cases, the ATD peaks of molecular ions can be identified already in the time spectra without looking at the corresponding ion masses. Figure 7.2 shows a mass-time spectrum obtained after laser resonance ionization of evaporated gadolinium atoms using a Gd-Ho multi-filament. The ATD of Gd^+ is rather confined and peaks at about 38.6 ms, unlike for gadolinium oxides of masses ranging between 168 u and 176 u (see the same figure). GdO^+ ions produce broad ATDs due to the different positions along the drift path where oxidizations occur. The GdO^+ ions created near the filament need about 43.6 ms to traverse the drift cell, whereas those created in the nozzle cone exhibit on the one hand the drift time of Gd^+ ions, but on the other hand they are registered at masses of GdO^+ . Hence, in order to investigate the mobility of such molecules, it is necessary to make use exclusively of the UV light of the excimer laser such that no resonance ionization takes place but instead molecules of sample atoms are ionized above the filament according to Eq. (7.2).

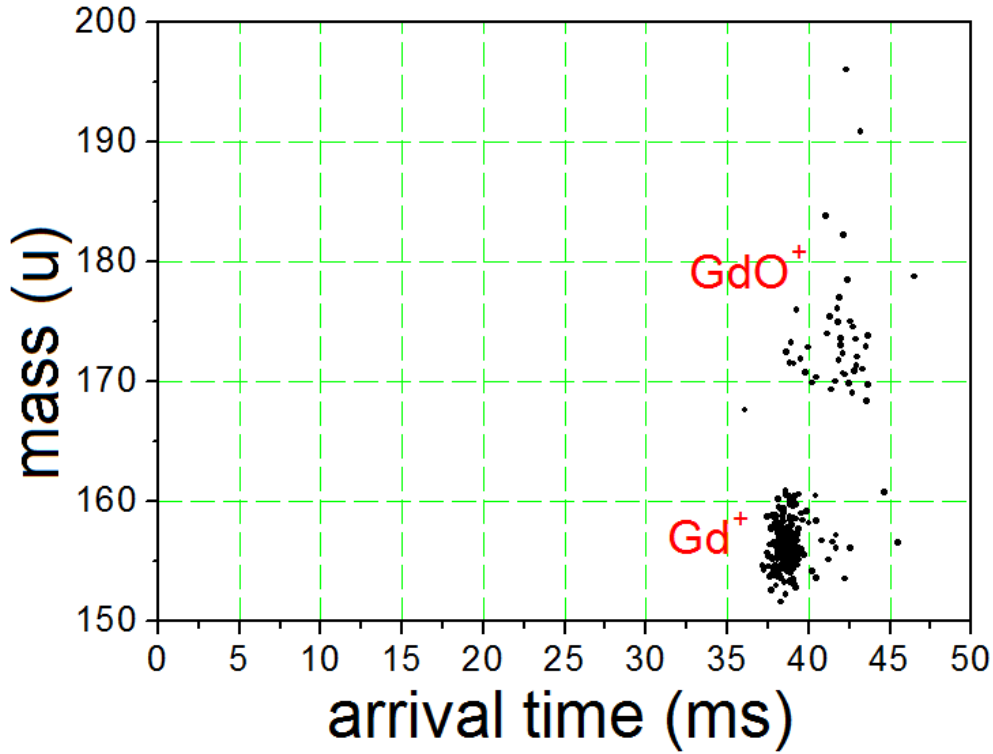


Figure 7.2: Mass-time spectrum obtained after laser resonance ionization of evaporated gadolinium atoms from a Gd-Ho multi-filament at a cell pressure of 40.6 mbar ($E/n = 1.8$ Td). The obtained oxides are created according to Eq. (7.4).

7.1.2 Charge transfer reactions

In case of elevated filament temperatures, the mass-time spectra become somewhat difficult to interpret, especially in the presence of residual impurities. A rather simple case is shown in Fig. 7.3. This scatter plot is obtained by evaporating and ionizing terbium atoms from a Tb-Gd-Ho multi-filament. The relatively large differences in the vapor pressure of the filament constituents, i.e. Tb, Gd and Ho, bear the risk of decreasing the terbium signals even at higher filament temperatures due to charge transfer reactions, in which an essential amount of created Tb^+ ions neutralize in accordance with Eq. (7.3) by transferring their charge mainly to evaporated Ho atoms. Such reactions are called asymmetric charge transfer reactions, since different elements are involved in them². The resulting charge transfer loss [129] is proportional to the number density of the simultaneously evaporated holmium and to the charge transfer

²The symmetric charge transfer reaction ($\text{Tb}^+ + \text{Tb} \rightarrow \text{Tb} + \text{Tb}^+$) does not contribute to ion losses and remains not considered so far. In addition, charge transfer reactions involving sample ions and buffer gas atoms or residual impurities are almost improbable due to the strong endoergicity of such reactions [133].

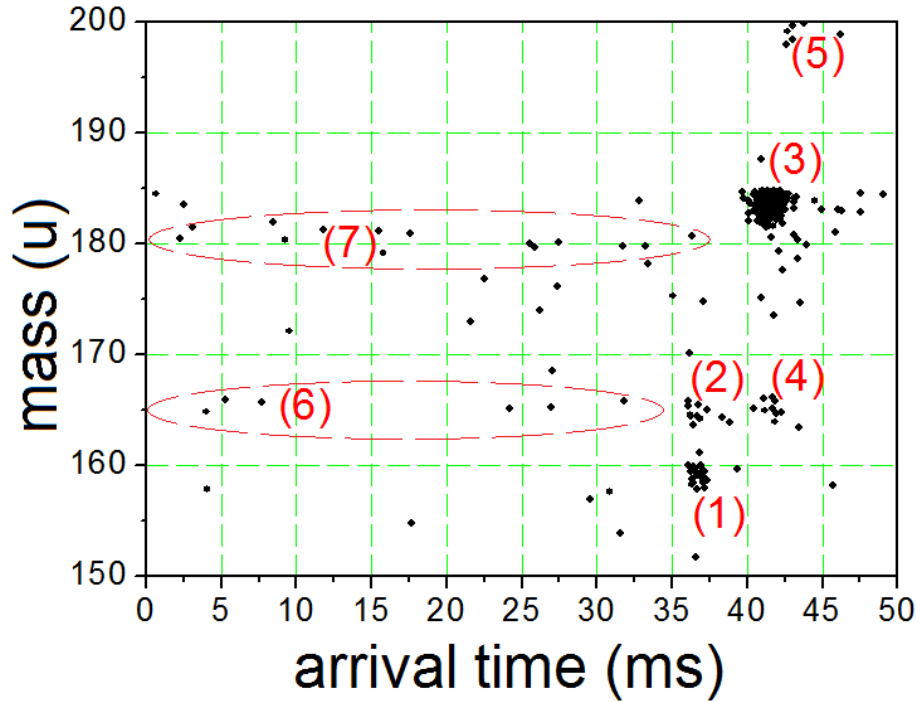


Figure 7.3: Mass-time spectrum of resonantly ionized terbium at an argon pressure of 42.2 mbar and E/n value of 1.7 Td. (1): Resonantly ionized Tb^+ , (2): Ho^+ created in charge transfer reactions, (3): HoH_3O^+ , (4): Ho^+ from molecule cracking of HoH_3O^+ , (5): $\text{HoO}(\text{H}_2\text{O})^+$, (6): thermally ionized Ho^+ , (7): thermally ionized HoO^+ . The filament temperature amounts to $T_{Fil} = 1220(20)$ K.

cross section. The latter has been investigated theoretically [134, 135] as well as experimentally [130, 136, 137] for a variety of elements and is expected to be in the order of 10^{-18} m^2 [129] for asymmetric lanthanide reactions. Therefore, the simultaneous production of Ho^+ with respect to resonantly ionized terbium (see Fig. 7.3) is just a consequence of charge transfer reactions at a filament temperature of 1220 K.

Figure 7.3 is obtained during a mass scan with a scanning period of 10 s/u, such that the ATDs shown there can be associated with a certain constant E/n value. Both Ho^+ (2) as well as Tb^+ (1) arrival time distributions center at about 36.5 ms, which implies nearly equal mobilities and hence almost the same collision integral $\Omega^{(1,1)}$ for these two elements. A detailed discussion on the obtained mobilities is provided in the next chapter.

Actually, Ho^+ signals are also expected in the previous three figures 6.15, 7.1 and 7.2, where gadolinium is resonantly ionized and detected. In those experiments, however, the used Gd-Ho multi-filament has been manipulated such that at $T_{Fil} = 1220$ K the vapor pressure of Ho is drastically reduced. A simple method to do so is to prevent the filament current from flowing through the holmium strip. The latter then gets

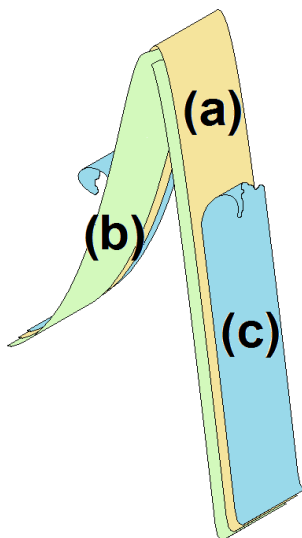


Figure 7.4: Primed multi-filaments, which allow for controlling the vapor pressure of the filament constituents. (a): Intact foil strip used for evaporating the sample atoms. (b): The foil is cut in the middle and gets heated indirectly via thermal conductivity by the intact filament. (c): Damaged strip, which similarly to (b), is heated by the intact filament.

indirectly heated by the Gd filament via thermal conductivity (see Fig. 7.4). On the one hand this method allows for sufficient holmium atoms to be evaporated during Ho mobility measurements and on the other hand it ensures gadolinium mobility measurements without significant charge transfer reactions according to $\text{Gd}^+ + \text{Ho} \rightarrow \text{Gd} + \text{Ho}^+$. A similar problem may arise while working with an Yb-Eu-Ho multi-filament. In such a case, the holmium signal may get considerably suppressed by charge transfer reactions inside Yb and Eu vapors. The big advantage now is that holmium requires elevated temperatures beyond the melting point of Yb and Eu in order to be efficiently evaporated, so that at $T_{Fil} > T_m(\text{Yb}, \text{Eu})$, the strips of the latter elements get immediately damaged like shown in Fig. 7.4 (c). The holmium strip, however, remains intact and can then be exploited for evaporation of the sample elements.

7.2 Molecule cracking

The mass-time spectrum shown in Fig. 7.3 as well as the terbium mass spectrum in Fig. 6.3 underline the hypothesis of chemical reactions ending up with the production of HoH_3O^+ , $\text{HoO}(\text{H}_2\text{O})^+$ and TbH_3O^+ molecular ions in accordance with the observations made in Ref. [50] and [113] for the elements erbium and gadolinium. Noteworthy in Fig. 7.3 are the HoH_3O^+ (3) signals at 184 u, which exhibit a mean ATD of 41.5 ms. Such molecules may be cracked within the emerging buffer gas jet inside the extraction chamber and thereby producing Ho^+ ions (4) of a mean ATD equal to that of the

larger hydroxides. The time difference between the two Ho^+ distributions in Fig. 7.3 amounts to about 5 ms, which facilitates the assignment of their signals.

Extensive tests with different lanthanides have shown the dissociation of oxides to be unfavored compared with the case of hydroxide molecules (compare with Fig. 7.2). However, molecule cracking phenomena may deliver misleading results concerning the arrival time distributions. Therefore, it is advisable first to get rid of the residual impurities inside the cell before beginning the mobility measurements. This procedure promises highest extraction efficiencies and significantly eases the ATD analysis.

7.3 Thermionic emission of the filament

Efficient evaporation of the filament constituents reduces the measurement time and enhances the precision of the mobility measurements in consequence of pressure and temperature variations with time. The easiest way to achieve this goal is to increase the filament temperature, which possibly causes unwanted charge transfer reactions as mentioned before. Additionally, higher filament temperatures facilitate surface ionization [138, 139], which is usually very well described by the so-called Saha-Langmuir equation [140, 141]

$$\frac{n_+}{n_0} = (g_+/g_0) \exp[(e\varphi - IP)/k_B T], \quad (7.5)$$

where n_+ , n_0 are the flux of ions and atoms, respectively, g_+ and g_0 are the statistical weights of the ionic and atomic states, $e\varphi$ is the work function as discussed in Ref. [142], IP is the first ionization potential of the atom (in eV) and T is the equilibrium temperature of the system, which may be set equal to the filament temperature T_{Fil} . Since the work functions of the lanthanide atoms [143] are smaller than their corresponding ionization potentials [144], the thermionic emission saturates at extremely high temperatures according to Eq. (7.5). Thermionic emission decreases the amount of neutral atoms within the ionization volume and leads to higher background in the ATDs, as can be inferred from Fig. 7.3 (6) and (7). For instance, the first ionization potential of holmium is 6.02 eV [62, 144] and the work function of a hexagonal closed packed Ho-crystal may be taken equal to 4.37 eV [143]. The expected Ho^+ flux is about $1.5 \cdot 10^{-7}\%$ of the overall flux of evaporated Ho atoms at $T_{Fil} = 1220$ K assuming $(g_+/g_0) = 1$. The calculated ratio may appear negligibly small, during the mobility measurements of Gd or Tb, however, it may create a perturbing background in the time spectra due to the low vapor pressure of the latter elements compared with the one of holmium.

One should note that thermionic emission is not correlated with the laser pulsing, such that sample ions produced by surface ionization phenomena are randomly registered during each measurement cycle. During the systematic mobility measurements, thermionic emission has been efficiently suppressed by manipulating suitable filament strips as described in Sect. 7.1.2.

8 Ion mobility measurements in the lanthanide region

In this chapter, the outcome of the experiments and the method used in this work to extract the ion mobility data for certain lanthanide elements is presented. The experimental results are then discussed on the basis of the mobilities calculated according to the rigid-sphere model, the polarization-limit model and the model involving the ion-atom interaction potentials presented in chapter 2. Special emphasis will be placed on the influence of the electronic configuration of valence electrons on the mobility data.

8.1 Experimental results

Different multi-filaments have been used during the mobility experiments. Depending on the evaporation characteristics of the investigated lanthanides, the following element combinations have proven to be very well suited: (I) Ho in conjunction with Er, (II) Ho with Gd and Tb, (III) Ho together with Eu, Yb and Er and (IV) Ho with Gd. Dysprosium could not be investigated in the presence of Gd and has been omitted from the following mobility measurements.

All the results presented here are carried out using a laser beam of 1-3 mm diameter, depending on the vapor pressure of the constituents under consideration. The latter depends on the filament temperature, which has been varied in the range between 950 °C and 980 °C for filaments containing gadolinium or terbium and between 800 °C and 860 °C otherwise. The position of the ionization volume could not be reproduced exactly for the different multi-filaments such that only ATDs of the same multi-filament measured in one run may be directly compared to each other. Figure 8.1 shows the arrival time distributions of Gd^+ , Tb^+ and Ho^+ measured using a Gd-Tb-Ho multi-filament. The time elapsed between the sequentially performed measurements is about 3 minutes, which is just sufficient to adjust the proper excitation wavelength provided by the dye laser. All elements are ionized via the two-step photoionization processes described in Sect. 3.2 using laser beams of different diameters (1-3 mm). Obviously, Gd^+ ions need ca. 3 ms more time to get extracted from the drift cell compared with Ho^+ and Tb^+ , which are detected almost at the same time. According to Fig. 8.1, gadolinium definitely exhibits a larger collision integral $\Omega^{(1,1)}$ than holmium and terbium. Furthermore, it can be clearly discriminated in time from the other two elements using the IMS apparatus presented in this work.

As mentioned before, lanthanide molecules are much larger in size than their monoatomic ions. This means that their discrimination in time would not be a big challenge. Figure 8.2, for instance, shows the time spectra of Er^+ and Ho^+ and their corresponding oxide ions obtained while working with an Er-Ho multi-filament. Unlike the atoms, which are ionized via the element selective two-step photoionization process, the oxides are non-resonantly ionized using exclusively the UV light of the excimer laser. In this case the beam diameter amounts to 10 mm. This method is less efficient compared with the two-step photoionization process such that less events are registered in the oxide spectra. In case of low statistics, fit routines may fail to mimic the time spectra resulting in larger uncertainties of the ATD means. In general, increasing the measurement time would result in smaller uncertainties, but due to the pressure effects described in Sect. 6.3.2, broadened peaks will result for extended measurement periods. Nevertheless, in certain time spectra like the one shown in Fig. 8.2, good fits of the line shapes could be obtained using Gaussian fit functions. The time differences between the monoatomic ions and their oxides are about 5.6 ms and 6.2 ms for Er and Ho, respectively. This plot demonstrates the ability of the ion mobility

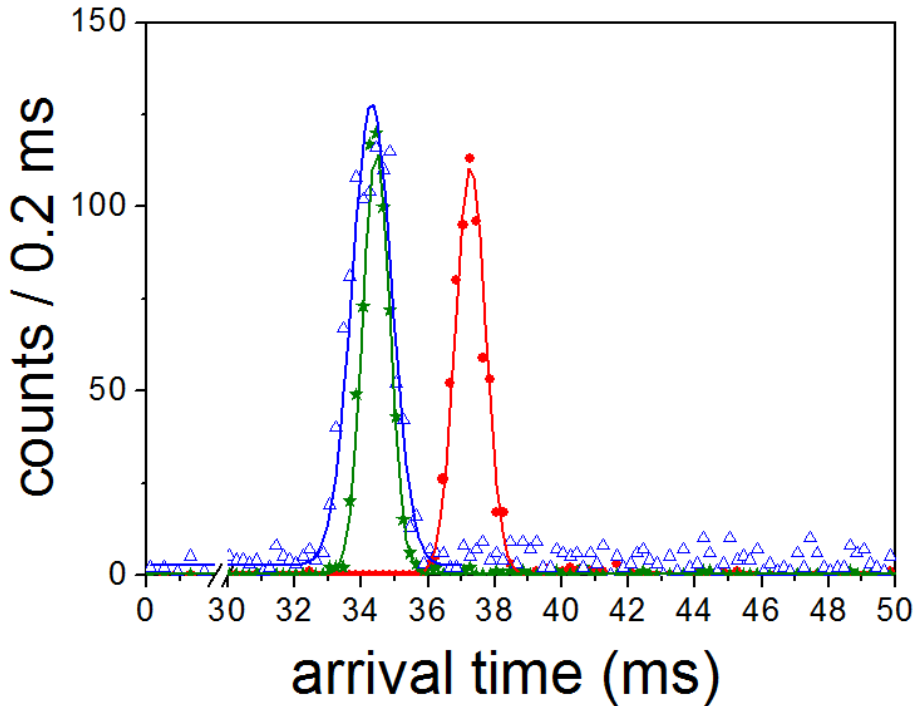


Figure 8.1: ATDs of Gd^+ (\bullet), Tb^+ (\star) and Ho^+ (∇) measured using a Gd-Tb-Ho multi-filament at an argon pressure of 40.4 mbar ($E/n = 1.8$ Td) and a filament temperature of $T_{Fil} = 1220(20)$ K. The measurement time amounts to 300 s, 200 s and 40 s for Gd^+ , Tb^+ and Ho^+ , respectively, whereas all these spectra are measured within 15 minutes. The solid lines are Gaussian fits of the obtained spectra, which deliver the following ATD means: $\langle t_a(\text{Gd}^+) \rangle = (37.269 \pm 0.012)$ ms, $\langle t_a(\text{Tb}^+) \rangle = (34.444 \pm 0.009)$ ms and $\langle t_a(\text{Ho}^+) \rangle = (34.310 \pm 0.019)$ ms.

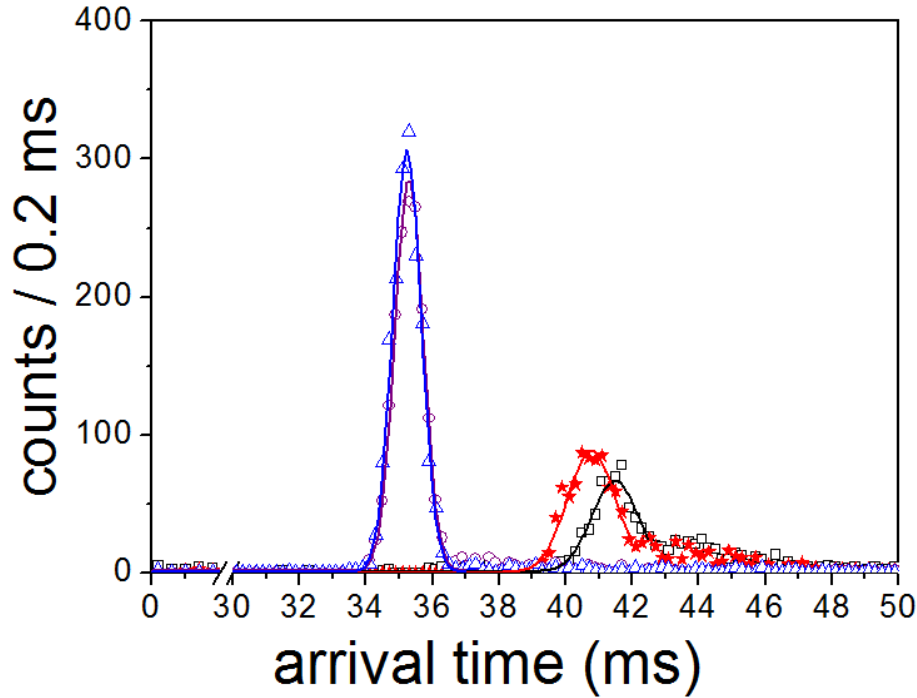


Figure 8.2: ATDs of Ho^+ (\circ), Er^+ (Δ), HoO^+ (\square) and ErO^+ (\star) measured using an Er-Ho multi-filament at an argon pressure of 40.6 mbar ($E/n = 1.8$ Td). In contrast to monoatomic ions, the oxides are ionized using exclusively the UV light of the excimer laser. The solid lines are Gaussian fits of the obtained spectra, which deliver the following ATD means: $\langle t_a(\text{Ho}^+) \rangle = (35.291 \pm 0.014)$ ms, $\langle t_a(\text{Er}^+) \rangle = (35.229 \pm 0.010)$ ms, $\langle t_a(\text{HoO}^+) \rangle = (41.488 \pm 0.027)$ ms and $\langle t_a(\text{ErO}^+) \rangle = (40.782 \pm 0.017)$ ms.

spectrometer to distinguish between the singly charged oxides of both elements, which actually implies the well-known bond length contraction [17] of lanthanides. The time difference between the two oxide peaks is about 706 μs , which is quite significant and cannot be explained only by systematic errors, in particular because the measurements are performed in a sequential manner within 30 minutes at a constant buffer gas pressure. The tailing on the right hand side of the oxide peaks is probably caused by large and slow molecular ions that dissociate to give oxide ions within the supersonic gas jet inside the extraction chamber. The time difference between the holmium peaks in Fig. 8.1 and Fig. 8.2 is a consequence of modified experimental conditions, especially variations of the buffer gas pressure and of the position of the ionization volume with respect to the filament and to the electrode system of the drift cell.

According to Eq. 3.1, the mean drift time $\langle t_d \rangle$ is obtained by subtracting the mean transit time $\langle t_t \rangle = (182 \pm 12)$ μs (see Sect. 6.4) from the arrival time mean $\langle t_a \rangle$. Due to the fact that the drift time is a linear function of the pressure as well as of the drift distance, one may normalize all means $\langle t_a(\text{X}^+) \rangle$ of singly charged ions X^+ to a

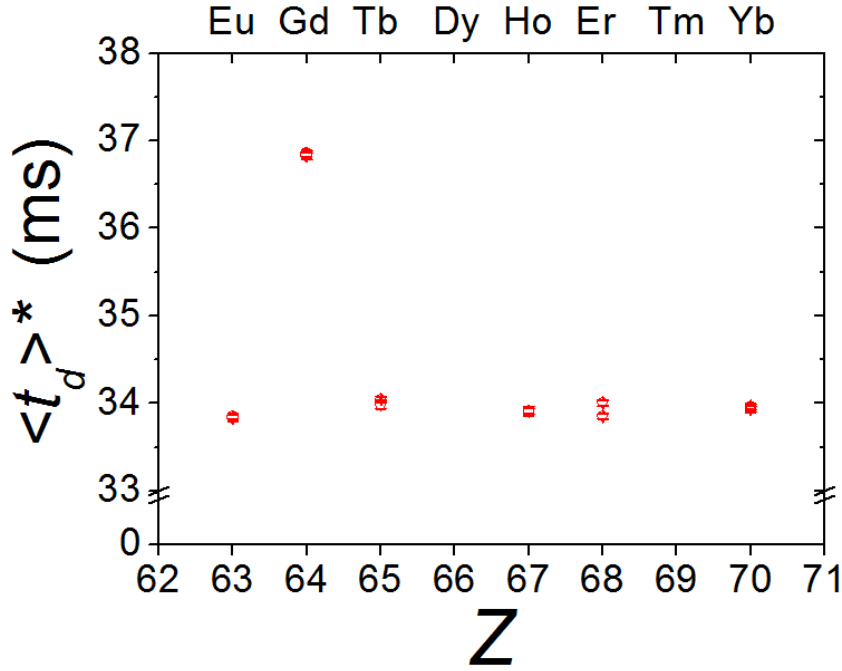


Figure 8.3: Normalized drift time means $\langle t_d \rangle^*$ of some singly charged lanthanides. All the means presented here correspond to an argon pressure of $(P_{cell}^{ref} = 40.97 \pm 0.15)$ mbar ($E/n = 1.8$ Td), to a gas temperature of 300 K and to a starting position of $(y, z) = (5 \text{ mm}, 5 \text{ mm})$ as shown in Fig. 6.10, which results in a drift distance of $d_d^{ref} = (316 \pm 1)$ mm.

reference mean drift time of Ho^+ according to

$$\langle t_d(X^+) \rangle^* = \frac{\langle t_d(\text{Ho}_{ref}^+) \rangle}{\langle t_d(\text{Ho}^+) \rangle} \cdot \langle t_d(X^+) \rangle, \quad (8.1)$$

where $\langle t_d(\text{Ho}_{ref}^+) \rangle$ is the mean drift time of a reference time spectrum of holmium measured at a certain buffer gas pressure P_{cell}^{ref} and a certain drift distance d_d^{ref} . The value $\langle t_d(X^+) \rangle$ and $\langle t_d(\text{Ho}^+) \rangle$ is the mean drift time of the considered ion species and of a corresponding holmium ion measured in one run under the same conditions, respectively. The normalized mean drift time of the sample ion is denoted by $\langle t_d(X^+) \rangle^*$.

The result of such a normalization is shown in Fig. 8.3 and Fig. 8.4. The error bars shown in these figures result from the error propagation due to the normalization given by Eq. (8.1) and denote one sigma uncertainties of the $\langle t_d \rangle^*$ values. The overlapping data markers in Fig. 8.3 imply the reproducibility of the mean values after normalization. The reproducibility of the results is within 0.3% even though slightly different conditions prevailed during the measurement runs. The mismatch of the data at erbium (Fig. 8.3) could not be explained yet. The drift of the ions in the vicinity of the filament may introduce systematic errors due to e.g. field inhomogeneities prevailing there. Furthermore, the ion mobility depends also on the gas temperature T [2, 145, 146], such that variations of T near the filament may contribute to systematic errors, too. In

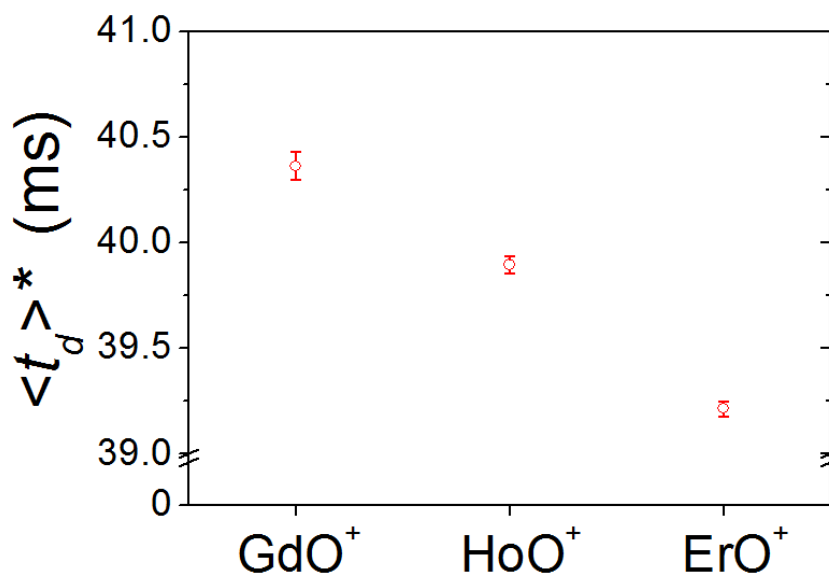


Figure 8.4: Normalized drift time means $\langle t_d \rangle^*$ of some singly charged lanthanide oxides (same conditions as in Fig. 8.3). The means decrease as going to heavier monoxides, which nicely reflects the bond length contraction at the lanthanides [17].

this work, the gas is assumed to be in a thermal equilibrium because a drastic increase of the gas temperature is expected only within the ionization volume and has been neglected so far. Also a dense vapor of the sample atoms may influence the mobility of the ions above the filament in a sense that ions do not drift in a pure buffer gas as required. Such an influence have not been considered in this work due to the fact that the ionization volume is located axially ≈ 5 mm away from the tip of the filament, where the density of the vapor of sample atoms is drastically reduced, see Fig. 6.10 (a). If such systematic errors strongly influence the time spectra, then they are expected to produce similar variations in the normalized means, which is definitely not the case as can be seen in Fig. 8.3.

Noteworthy in this figure is that most investigated lanthanide ions show nearly equal drift time means. The only exception is Gd⁺ with significantly larger $\langle t_d \rangle^*$ values, which actually indicate an increased collision cross section of the latter ion with respect to the other element ions. Also within the oxides, GdO⁺ exhibits a larger drift time mean compared with that of TbO⁺ and ErO⁺ as shown in Fig. 8.4, resulting in a continuous decrease of $\langle t_d \rangle^*$ as going to heavier monoxides. A detailed discussion of the experimental results is provided in Sect. 8.3.

Table 8.1 summarizes the drift time t_d^{exp} of the investigated ion species, which is just an arithmetic mean of the corresponding $\langle t_d \rangle^*$ values shown in Fig. 8.3 and Fig. 8.4. The errors indicated in this table are classified into systematic (*sys*) and statistical (*stat*) errors, in order to emphasize the precision of the measurements. In the statistical errors, both the propagation of the errors due to Eq. (8.1) as well as the deviation of the arithmetic means are considered. The systematic errors concern the accuracy of the

Table 8.1: Drift time of the investigated ions at an argon pressure of ($P_{cell}^{ref} = 40.97 \pm 0.15$) mbar ($E/n = 1.8$ Td, $E = 17.9$ V, $d_d^{ref} = (316 \pm 1)$ mm).

ion	$^{151}\text{Eu}^+$	$^{156}\text{Gd}^+$
t_d^{exp} [ms]	$33.84 (\pm 0.03)_{stat} (\pm 0.13)_{sys}$	$36.83 (\pm 0.03)_{stat} (\pm 0.15)_{sys}$
ion	$^{159}\text{Tb}^+$	$^{165}\text{Ho}^+$
t_d^{exp} [ms]	$34.02 (\pm 0.04)_{stat} (\pm 0.13)_{sys}$	$33.91 (\pm 0.02)_{stat} (\pm 0.13)_{sys}$
ion	$^{168}\text{Er}^+$	$^{174}\text{Yb}^+$
t_d^{exp} [ms]	$33.93 (\pm 0.08)_{stat} (\pm 0.13)_{sys}$	$33.95 (\pm 0.03)_{stat} (\pm 0.13)_{sys}$
ion	$\text{GdO}^+ (m = 172 \text{ u})$	$\text{HoO}^+ (m = 181 \text{ u})$
t_d^{exp} [ms]	$40.36 (\pm 0.07)_{stat} (\pm 0.16)_{sys}$	$39.90 (\pm 0.04)_{stat} (\pm 0.16)_{sys}$
ion	$\text{ErO}^+ (m = 184 \text{ u})$	
t_d^{exp} [ms]	$39.22 (\pm 0.04)_{stat} (\pm 0.16)_{sys}$	

results and are mainly determined by the uncertainty of the pressure values measured by the capacitance gauge. The variation in the operating temperature of the gauge is 1 °C at most, such that the relative error of the pressure is equal to 0.37% [147] at 41 mbar argon. Moreover, the drift of the buffer gas pressure with time (see the left plot of Fig. 6.7) results in time differences between the ATD peaks of the sample ions within a single run lasting for about 10 min. Such tiny pressure variations remained unresolved during the experimental runs. They cause additional systematic errors in the order of 0.03% (see Sect. 6.3.2).

8.2 Extraction of the ion mobilities

According to Eq. (2.3), the mobility K may be calculated from the drift time t_d^{exp} obtained during the experiments and from the drift path S and the electric field $E(s)$, which is position dependent. The latter is quite constant near the symmetry axis of the drift cell for most drift electrodes. The only exception is beneath the focusing electrodes, where relatively higher electric fields are needed to focus the ions into the nozzle cone. The ions spend nearly 20% of the drift time inside the inhomogeneous part of the field near the nozzle¹ such that any approximation of the electric field by the mean value $\langle E(s) \rangle$ inevitably results in a large mobility inaccuracy. A better mobility estimate may be obtained by an exact calculation of the integral $\int_S ds/E(s)$

¹Compare the curve of the E/n parameter shown in Fig. 3.4 for Po^+ ions drifting in 40 mbar argon.

provided that the geometry of the apparatus as well as the boundary conditions of the measurements are very well known. The way followed in this work is to simulate the ion drift from an initial distribution above the filament until arriving to the nozzle throat by using the SIMION 8.0 [148] software, which makes use of the finite difference method to solve the Laplace equations for a given geometry of electrodes. In conjunction with a user-written program, the so-called Lua program, SIMION allows also for ion drift simulations (see Appendix D).

There is a variety of physical models that may be incorporated in the Lua codes such that mobility, diffusion, space charge effects, etc. are taken into account when calculating the ion trajectories. The way the models work is that at each simulation time step, such a user program applies an adjustment to the ion motion according to some equation or algorithm depending on the desired collision model [65, 149, 150, 151, 152]. In the presented work, only a macroscopic approach, which uses viscous damping (Stokes' law) to describe the average effect of the buffer gas on the ions has been considered. This approach does not calculate the deflection angle for ion-atom collisions (as usually considered in complicated collision models) and therefore does not accurately represent diffusional effects [153] and ceases to be useful when ion energies become very large compared to thermal energies [67]. However, Lock and Dyer [66] reported that such an approach is most applicable to cases where the ions have large cross sections or a high collision frequency. Since the focus of the simulations performed here is on the mobilities of heavy ions drifting in about 41 mbar argon at low E/n values, the viscous damping model is assumed to be trustworthy. Further details on the used model can be found in Appendix D.1.

For the performed simulations, the geometry of the drift cell including the electrode system has been implemented into the SIMION workbench. The potential array calculated by the program corresponds to the potentials listed in Tab. 3.2. The Lua code presented in Appendix D.2 accepts input parameters like the pressure P , the temperature T and the reduced mobility K_0 in order to calculate the mobility K (according to Eq. (2.4)), from which then the viscous deceleration $a_v = -e \cdot v/m \cdot K$ according to Eq. (D.1) and Eq. (D.2) is obtained. The parameters e and m are input parameters for the ion charge and mass, respectively. The instantaneous acceleration a_s and velocity v of the ions, however, are numerically calculated by the SIMION code itself and are subsequently corrected by the viscous damping term according to Eq. (D.7) for each time step. This correction procedure allows to mimic the average effect of diffusion (but not realistic diffusion due to ion-atom collisions) in cases where relatively large ions drift in a dense buffer gas. This is the case assumed in this work. Otherwise, diffusion processes have to be considered by implementing sophisticated Lua codes in the simulation runs, since different ion trajectories may result when compared with the viscous damping model.

In the performed simulations, the temperature T has been fixed to 300 K, whereas the gas pressure P amounts to 40.97 mbar. These parameters correspond to the temperature and the pressure of the buffer gas during the experiment in which the arrival time spectrum of the reference ion $^{165}\text{Ho}_{ref}^+$ has been measured. In

Table 8.2: Mobilities of the investigated ions at an argon pressure of 40.97 mbar ($E/n = 1.8$ Td).

ion	$^{151}\text{Eu}^+$	$^{156}\text{Gd}^+$
K_0 [cm ² /Vs]	$1.844 (\pm 0.002)_{stat} (\pm 0.019)_{sys}$	$1.692 (\pm 0.001)_{stat} (\pm 0.018)_{sys}$
ion	$^{159}\text{Tb}^+$	$^{165}\text{Ho}^+$
K_0 [cm ² /Vs]	$1.834 (\pm 0.002)_{stat} (\pm 0.019)_{sys}$	$1.839 (\pm 0.001)_{stat} (\pm 0.019)_{sys}$
ion	$^{168}\text{Er}^+$	$^{174}\text{Yb}^+$
K_0 [cm ² /Vs]	$1.839 (\pm 0.004)_{stat} (\pm 0.019)_{sys}$	$1.837 (\pm 0.001)_{stat} (\pm 0.019)_{sys}$
ion	$\text{GdO}^+ (m = 172 \text{ u})$	$\text{HoO}^+ (m = 181 \text{ u})$
K_0 [cm ² /Vs]	$1.546 (\pm 0.003)_{stat} (\pm 0.016)_{sys}$	$1.563 (\pm 0.002)_{stat} (\pm 0.016)_{sys}$
ion	$\text{ErO}^+ (m = 184 \text{ u})$	
K_0 [cm ² /Vs]	$1.590 (\pm 0.001)_{stat} (\pm 0.017)_{sys}$	

SIMION, the ions of a single species have an initial 3D Gaussian distribution with $\text{FWHM}_{x,y,z} = 0.5$ mm. Their origins are Monte-Carlo distributed with a center located at $(x, y, z) = (0 \text{ mm}, 5 \text{ mm}, 5 \text{ mm})$ above the filament (compare Fig. 6.10), which results in a drift distance of $d_d = d_d^{ref} = 316$ mm. The used code enforces the ions to drift in a sequential manner and does not allow for the simulation of possible space charge effects. For a proper evaluation of the drift time simulations, data of more than 100 ions per each ion species are required. The most important output parameter of SIMION is the drift time. For enough ions, the drift time distribution is a Gaussian-like peak with a mean t_d^{sim} of a negligible deviation and a width (in terms of the standard deviation) $\sigma \approx 5 \mu\text{s}$. The input parameter K_0 of a certain ion species is varied as long as needed until the calculated t_d^{sim} value comes close to the corresponding t_d^{exp} value listed in Tab. 8.1. As a general rule for the assignment of the mobilities, the relative difference between the calculated and the measured drift time of an ion species has to be less than 0.05%. The reduced mobilities obtained from such iteration procedures are listed in Tab. 8.2. A detailed discussion of the mobilities is provided in the next section.

The mobility uncertainty has several distinct origins. In addition to the errors mentioned in Sect. 8.1, the uncertainty in the drift distance d_d^{ref} during the measurements results in a 0.6% underestimation/overestimation of the reduced mobilities at most. This relative error has been obtained by varying the center of the initial ion distribution in SIMION by ± 1 mm along the symmetry axis and analyzing the impact of such variations on the calculated drift time means t_d^{sim} . Furthermore, the relative error caused by the difference between the calculated and the measured drift time contributes with about 0.05% to the systematic errors.

Since the mobility is calculated using a software package, one may still introduce systematic errors due to numerical inaccuracies or inaccuracies of the used physical models. The used SIMION 8.0 software is deemed to be sufficiently reliable due to its widespread application areas and especially due to its excellent reputation in the field of mass spectrometry [151]. However, due to the mesh size of the grid chosen in the simulations (1 mm x 1 mm x 1 mm), the drift electrodes as well as the filament including the foil strips could not be drawn exactly in the SIMION workbench. After refining the grid, the resulting drift field may slightly differ from that prevailed during the measurements (especially near the electrodes), which may cause additional systematic errors.

An other origin of such errors may be the averaging effects caused by the viscous damping model when considering diffusion phenomena. Unfortunately, there is no simulated data in the accessible literature that could be compared with experimental data, especially for realistic IMS instruments and for monoatomic and heavy ions drifting in elevated argon pressures. The performance of the damping model, however, has been compared with other models simulating ion-molecule collisions based on the kinetic theory of gases [66, 153, 154]. The damping model produces very narrow time distributions for ions starting at the same position due to the averaging effect described in Appendix D.1. Other models successfully simulate the ion diffusion by considering each ion-atom collision, which results in broadened peaks [66, 155]. Nevertheless, the peak positions determined by the different models almost coincide, which makes the viscous damping model somewhat realistic at least concerning the “low-field” mobilities. Systematic errors like the underestimation of the drift path by the latter model will consequently result in the underestimation of the mobilities and vice versa. In fact, viscous damping is produced by the the long-range induced-dipole interaction, by which an ion feels the effect of many gas atoms at once rather than the short-range force of a direct collision [67]. Therefore, the damping model is best suited to describe the mobility of huge particles, like aerosols etc., of sizes comparable to the mean free paths. Concerning the drift of monoatomic ions where multiple collisions become less probable [2], the validity of this model remains questionable. This, however, does not effect the expressiveness of the experimental results at all, especially when comparing the obtained mobilities with each other. When trusting the viscous damping model implemented in SIMION and neglecting the effects of the grid onto the calculated electric fields (which is the case for the results presented in this work (Tab. 8.2)), the overall accuracy of the obtained mobilities can be given by a relative error of less than 1.3%.

8.3 Discussion of the mobility data

In the following, the obtained mobilities for the different lanthanide and lanthanide monoxide ions will be discussed in detail.

8.3.1 Lanthanide mobilities

The investigated lanthanide ions have in common a xenon core electronic configuration and occupied 6s-orbitals. The series corresponds to a gradual filling of the 4f-orbitals (except for Gd⁺ for which a 5d electron is added) and undergo a smooth decrease in radius with increasing atomic number known as the “lanthanide contraction” [17, 131], a direct result of the poor ability of electrons in the f-subshell to shield outer electrons from the increasing nuclear charge.

The mobility data of the investigated lanthanide ions at 300 K are summarized in Tab. 8.2 and shown in Fig. 8.5. Obviously, most obtained mobilities (open circles in the figure) are remarkably similar except for Gd⁺. The mobility of the latter is found to be $K_0 = [1.692 (\pm 0.001)_{stat} (\pm 0.018)_{sys}] \text{ cm}^2/\text{Vs}$, which is about 8% lower than for the other lanthanide ions. The explanation of such a deviation is an increased collision cross section of the singly charged gadolinium that may be influenced by the specific valence electron configuration of this element. Unlike the other investigated ions, Gd⁺ exhibits an occupation of the 5d-subshell [16]. Hence, the mobilities shown in Fig. 8.5 are associated with the ground states $[\text{Xe}]4f^75d6s$ for Gd⁺ ($Z=64$) and $[\text{Xe}]4f^i6s$ for the other ions, where $i = Z - 56$. Excited states of the singly charged ions are excluded in the measurements performed at “low-field” conditions due to the resonance ionization techniques exploited in this work. Also ATDs that could be associated with excited states of singly charged ions have not been observed in the measurements carried out during this work.

The rigid-sphere model

Assuming the applicability of the rigid-sphere model as described in Sect. 2.2.1, one may expect the ion-neutral forces to show a variety of distinctive features, each of which affects the mobility in a characteristic manner as the ionic radii of the heavy ions decrease. This postulates also that the repulsion term becomes the only dominant part in the interaction potential at closer ion-atom distances (see Sect. 2.2.2). From this point of view, the trends predicted by the $\sqrt{\langle r^2 \rangle}$ or by the $\langle r_{out} \rangle$ values [16] as shown in Fig. 1.1 have to be comprehensible by means of mobility measurements.

Taking the ionic and the atomic radii to be equal to either $\sqrt{\langle r^2 \rangle}$ or $\langle r_{out} \rangle$, one may calculate the reduced mobilities of the investigated species according to Eq. (2.4) and Eq. (2.5) in conjunction with Eq. (2.10) from the internuclear distance determined by the sum of the radii of the sample ions r_{ion} and the argon atoms r_{Ar} . For a mean spherical radius of argon of 0.77 Å [21], the calculated mobilities of the lanthanides are about 21 times larger than those obtained from the experiments when considering their corresponding $\sqrt{\langle r^2 \rangle}$ values from Fig. 1.1. About 2 times larger mobilities are obtained when instead of the mean spherical the outermost radii $\langle r_{out} \rangle$ are considered, whereas one may take $\langle r_{out} \rangle = 1.76 \text{ Å}$ [21, 157] for an argon atom. This inconsistency clearly indicates the simplicity of the rigid-sphere model and that “low-field” mobilities are neither sensitive to the mean spherical nor to the outermost radii of singly charged

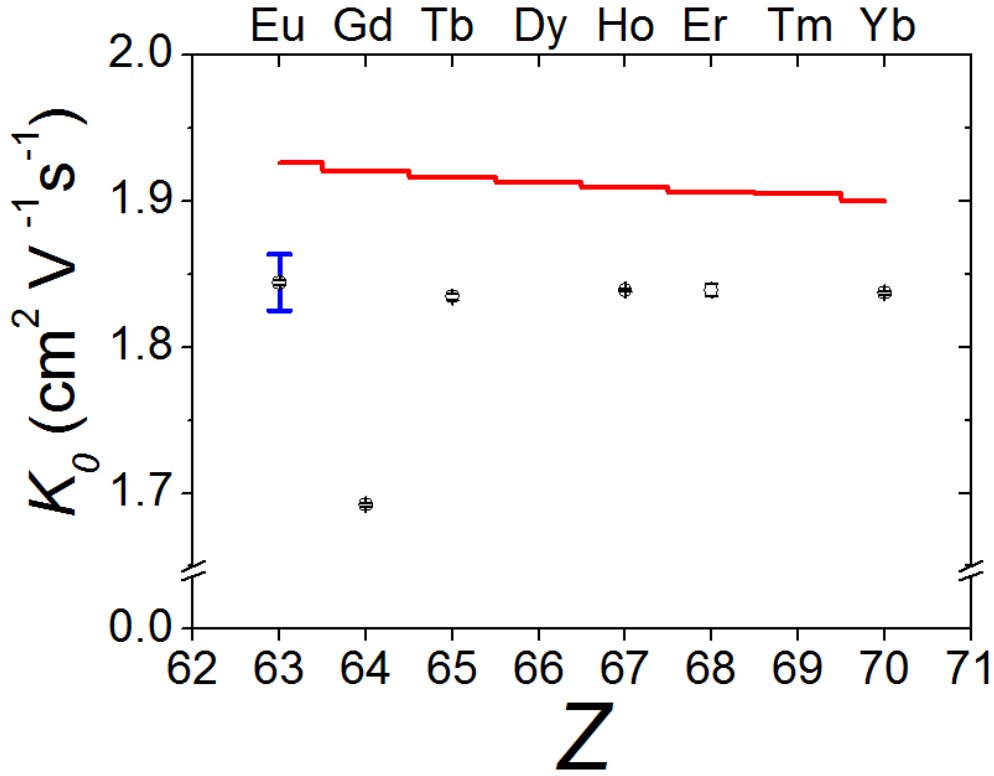


Figure 8.5: (—○—): Measured reduced mobility (K_0) of some investigated lanthanide ions at an argon gas temperature of 300 K (error bars with open circles, this work). The large error bar at ^{63}Eu indicates the common systematic error. Statistical errors are presented by smaller error bars on each data marker. (—): Mobility calculated according to the polarization limit model for $T \rightarrow 0$ (Eq. (2.14)) using an argon polarizability of $\alpha_p(\text{Ar}) = 1.641 \text{ \AA}^3$ [156].

lanthanides, but get strongly influenced by the electronic configuration as demonstrated in former publications [8].

The polarization limit model

Unless the gas atoms possess an appreciable permanent dipole or quadrupole moment, the longest-ranged component of the ion-atom interaction potential is the charge-induced dipole potential, which arises from the interaction of the ionic charge with the dipole that it induces in the neutral quantity [2]. At low temperatures, the mobility of heavy ions is dominated by this polarization attraction, which is given by the potential

$$V_{pol}(r) = -\frac{1}{2} \cdot \frac{e^2 \alpha_p(\text{Ar})}{(4\pi\epsilon_0)^2 r^4}, \quad (8.2)$$

with an argon polarizability of $\alpha_p(\text{Ar}) = 1.641 \text{ \AA}^3$ [156].

According to the polarization limit model (Eq. (2.14)), the mobility should exclusively be a function of the reduced mass $\mu = mM/(m+M)$ and approaches a constant nonzero polarization limit, K_{pol} , for vanishing temperatures $T \rightarrow 0$. For heavy ions with masses much larger than the mass of argon, the mobility turns out to be essentially independent of the ion mass and quite constant for the different investigated lanthanides. This scenario is presented by the solid line in Fig. 8.5. This is in contrast with the physical intuition as well as with experimental observations (see the same figure), but is in accordance with what one would expect when repulsive forces are completely neglected.

According to McDaniel and co-workers ([1], p. 147-148), reduced mobilities at room temperature are close to K_{pol} values in general. Hence, the polarization limit model provides a simple tool to make a first guess of the “low-field” mobilities of a variety of ion-neutral systems, if the polarizability of the neutral quantity is known. According to the same reference, smaller mobilities than the polarization limit (as the case in Fig. 8.5) indicate that the (n,4) potential (Eq. (2.16)) is not sufficient to describe the interaction potential and that the dispersion attraction has to be considered in terms of a non-vanishing parameter γ in Eq. (2.15).

The ion-atom interaction potential

Better mathematical models that mimic the interaction potential of singly charged lanthanides with neutral argon may be obtained by considering both the short-range repulsive and the long-range attractive forces as suggested by Eq. (2.12) and Eq. (2.16). Recent ab initio studies [158, 159] of heavy element systems have shown great strides towards an accurate prediction of such interaction potentials. The performed relativistic ab initio calculations also consider the attractive dispersion contribution [42], which corresponds to the intermediate-range interaction potential, i.e. the $-C_6/r^6$ term in Eq. (2.12). Figure 8.6, for instance, shows the interaction potential of an $\text{Yb}^+(^2\text{S})$ - $\text{Ar}(^1\text{S})$ system at 300 K obtained from such ab initio calculations [160]. The depth of the potential well located at an internuclear distance of $r_m \approx 3.25 \text{ \AA}$ is about -0.1 eV . During head-on collisions, ions coming from larger radii r hit the repulsive wall and separate from each other with the same energy and opposite momentum. They do not fall into the potential minimum because there is no way to release their kinetic energy. If no electronic excitation occurs, the kinetic energy remains the same unless a third particle comes and hits the collision pair, thereby removing extra energy. However, the formation of diatomic ions is not probable especially at high kinetic energies of the collision partners at 300 K. The steepening of the potential wall on the left-hand side of r_m is mainly defined by the short-range repulsion, in which the electronic configuration of the sample ions obviously plays a significant role via the Pauli exclusion principle. According to Viehland [161], the “low-field” mobilities presented in this work are expected to be less sensitive to short-range repulsion. At low E/n values like in the performed experiments, the mobility is constant for a single ion species because the field-derived energy expressed as the $(\frac{1}{2}Mv_d^2)$ term in Eq. (2.6) is negligibly small compared to the thermal energy, such that the collision integral $\Omega^{(1,1)}$ in Eq. (2.7) re-

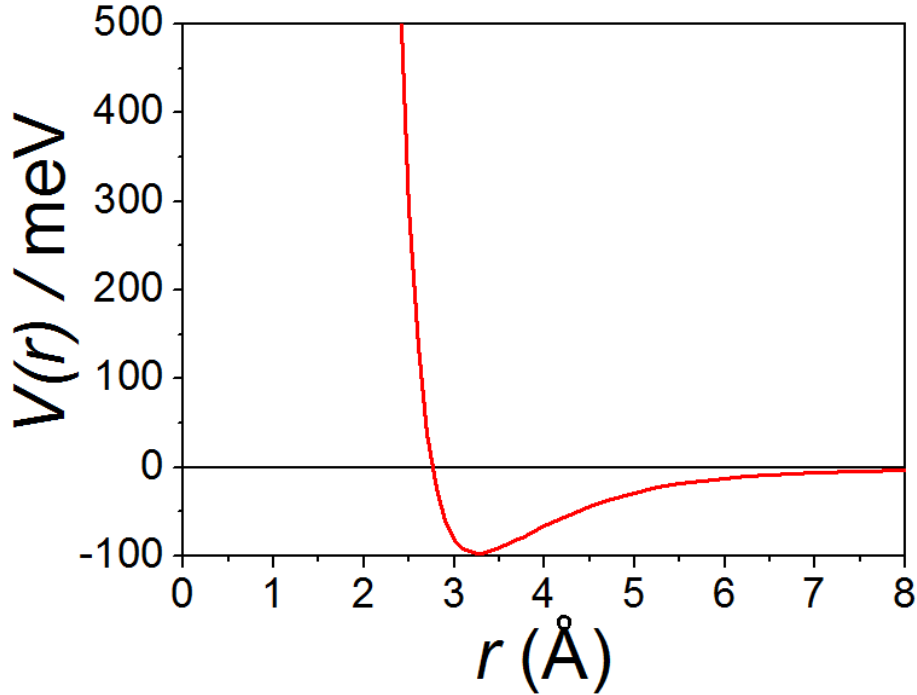


Figure 8.6: Interaction potential of Yb^+ ions with argon at 300 K according to Ref. [160] vs. the internuclear distance r .

mains unchanged. Strong repulsion is not expected until the internuclear distance of the colliding pair is considerably less than the critical radius² r_c for orbiting collisions given by [122]

$$r_c = \left[\frac{e^2 \alpha_p(\text{Ar})}{(4\pi\epsilon_0) \mu \bar{v}^2} \right]^{1/4} \approx 4.6 \text{ \AA}, \quad (8.3)$$

with the relative collision velocity \bar{v} . At that point, however, the orbiting collision has already occurred, because the centrifugal potential prevents seeing the repulsive part of the interaction potential at low kinetic energies for a wide range of impact parameters, see Fig. 2.1. Due to the sensitivity of the diffusion cross section $Q^{(1)}$ (Eq. (2.8)) to the deflection angle θ , which may exhibit values corresponding to unstable circular orbits ($\theta = -\infty$), the contribution of orbiting collisions to the momentum transfer collision integral (Eq. (2.7)) is such significant that “low-field” mobilities of lanthanide-argon systems are deemed to probe the long-range rather than the short-range part of the interaction potential. This, actually, explains the mobilities near the polarization limit as shown in Fig. 8.5.

Figure 8.7 shows the calculated reduced mobility of $^{174}\text{Yb}^+$ in argon vs. the E/n parameter. The mobility curve is calculated by Mr. L. Viehland [161, 162] using the

²This equation requires a small relative collision energy ε and a polarization attraction, which dominates the interaction potential. It can be derived from Eq. (8.2) by setting V_{pol} equal to the kinetic energy $\frac{1}{2}\mu\bar{v}^2$.

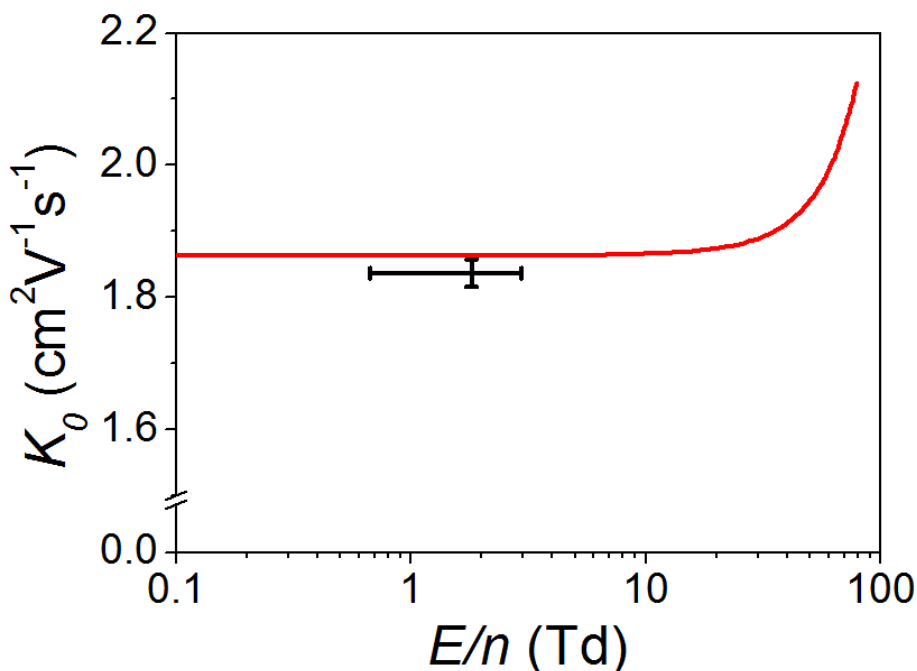


Figure 8.7: Mobility of Yb^+ in argon at 300 K vs. the E/n parameter according to Ref. [161]. The mobility curve is calculated using the $\text{Yb}^+ - \text{Ar}$ interaction potential shown before. The cross presents the reduced mobility of Yb^+ obtained in this work. The horizontal error bar indicates the uncertainty of the E/n parameter, at which the measurement has been performed.

$\text{Yb}^+ - \text{Ar}$ interaction potential shown in Fig. 8.6, whereas the gas temperature is taken equal to 300 K. The accuracy for the calculated mobility amounts to $\Delta K_0/K_0 = 0.1\%$. Three successive integrations are needed to obtain the mobility from a given interaction potential. The first integration determines the deflection angle θ in the ion-neutral collision as a function of the impact parameter b and relative energy ε (see Eq. (2.9)). The second integration averages over impact parameters to yield the transport cross sections $Q^{(1)}$ as a function of energy according to Eq. (2.8). The third integration averages the cross sections over energy to produce the collision integrals $\Omega^{(1,1)}$ as a function of temperature (Eq. 2.7). Subsequently, the mobility is calculated according to Eq. (2.4) and Eq. (2.5)³. Difficulties may arise during the first two integrations due to singularities and other irregularities that can occur in their integrands [1].

As E/n increase, the collisions become more energetic and they probe successively further into the region where the internuclear distance is small, i.e. the effective potential V_{eff} is probed in a region below its inflection point (see Fig. 2.1). Then the mobility exhibits a maximum, which is expected to be at large values of E/n , larger than the ones displayed in Fig. 8.7. For a better understanding compare the mobility curve of thallium ions [158] shown in Fig. E.1. Thereafter, increasing E/n probes further and

³The effective temperature T_{eff} may be considered equal to the gas temperature for $E/n < 12$ Td.

further into the repulsive region of the interaction potential, making the mobility decrease as $1/\sqrt{k_B T_{eff}}$ as predicted by the rigid-sphere model. In Fig. 8.7, the mobility maximum has not been reached even not at $E/n = 78.78$ Td, which denounces the rigid-sphere model to be less realistic at this point. In the “low-field” region, the rigid-sphere model is not reasonable, except in the sense that one can always adjust the size of the sphere to match data over a small range of T and E/n . The physical meaning of such a sphere, however, remains questionable. The cross in Fig. 8.7 presents the reduced mobility of Yb^+ obtained in this work, which is remarkably close to the theoretically predicted values⁴. More mobility data at different E/n values would provide a good tool to test the kinetic theory of heavy ions in gases and give the opportunity to draw more conclusions on the interaction potential. However, the inverse problem of determining the potential from the mobility data is rather difficult and an unambiguous inversion in the general case is impossible in principle [40].

From the interaction potential of Fig. 8.6, one may deduce the best value for the parameter n in Eq. (2.12), Eq. (2.15) and Eq. (2.16) to be $n = 8$. Assuming the (8,6,4) potential to give a realistic figure of the Yb-Ar interaction potential, the best fit of the parameters in Eq. (2.15) can be determined as $\varepsilon_0 = 99$ meV, $r_m = 3.2$ Å and $\gamma = 0.56$. The large parameter γ implies a significant contribution of the r^{-6} term to the interaction potential. Since the mobilities obtained are quite similar (except for Gd^+), their interaction potentials are expected to be comparable, even though large changes in the number of f -electrons occur across the lanthanide elements. The minor effect of the f -electrons on the colliding pair underlines the dominance of the charge-induced dipole potential mentioned before.

Nevertheless, the distinct mobility of gadolinium compared with the other lanthanides cannot be explained by the polarization attraction, the $1/r^4$ -term, which is ion-independent. The polarization attraction depends solely on the charge of the ion and on the static polarizability of argon (see Eq. (2.13)). The occupation of the $5d$ orbital (like in Gd) influence both the repulsive as well as the intermediate-range part of the interaction potential. The latter contribution is traced back mainly to the dispersion potential $V_{dis} \approx -C^{(6)}/r^6$ [1, 163] of polarisable heavy ions, whereas the coefficient $C^{(6)}$ depends on the polarizability of the sample ion $\alpha_p(ion)$ of a given electronic configuration. Hence, the dispersion potential may be understood as a backlash of argon atoms on the ion itself. Since both contributions are ion dependent, different electronic configurations may drastically change the whole potential landscape [122], such that distinct ion mobilities result. Besides the effect of the short-range repulsion, the dispersion attraction is seen to have the effect of increasing the steepness of the repulsion wall and thus decreasing the “low-field” mobility, especially of heavy ions drifting in light gases [2, 158], too. The resulting mobility of Gd^+ with the $4f^7 5d 6s$ electronic state will thus likely be smaller than the mobility of lanthanide ions exhibiting the $4f^i 6s^2$ states due to the commonly stronger influence of the d -orbital on the radial electron density and on the polarizability of the ions [122, 164, 165, 166]. Therefore,

⁴The mobility error indicated in Fig. 8.7 results when trusting on the ion trajectories calculated using the viscous damping model, see Sect. 8.2.

neglecting the inverse sixth power term like in Eq. (2.16) would not accurately describe the physics of ion collisions at “low-field” conditions.

Due to the lack of *ab initio* calculations of lanthanide-argon interaction potentials and since no extended mobility data exist for lanthanide elements, no further conclusions can be made so far. Also extrapolations will not help on deducing the inverse sixth power term in Eq. (2.12) with an acceptable accuracy for the gadolinium-argon system. The quantum-mechanical treatment of the latter system, however, may become difficult due to the open-shell structure of Gd^+ and remains a subject of further theoretical investigations [160].

Concluding remark

In the past, it has been shown that state-selective mobility investigations become feasible also using IMS devices [7, 8]. Hence, the mobility spectrometry gains increasingly importance if dealing with heavier elements, where relativistic effects strongly affect their valence electron configurations [16]. The aim of this thesis was to systematically investigate for the first time the “low-field” mobilities of rare-earth metals, where the electronic configuration is expected to be influenced by such relativistic effects. Most of the obtained mobilities have shown a great similarity except for the element gadolinium, which exhibited an 8% lower mobility. The gadolinium peak in the arrival time distributions could be clearly resolved from the other investigated lanthanides at a resolving power of about 45 of the developed apparatus.

The observed mobility deviation is assumed to be a direct consequence of occupying the *d*-orbital in Gd^+ , which in turn has a big impact on the ion-atom interaction potential. However, a direct influence of the ionic radii on the mobilities can be definitely excluded due to the fact that “low-field” mobilities are sensitive also to the attraction potentials, i.e. the polarization attraction and the dispersion attraction, etc., rather than solely to the short-range repulsion.

8.3.2 Mobility of oxides

The lanthanide contraction could be experimentally observed by investigating the mobilities of monoxide ions of Gd, Ho and Er. The obtained mobilities are listed in Tab. 8.2. It is interesting to note that the reduced mobility is higher for ErO^+ ($\approx 1.7\%$) than for HoO^+ , while monoatomic Er^+ and Ho^+ exhibit similar mobilities. The effect almost always seems to be a contraction in the bond length of the lanthanide molecules. Theoretical calculations suggest that about 10% of the lanthanide contraction would come from relativistic effects, which roughly scale as Z^2 [17]. This means a sequential increase in mobilities of the rare earth metals as the charge number increases. Therefore the heavier ErO^+ is expected to be faster than HoO^+ , and the latter faster than GdO^+ , which is confirmed in Tab. 8.1 and Tab. 8.2.

The “low-field” mobilities seem to be sensitive enough to variations in the bond lengths across the lanthanide oxides. An appropriate interaction potential that may be most applicable is the one given by the repulsion and the polarization attraction according to Eq. (2.16). Usually an effective core diameter a^* is imbedded in this equation [4], which accounts for the charge and mass center differences that could be significant in polyatomic ions and neutrals resulting in a parameter $\left(\frac{r_m - a^*}{r - a^*}\right)$ instead of $\left(\frac{r_m}{r}\right)$. It should be mentioned that this work focuses solely on the mobility of monoatomic ions. Chemical reactions of the lanthanide ions with gas impurities have been suppressed in order to achieve highest extraction efficiencies, which actually comply with the ordinary working conditions of buffer gas cells [29, 73]. Therefore, no further mobilities have been measured for these systems.

9 Outlook

The application of IMS techniques to lanthanides may pave the road for investigations of the actinides and even of the superheavy elements. The diversity of the electronic configurations for these elements [16, 167] leads to the expectation of a corresponding distinct mobility, which - in combination with mass analysis - may be exploited for element identification purposes. Hence, the next focus of the mobility measurements will be on certain available actinides, which show such variations in their electronic configurations. Pu^+ ($5f^56d7s$), for instance, exhibits an occupation of the $6d$ -orbital [16] unlike Am^+ ($5f^77s$) or Cm^+ ($5f^77s^2$) and may exhibit a smaller mobility compared with the other two elements as partly assumed in Ref. [14]. With the relatively high resolving power of the developed apparatus (see Sect. 6.3.1), one may definitively approve this assumption.

Using electrochemical deposition techniques [114] for the production of sample filaments, off-line mobility experiments remain accessible for elements up to fermium ($Z = 100$). Also spectroscopic data are available for all these elements (see Tab. A.1 in Appendix A.2), which allow for the application of laser resonance ionization techniques [48, 168] for ionizing sample atoms and thus for an unambiguous assignment of the arrival time distributions. This ambitious goal, however, requires significant improvements of the IMS apparatus and further off-line investigations at the accessible actinides. Obviously, the most critical parameter in such experiments is the overall efficiency. This may be significantly improved by using larger extraction nozzles in order to achieve highest possible gas flow rates. The next important parameter is the resolving power, which may be kept high when using efficient turbomolecular pumps for evacuating the detection part of the apparatus. Furthermore, laser resonance ionization may become more efficient by installing an optical resonator around the ionization volume such that enough laser photons are provided to ionize the neutral atoms. The evaporation from filaments may not be applicable at certain elements of high evaporation temperatures, where convection is expected to drastically decrease the ionization efficiency. It is therefore advisable to alternatively test laser ablation methods [169] from suitable catcher/filament materials under buffer gas environments, before investigating such elements.

Adding different reactants into the buffer gas may enforce chemical reactions and allow for investigations of the reaction rate coefficients, which are of particular interest in chemistry [4]. The rate coefficients may be inferred not only from studying the reactant and product ion intensities with increasing vapor concentration of a sample, but also from the shape of the arrival time distributions [1] as described in Sect. 6.3.

Ion chemical reaction studies involving lanthanides [48] and actinides [113] have proven to be easily achievable with IMS techniques in on-line as well as in off-line experiments. Such studies provided information on the electronic structure for a variety of elements [170] and promise an interesting approach to the physics and chemistry investigations of the heaviest elements in the years to come.

In contrast to chemistry methods, which require the existence and production of element isotopes with half-lives of more than a second [171, 172, 173], methods involving IMS techniques are quite fast. The ion drift time can be tuned to be even in the ms-regime such that elements exhibiting only short-lived isotopes are still accessible via ion mobility spectrometry. IMS investigations at superheavy elements may be performed in on-line experiments, e.g. at the UNILAC accelerator facility of GSI in Darmstadt behind the recoil separators TASCAs [174] and SHIP [64]. The latter allows for the suppression of background from scattered primary beam particles and transfer products to $< 100/s$, which is the maximum ion rate that can be handled by the developed mobility spectrometer, limited by the width of the ATDs. When investigating elements, for which no information on laser excitation schemes exists, thermalized fusion products that still exhibit a positive charge may be directly extracted from the cell by applying the extraction methods introduced in Sect. 3.3.1 or by using an ion funnel trap [175] as an ion injection mechanism. The latter technique yielded sufficient precision of the injection time as well as of the starting position of ions stopped inside a buffer gas cell [176, 177]. The ion funnel trap can be easily coupled to the drift cell, such that the mobility spectrometer becomes still compact in size and thus flexible for online experiments.

All in all the application of IMS techniques to lanthanide elements has opened the door towards electron configuration and relativistic contraction studies of the heaviest elements. The kinetic theory of gases has reached a stage where mobility data over wide ranges of temperatures and electric field strengths serve as stringent tests of ion-neutral interaction potentials over wide ranges of separation. Hence, the time is ripe for using such techniques with actinide and transactinide ions.

Appendix

A Laser resonance ionization methods

A.1 The two-step photoionization process

The excitation of sample atoms and their ionization using two laser beams of different wavelengths can be approximated by the simple rate equations for the number density N_1 in the ground state 1, the number density N_2 in an intermediate excited state 2, and the ion number density N_i [178]:

$$\frac{dN_1}{dt} = -P_{12}(N_1 - N_2) + \frac{1}{\tau_{12}}N_2; \quad \text{with } N_1(t=0) = N_0, \quad (\text{A.1})$$

$$\frac{dN_2}{dt} = P_{12}(N_1 - N_2) - P_i N_2 - \frac{1}{\tau_{12}}N_2; \quad \text{with } N_2(t=0) = 0, \quad (\text{A.2})$$

$$\frac{dN_i}{dt} = P_i N_2. \quad (\text{A.3})$$

The quantities P_{12} and P_i represent the transition rates from the ground state into the excited state and from the excited state into the continuum, respectively. The relaxation time of the excited atoms is given by τ_{12} . In the equations above, the statistical weights of the ground and excited states have been assumed to be equal and the decay of the excited level only takes place to the ground state.

With two lasers of short pulses $\Delta t \ll \tau_{12}$ that temporally and spatially overlap, the ratio of the created ions compared to the ground state atoms can be expressed as:

$$\frac{N_i}{N_0} = 1 - \frac{a_1 + a_2}{2a_2} \exp[-(a_1 - a_2)\Delta t] + \frac{a_1 - a_2}{2a_2} \exp[-(a_1 + a_2)\Delta t], \quad (\text{A.4})$$

where a_1 and a_2 are given by the equations

$$a_1 = P_{12} \left[1 + \frac{P_i}{2P_{12}} \right] \quad \text{and} \quad a_2 = P_{12} \sqrt{1 + \left(\frac{P_i}{2P_{12}} \right)^2}. \quad (\text{A.5})$$

The transition rates are directly proportional to the transition cross sections σ_{12} , σ_i and to the energy flux of the laser beams Φ_{12} , Φ_i (photons/cm²) according to [63]

$$P_{12} \cdot \Delta t = \sigma_{12} \cdot \Phi_{12} \quad \text{and} \quad P_i \cdot \Delta t = \sigma_i \cdot \Phi_i. \quad (\text{A.6})$$

Direct photoionization of excited atoms to the continuum has a very small cross section, usually of the order of 10^{-18} cm², which limits the ratio N_i/N_0 and hence the two-step

ionization efficiency to $< 1\%$ [46]. Increased efficiencies can be obtained if the second step occurs resonantly into the so-called auto-ionization states [178]. Alternatively, an enhancement of element selectivity and ionization efficiency can be achieved if in the second step high-lying Rydberg states [33, 179] are populated, which lead to ionization of the sample atom through buffer gas collisions.

A.2 Suitable excitation states of some actinide elements

Table A.1: Overview of some actinide atomic levels that decay into the ground state by emitting photons in the green, blue and UV range of the electromagnetic spectrum. The quantity λ_{12} and $\bar{\nu}_{12}$ is the wavelength in air and the excitation energy given as a wavenumber, respectively. The first row of each group gives the ground state values of the corresponding element. Values taken from Ref. [62]. Also references of some former spectroscopic investigations are indicated in the table.

Element	λ_{12} [Å]	Configuration	Term	J	$\bar{\nu}_{12}$ [cm ⁻¹]
Pu I		$5f^67s^2$	7F	0	0
	4896			1	20426 [113]
	4206.481	$5f^57s7p$	$^7D^\circ$	1	23766.139
	3851.007	$5f^56d^27s$		1	25959.849
	3753.628	$5f^67s7p$		1	26633.288
Am I		$5f^77s^2$	$^8S^\circ$	7/2	0
	5000.21			7/2	19992.16 [113]
	4681.65				21352.99 [105]
	4662.79	$5f^77s7p$	(7/2, 2)	7/2	21440.37 [50, 105, 180])
Cm I		$5f^76d7s^2$	$^9D^\circ$	2	0
	4330.82	$5f^76d7s7p$	9D	3	23083.822
	3995.10	$5f^76d7s7p$	7D	3	25023.578
	3116.41	$5f^76d7s7p$	5P	2	32078.886
Cf I		$5f^{10}7s^2$	5I	8	0
	4329.03	$5f^{10}7s7p$	(8, 2) $^\circ$	9	23093.355
	3785.61				26408.305 [51]
	3598.77	$5f^{10}7s7p$	(8, 1) $^\circ$	9	27779.345
Fm I					0
	3982.98				25099.80 [51]
	3981.08				25111.80 [51]

B The developed IMS software

Different LabVIEW-based programs have been developed to allow for a variety of experiments and investigations before and during mobility measurements. In this section, the software user interface and some modes of operation are explained.

B.1 The control software of the iseg high voltage modules

The used iseg HV modules for supplying the drift electrodes with the suitable potentials have already been described in Sect. 4.3. Based on the CAN-bus communication protocols and on a driver module provided by the manufacturer [181], a huge package of commands can be used to control the functionality of each high voltage channel. Among the 32 available channels, only 24 are in use: 22 channels are reserved for the drift electrodes, one for the extraction nozzle¹ and one for the filament.

The user interface of the LabVIEW-based program for setting the appropriate potentials inside the cell is shown in Fig. B.1. Thereby the control panel allows not only for individual setting of the voltages (1), but also for monitoring the actual voltages (2) of all channels. The electrode potentials are either read out from a user defined ASCII file or given manually (5) for each channel (4). If all voltages are successfully applied, the “Ready” indicator (3) changes its color into green, otherwise it stays red.

Before terminating the program (7), the software provides the possibility of saving the currently used potential configuration as an array of floats in an ASCII file (6) of individual name. As mentioned in Sect. C, the risk of gas discharges exists between the electric feedthroughs and the wall of the cell. However, during the startup phase of the high voltage regulation procedure, the critical value for voltage breakdown may be exceeded between the electrodes if not a certain hierarchy is maintained. This scenario is hindered by the software such that

1. the voltage of each electrode is increased in 30 V steps up to the selected optimum potential and
2. the voltage increment takes place in a cyclic order for the different electrodes starting at the nozzle until arriving at the last electrode of the entrance window.

¹Alternatively FUG HV modules described in Sect. 4.3 may be used instead.

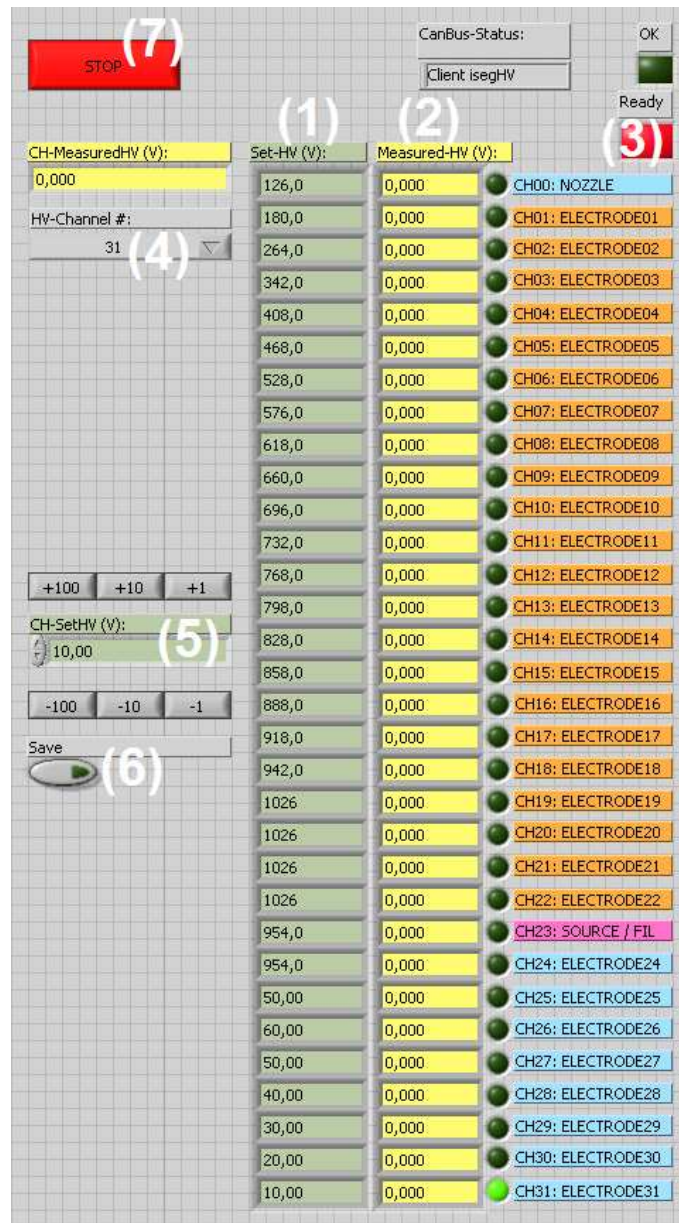


Figure B.1: User interface of the LabVIEW based program for setting the filament potential and the 22 drift potentials inside the cell.

An inverse but similar procedure is followed while shutting down the high voltages. Usually, if gas discharges occur, the involved channels cannot be controlled by the developed software and wrong voltage values are shown on the panel. In this case, the user has to reset the potentials and the CAN-bus communication port by restarting the program. In this way, a permanent control of the voltages is intended to exclude the possibility of unnoticed gas discharges during mobility measurements.

B.2 The control software of the DAQ system

For mobility measurements, a LabVIEW-based data acquisition software has been developed that allows for an efficient readout of the remote PXI 7833R DAQ system presented in Sect. 4.3. Its control panel is shown in Fig. B.2. Before starting the program, the user may define an ASCII file, where to store the data (1), and determine which kind of measurements is intended. Different possibilities are available:

1. For finding the suitable laser resonance of a certain element, one may fix the ion mass to one expected value (2), and start (6) a laser scan by detuning the dye laser (3), see Sect. 6.1. In this case, each registered event is associated with a certain position of the laser grating, which later on can be translated into wavenumbers.
2. The user may fix the ion mass for the QMS filter at only one value (2) and start the drift time measurements for a certain time interval (4). The resulting time spectra will be shown in (8).
3. Another possibility is to scan the ion masses registered (2) by manipulating the control voltages of the QMG 311 unit described in Sect. 4.3. The resulting mass spectrum is then plotted in (7).

Both the main trigger and the laser trigger (5) allow the user to define the repetition rate of the excimer laser, the period for resetting the time counter and the delay time of laser pulsing vs. the main period. The cell pressure (9) is read out each 10 s and stored in another file associated with the data file defined before (1). The measurement time is shown in (10) and if elapsed, the program stops automatically. (11) is foreseen for an immediate stop by the user. Hence, the stored file contains three parameters associated with each registered event: the ion mass calculated from the response of the mass filter control unit, the relative position of the laser grating, from which a wavenumber can be calculated and a time stamp corresponding to the arrival time if the latter is smaller than the trigger period. The display unit (12) shows the total number of events registered by the DAQ system. Due to the analog signals from the QMS control unit, each readout cycle has to last $> 5 \mu\text{s}$ to be executed, which reflects the ADC dead time of the PXI 7833R. However, using a pulse generator (BNC, model: PB-4), count rates of only 12 kHz could be detected and stored without any losses. This can be checked by counting the events stored (13) and comparing them with those registered (12). For data acquisition beyond this frequency, some improvements in the program structure are inevitable. Especially, event visualization and data storage loops have a big impact on the dead time of the software.

The same software may be taken for extraction efficiency measurements described in Sect. 5.1.1. In this case, the α decays of ^{215}Po implanted in the bare Si PIN diode are registered and displayed in the pad (7). Signal amplitude spectra similar to the energy spectrum in Fig. 5.2 are then shown instead. By triggering the recoil source potential (Sect. 5.1.3), also time spectra (8) of the registered decay events can be obtained, see e.g. Fig. 5.4. The electric circuitry of the used high voltage switch is shown in Fig. B.3. The rise time as well as the fall time of voltages provided by this module is about $2 \mu\text{s}$.

Trigger & Data Acquisition Software

(11) Stop

(6) Start

Digital-Triggering

Beam Trigger: (DO0)

MainTrigger (DO0)

MainPeriod0 (s) 0,05

MainOnTime0 (s) 0,025

MainTrigger-DelayTime (s) 0

Laser Trigger: (DO5)

LaserTrigger (DO5)

LaserPeriod5 (s) 0,05

Laser-DelayTime (s) 0

LaserOnTime5 (s) 1E-5

InvBeam Trigger: (DO3)

InvMainTrigger (DO3)

Laser:

Laser Scan Single Command

Starting Wavenumber (cm-1): 0 (3)

Laser Scan-Steps: 0

Laser Scan Direction

Current Wavenumber (cm-1): 0

File path for the readout data: E:\Data\0903\0903dummy.txt (1)

Measurement-Time (s): 600 (4)

EventCounter: 0 (12)

Analog In 0

Scan-Cycle (s) per Step: 10 (7)

QMS:

QMS Scan Single Command

Starting Ion Mass (amu): 168,50 (2)

QMS-Steps (amu): 0

QMS Scan Direction

Current Ion Mass (amu): 0,00

Energy Filter:

Energy-Low (V): 0,00000

Energy-High (V): 5,00000

Time Filter

Time-Low (s): 0,00000

Time-High (s): 0,20000

Progress (%): 0 (10)

Cursor0 X-Position (V): 100

Cursor1 X-Position (V): 200

Marked Events: 0 (13)

X-DOWN (V): 0,00000

X-UP (V): 10,00000

Event-Rate (1/s): 0

RS232-Port: COM1

CH#: 1

Pressure (mbar): 4,02E+1 (9)

SaveTimePlot

Time Bins 128 (8)

Figure B.2: User interface of the listmode data acquisition software.

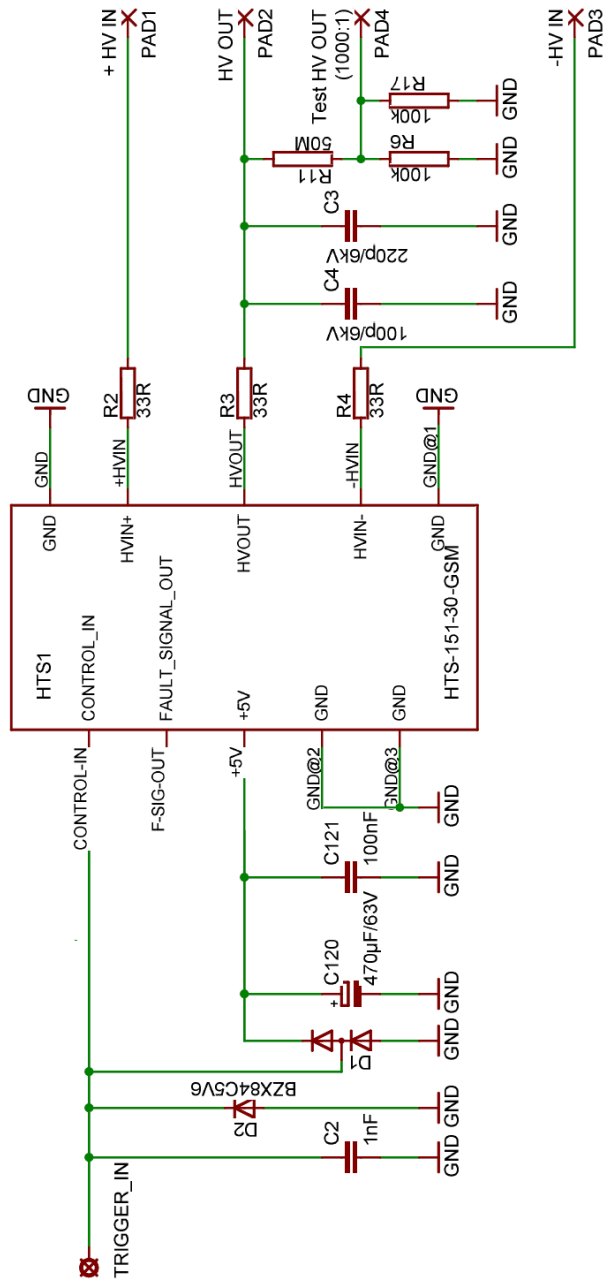


Figure B.3: Electric circuitry of the used fast HV-switch (Behlke, type HTS 151-30-GSM).

C Gas discharge experiments

Gas discharge experiments are carried out in order to define highest possible electric fields between the focusing electrodes inside the drift cell. In Fig. C.1, the measured breakdown voltage HV_B for two plane, electropolished stainless steel electrodes in argon gas is shown. The parameter Pd^* describes the product of the gas pressure P and the gap between the used electrodes d^* . The critical voltage for gas discharges HV_B is determined by fixing the distance d^* , whereas the electric field between them is increased until a current is flowing or visible UV light from gas discharges is registered. The argon pressure is varied in the range at which IMS measurements are expected to be carried out resulting in Pd^* values between 6 and 36 Torr·cm, which are well above the location of the Paschen curve minimum for argon [74, 182]. The latter is found to be at a Pd^* value of about 1.1 Torr·cm [77].

Remarkably in Fig. C.1 is the fact that increasing gas purity results in a decreased critical voltage for breakdown. This amounts to 371 V at 40 mbar argon (12 Torr·cm), which is close to the predicted value in Sect. 3.3.2. At 100 mbar Ar, the critical field is found to be about 1.4 kV/cm.

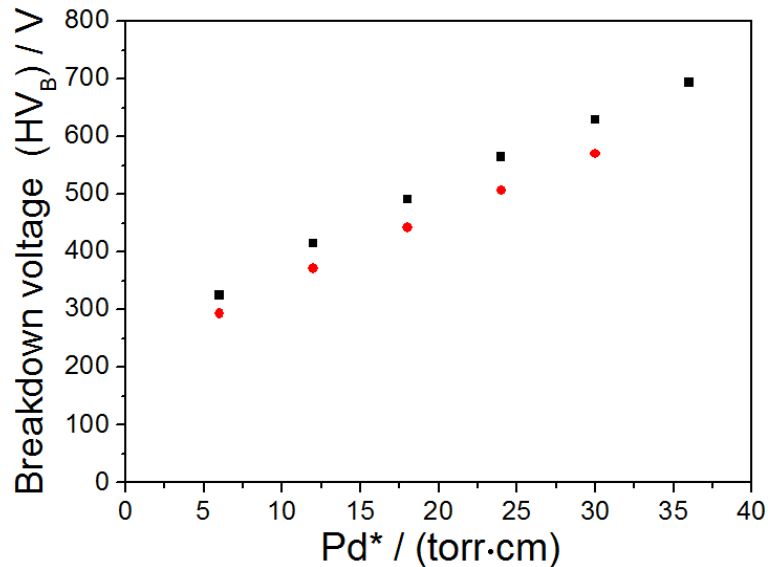


Figure C.1: Measured breakdown voltage HV_B for electropolished stainless steel electrodes in argon (■). The distance d^* between the electrodes is 0.4 cm. The voltage HV_B decreases by $\approx 10\%$ at sufficient gas purity (●), which is achieved by activating the getter pump inside the cell.

D SIMION simulations

SIMION [65] is a native ion optics simulation program that models ion optics problems with 2D symmetrical and/or 3D asymmetrical electrostatic and/or magnetic potential arrays. An overview on the numerical methods used in this program can be found in Ref. [66, 148]. Originally developed for ion optics in vacuum, the program nowadays has an excellent reputation, especially in the field of mass spectrometry. One of the key features of the SIMION code is its ability to run complex user-written programs, thus allowing for predicting the trajectories of ions drifting in a neutral gas even at atmospheric pressure [155]. The so-called high-level language program “Lua” is such a user program.

This chapter describes the viscous damping model implemented in the SIMION simulations and presents parts of the user-written codes used in the different ion-trajectory simulations.

D.1 The viscous damping model used in the drift time simulations

The simplest model used in the SIMION simulations is the viscous damping model, which applies via Stokes’ law [183] damping to the ion motion in a neutral gas. In such a model, the drag force F_v acting on spherical ions due to their drift in a viscous gas is proportional to their velocity v . From this point of view, the acceleration¹ due to the drag force can be expressed as

$$a_v = \frac{1}{m}F_v = -\zeta \cdot v, \quad (\text{D.1})$$

where m is the ion mass and ζ is the semi-empirical constant of proportionality defined by Stokes’ law. It may be related to the mobility of singly charged ions of large cross sections according to (compare Eq. (47) and Eq. (48) in Ref. [43])

$$\zeta = \frac{e}{m \cdot K}, \quad (\text{D.2})$$

with the mobility K .

¹Also referred to as deceleration.

In such a case, SIMION computes the ion's total acceleration a_s at a certain point as appropriate as possible and adds the correction term a_v (see the Lua codes in D.2 and D.3) to give an updated ion acceleration

$$a_s^* = a_s + a_v = a_s - \zeta \cdot v. \quad (\text{D.3})$$

If v is taken as the velocity at the beginning of a simulation time step, one may overestimate/underestimate the viscous damping term due to the possible velocity change within the time step duration δt_s . The viscous damping algorithm becomes significantly improved and the accuracy of the results drastically increases when multiplying the right hand side of Eq. (D.3) by a correction factor f as described below. The main idea behind such a correction factor is to consider the average viscosity acceleration during the time step. For this purpose, one may solve the differential equation

$$\frac{da_v}{dt} = -\zeta \cdot \frac{dv}{dt} = -\zeta \cdot a, \quad (\text{D.4})$$

or equivalently,

$$\frac{da_v}{dt} = -\zeta \cdot (a_s + a_v). \quad (\text{D.5})$$

Assuming a_s to be relatively constant over the time step, one obtains the solution of the above differential equation as

$$a_v(t) = (a_s - \zeta \cdot v(0)) \exp(-\zeta t). \quad (\text{D.6})$$

The average value of a_v over the time step is then

$$\langle a_v \rangle = \frac{1}{\delta t_s} \cdot \int_0^{\delta t_s} a_v(t) dt \quad (\text{D.7})$$

$$= \frac{1}{\delta t_s} \cdot \int_0^{\delta t_s} (a_s - \zeta \cdot v(0)) \exp(-\zeta t) dt \quad (\text{D.8})$$

$$= f \cdot (a_s - \zeta \cdot v(0)), \quad (\text{D.9})$$

where

$$f = \frac{1}{\delta t_s \cdot \zeta} (1 - \exp(-\zeta \delta t_s)), \quad (\text{D.10})$$

which is typically close to 1.

D.2 High-level language program (Lua) for drift time simulations

The entire Lua program using the viscous damping model (drag.lua) is included in the software packages of SIMION 8.0 [148]. Below, only the most important user-defined parts of the program are presented. The damping term in this program is obtained from an assumed mobility K of the ion as explained in Appendix D.1. The mobility K is calculated from the reduced mobility K_0 and from the buffer gas pressure P and temperature T in accordance with Eq. (2.4). K_0 , P and T are adjustable variables that may be manipulated by the user. As an example, the program parts shown below were used to simulate ion trajectories of $^{215}\text{Po}^+$ drifting in 40 mbar argon at 20 °C.

```

- - adjustable variables
- - P_cell in (mbar)
adjustable Buffergas_Press_C_mbar = 40
- - mass of ion Po(215) in (amu)
adjustable amu_mass = 215
- - charge of ion in (e)
adjustable e_charge = 1
- - T_room in (degree Kelvin)
adjustable Buffergas_Temp_C_K = 293
- - Assumed reduced K0 (of 215Po+ in Ar) in (cm^2/Vs)
adjustable Ion_Mobility_cm2_Vs = 1.77
.
.
- - SIMION segment called by SIMION after every time step.
function segment.accel_adjust()
- - calculate ion mobility from local gas pressure
- - 3.7094 = P0/T0 (in order to get K from K0)
K=3.7094*(Buffergas_Temp_C_K*Ion_Mobility_cm2_Vs)/Buffergas_Press_C_mbar
- - calculate damping from effective ion mobility
- - 9.6485333e5 = e/amu * 0.01 cm^2/mm^2. Damping in 1/us
damping = ( 9.6485333e5 * Ion_Charge ) / ( K * Ion_Mass )
- - number of time constants in step
local nt = damping * Ion_Time_Step
- - exponent averaging factor
local factor = ( 1 - exp(-nt) ) / nt
- - adjusting acceleration. velocity in (mm/us) and acceleration in (mm/us^2)
Ion_Ax_mm = ( Ion_Ax_mm - Ion_Vx_mm * damping ) * factor
.
.
end

```

D.3 Lua code used for gas cooling simulations in the first pumping section

Included in the software packages of SIMION is also a Lua program dealing with the ion motion in quadrupolar potentials (quad.lua). This code has been manipulated to fulfill the geometry requirements of the novel IMS apparatus. Besides considering different segments of the RF-quadrupole ion guide, also the viscous damping algorithm presented before has been added in the Lua program in order to simulate the gas cooling mechanism inside the extraction chamber.

The most important parts of the program are shown below:

```
-- adjustable variables
-- gas pressure P1 in (mbar)
adjustable Buffergas_Press_C_mbar1 = 0.05
-- gas pressure P2 in (mbar)
adjustable Buffergas_Press_C_mbar2 = 0.01
-- mass of ion Po(215) in (amu)
adjustable amu_mass = 215
-- charge of ion in (e)
adjustable e_charge = 1
-- T_room in (degree Kelvin)
adjustable Buffergas_Temp_C_K = 293
-- Assumed reduced K0 (of 215Po+ in Ar) in (cm2/Vs)
adjustable Ion_Mobility_cm2_Vs = 1.77
-- begin of the second pumping section (in mm)
adjustable begin_section2_mm = 1.5
-- nozzle voltage in (V)
adjustable nozzle = 126
-- QPIG AC-Amplitude in (V)
adjustable qpig_ac = 60
-- QPIG DC-Amplitude in (V)
adjustable qpig_dc = 0
-- QPIG axis Offset in (V)
adjustable qpig_ax01 = 108
-- QPIG axis Offset in (V)
adjustable qpig_ax02 = 98.0
-- QPIG axis Offset in (V)
adjustable qpig_ax03 = 88.0
-- QPIG axis Offset in (V)
adjustable qpig_ax04 = 78.0
-- QPIG axis Offset in (V)
adjustable qpig_ax05 = 68.0
-- QPIG axis Offset in (V)
```

```

adjustable qpig_ax06 = 58.0
- - QPIG axis Offset in (V)
adjustable qpig_ax07 = 47.6
- - quad entry phase angle of ion in (deg.)
adjustable phase_angle_deg = 0.0
- - RF frequency of QPIG in (Hz)
adjustable frequency_hz = 1.95e6
.
.
- - SIMION segment called by SIMION at the start of ion flight for each potential
- - array instance to initialize adjustable electrode (static) voltages in that instance.
function segment.init_p_values()
Adj_Elect1 = nozzle
Adj_Elect2 = qpig_ax01
Adj_Elect3 = qpig_ax01
Adj_Elect4 = qpig_ax02
Adj_Elect5 = qpig_ax02
Adj_Elect6 = qpig_ax03
Adj_Elect7 = qpig_ax03
Adj_Elect8 = qpig_ax04
Adj_Elect9 = qpig_ax04
Adj_Elect10 = qpig_ax05
Adj_Elect11 = qpig_ax05
Adj_Elect12 = qpig_ax06
Adj_Elect13 = qpig_ax06
Adj_Elect14 = qpig_ax07
Adj_Elect15 = qpig_ax07
end

- - SIMION segment called by SIMION to set adjustable electrode voltages
- - in the current potential array instance.
- - NOTE: this is called frequently, multiple times per time step (by
- - Runge-Kutta), so performance concerns here can be important.
function segment.fast_adjust()
- - Initialize constants if not already initialized.
- - These constants don't change during particle flight.
if not omega then
omega = frequency_hz * (1E-6 * 2 * math.pi)
theta = phase_angle_deg * (math.pi / 180)
end
- Define the potentials.
local sin_period1 = sin(ion_time_of_flight * omega + theta)
local qpig_tempvolts = sin_period1 * qpig_ac + qpig_dc
- Finally, apply adjustable voltages to rod electrodes.

```



```
Adj_Elect2 = qpig_ax01 + qpig_tempvolts
Adj_Elect3 = qpig_ax01 - qpig_tempvolts
Adj_Elect4 = qpig_ax02 + qpig_tempvolts
Adj_Elect5 = qpig_ax02 - qpig_tempvolts
Adj_Elect6 = qpig_ax03 + qpig_tempvolts
Adj_Elect7 = qpig_ax03 - qpig_tempvolts
Adj_Elect8 = qpig_ax04 + qpig_tempvolts
Adj_Elect9 = qpig_ax04 - qpig_tempvolts
Adj_Elect10 = qpig_ax05 + qpig_tempvolts
Adj_Elect11 = qpig_ax05 - qpig_tempvolts
Adj_Elect12 = qpig_ax06 + qpig_tempvolts
Adj_Elect13 = qpig_ax06 - qpig_tempvolts
Adj_Elect14 = qpig_ax07 + qpig_tempvolts
Adj_Elect15 = qpig_ax07 - qpig_tempvolts
end

- - SIMION segment called by SIMION after every time step.
function segment.accel_adjust()
- - calculate ion mobility from local gas pressure
- - 3.7094 = P0/T0 factor in order to get K from K_0
if ion_pz_mm > begin_section2_mm then
K = 3.7094*(Buffergas_Temp_C_K*Ion_Mobility_cm2_Vs)/Buffergas_Press_C_mbar1
elseif ion_pz_mm <= begin_section2_mm then
K = 3.7094*(Buffergas_Temp_C_K*Ion_Mobility_cm2_Vs)/Buffergas_Press_C_mbar2
end
- - calculate damping from effective ion mobility
.
.
end
```

E Mobility of Tl^+ in argon

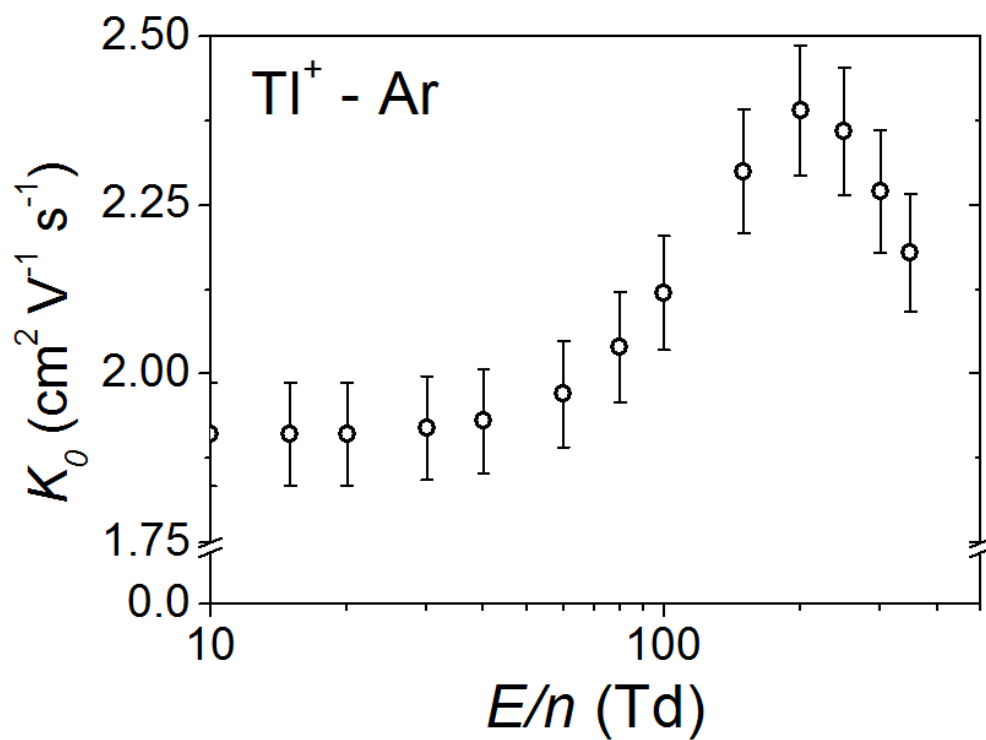


Figure E.1: Mobility of Tl^+ in argon at room temperature. The data are taken from Ref. [35]. The error in the experimental data is believed not to exceed $\pm 4\%$, which is a typically for mobility measurements.

Bibliography

- [1] E. McDaniel, E. Mason, *The Mobility and Diffusion of Ions in Gases*, John Wiley & Sons, New York, 1973.
- [2] E. Mason, E. McDaniel, *Transport Properties of Ions in Gases*, John Wiley & Sons, New York, 1988.
- [3] J. Baumbach, Ion mobility spectrometry in scientific literature and in the International Journal for Ion Mobility Spectrometry (1998-2007), *Int. J. Ion Mobil. Spec.* 11 (2008) 3.
- [4] G. Eiceman, Z. Karpas, *Ion Mobility Spectrometry*, CRC Press, Inc., Boca Raton, Ann Arbor, London, Tokyo, 1994.
- [5] K. Brown, G. Tautfest, Faraday-Cup Monitors for High-Energy Electron Beams, *Review of Scientific Instruments* 27 (1956) 696.
- [6] P. Dugourd, R. Hudgins, D. Clemmer, M. Jarrold, High-resolution ion mobility measurements, *Rev. Sci. Instrum.* 68 (1997) 1122.
- [7] C. Iceman, C. Rue, R. Moision, B. Chatterjee, P. Armentrout, Ion Mobility Studies of Electronically Excited States of Atomic Transition Metal Cations: Development of an Ion Mobility Source for Guided Ion Beam Experiments, *J. Am. Soc. Mass Spectrom.* 18 (2007) 1196.
- [8] P. Kemper, M. Bowers, State-Selected Mobilities of Atomic Cobalt Ions, *J. Am. Chem. Soc.* 112 (1990) 3231.
- [9] C. Düllmann, W. Bröchle, R. Dressler, K. Eberhardt, B. Eichler, R. Eichler, H. Gäggeler, T. Ginter, F. Glaus, K. Gregorich, D. Hoffman, E. Jäger, D. Jost, U. Kirbach, D. Lee, H. Nitsche, J. Patin, V. Pershina, D. Piguet, Z. Qin, M. Schädel, B. Schausten, E. Schimpf, H.-J. Schött, S. Soverna, R. Sudowe, P. Thörle, S. Timokhin, N. Trautmann, A. Türler, A. Vahle, G. Wirth, A. Yakushev, P. Zielinski, Chemical investigation of hassium (element 108), *Nature* 418 (2002) 859.
- [10] R. Eichler, N. Aksenov, A. Belozarov, G. Bozhikov, V. Chepigin, S. Dmitriev, R. Dressler, H. Gäggeler, V. Gorshkov, F. Haenssler, M. Itkis, A. Laube, V. Lebedev, O. Malyshev, Y. Oganessian, O. Petrushkin, D. Piguet, P. Rasmussen, S. Shishkin, A. Shutov, A. Svirikhin, E. Tereshatov, G. Vostokin, M. Wegrzecki, A. Yerebin, Chemical characterization of element 112, *Nature* 447 (2007) 72.
- [11] R. Eichler, N. Aksenov, A. Belozarov, G. Bozhikov, V. Chepigin, R. Dressler, S. Dmitriev, H. Gäggeler, V. Gorshkov, R. Henderson, M. Itkis, A. Johnsen,

- J. Kenneally, V. Lebedev, O. Malyshev, K. Moody, Y. Oganessian, O. Petrushkin, D. Piguët, A. Popeko, P. Rasmussen, A. Serov, D. Shaughnessy, S. Shishkin, A. Shutov, M. Stoyer, N. Stoyer, A. Svirikhin, E. Terechatov, G. Vostokin, M. Wegrzecki, P. Wilk, A. Yeremin, Chemical investigation of element 114 - status report, Contribution to the seventh international conference on nuclear and radiochemistry, Budapest, Hungary. <http://www.nrc7.mke.org.hu/pdf/presentations/abstract104.pdf> (2008).
- [12] M. Sewtz, H. Backe, A. Dretzke, G. Kube, W. Lauth, P. Schwamb, K. Eberhardt, C. Grüning, P. Thörle, N. Trautmann, P. Kunz, J. Lassen, G. Passler, C. Dong, S. Fritzsche, R. Haire, First Observation of Atomic Levels for the Element Fermium ($Z=100$), *Phys. Rev. Lett.* 90, 163002 (2003) ,.
- [13] M. Sewtz, H. Backe, C. Dong, A. Dretzke, K. Eberhardt, S. Fritzsche, C. Grüning, R. Haire, G. Kube, P. Kunz, J. Lassen, W. Lauth, G. Passler, P. Schwamb, P. Thörle, N. Trautmann, Resonance ionization spectroscopy of fermium ($Z=100$), *Spectrochim. Acta B* 58 (2003) 1077.
- [14] H. Backe, A. Dretzke, R. Horn, T. Kolb, W. Lauth, R. Repnow, M. Sewtz, N. Trautmann, Ion mobility measurements and ion chemical reaction studies at heavy elements in a buffer gas cell, *Hyperfine Interactions* 162 (2005) 77.
- [15] M. Sewtz, M. Laatiaoui, K. Schmid, D. Habs, Prospects of ion-mobility measurements in superheavy element research, *Eur. Phys. J. D* 45 (2007) 139.
- [16] P. Indelicato, J. Santos, S. Bourcard, J. Desclaux, QED and relativistic corrections in superheavy elements, *Eur. Phys. J. D* 45 (2007) 155.
- [17] P. Pyykkö, Relativistic effects in structural chemistry, *Chem. Rev.* 88 (1988) 563.
- [18] P. Pyykkö, M. Tokman, L. Labzowsky, Estimated valence-level Lamb shifts for group 1 and group 11 metal atoms, *Phys. Rev. A* 57 (1998) R689.
- [19] I. Grant, Relativistic calculation of atomic structures, *Advances in Physics* 19 (1970) 747.
- [20] V. Pershina, Electronic Structure and Properties of the Transactinides and their Compounds, *Chem. Rev.* 96 (1996) 1977.
- [21] J. Desclaux, Relativistic Dirac-Fock Expectation Values for Atoms with $Z = 1$ to $Z = 120$, *At. Data Nucl. Data Tables* 12 (1973) 311.
- [22] H. Backe, A. Dretzke, K. Eberhardt, S. Fritzsche, C. Grüning, G. Gwinner, R. Haire, G. Huber, J. Kratz, G. Kube, P. Kunz, J. Lassen, W. Lauth, G. Passler, R. Repnow, D. Schwalm, P. Schwamb, M. Sewtz, P. Thörle, N. Trautmann, A. Waldek, First Determination of the Ionization Potential of Actinium and First Observation of Optical Transitions in Fermium, *J. Nucl. Sci. Techn., Suppl.* 3 (2002) 86.
- [23] P. Pyykkö, Dirac-Fock One-Centre Calculations Part 8. The $^1\sum$ States of ScH, YH, LaH, AcH, TmH, LuH and LrH, *Physica Scripta* 20 (1979) 647.

- [24] L. Viehland, E. Mason, Statistical-mechanical theory of gaseous ion-molecule reactions in an electrostatic field, *The Journal of Chemical Physics* 66 (1977) 422.
- [25] S. Lin, L. Viehland, E. Mason, Three-Temperature Theory of Gaseous Ion Transport, *Chemical Physics* 37 (1979) 411.
- [26] L. Viehland, Velocity distribution functions and transport coefficients of atomic ions in atomic gases by a Gram-Charlier approach, *Chemical Physics* 179 (1994) 71.
- [27] E. Horwitz, in: J.D. Navratil and W.W. Schulz (Eds.), *Transplutonium Elements - Production and Recovery*, American Chemical Society, ACS Symposium Series, Volume 161, Washington D. C., 1981.
- [28] Y. Kudryavtsev, B. Bruyneel, M. Huyse, J. Gentens, P. Bergh, P.V.Duppen, L. Vermeeren, A gas cell for thermalizing, storing and transporting radioactive ions and atoms. part i: Off-line studies with a laser ion source, *Nucl. Instr. and Meth. in Phys. Res. B* 179 (2001) 412.
- [29] J. Neumayr, L. Beck, D. Habs, S. Heinz, J. Szerypo, P. Thirolf, V. Varentsov, F. Voit, D. Ackermann, D. Beck, M. Block, Z. Di, S. Eliseev, H. Geissel, F. Herfurth, F. Heßberger, S. Hofmann, H. Kluge, M. Mukherjee, G. Münzenberg, M. Petrick, W. Quint, S. Rahaman, C. Rauth, D. Rodriguez, C. Scheidenberger, G. Sikler, Z. Wang, C. Weber, W. Plaß, M. Breitenfeldt, A. Chaudhuri, G. Marx, L. Schweikhard, A. Dodonov, Y. Novikov, M. Suhonen, The ion-catcher device for SHIPTRAP, *Nucl. Instr. and Meth. B* 244 (2006) 489.
- [30] H. Backe, K. Eberhardt, R. Feldmann, M. Hies, H. Kunz, W. Lauth, R. Martin, H. Schöpe, P. Schwamb, M. Sewtz, P. Thörle, N. Trautmann, S. Zauner, A Compact Apparatus for Mass Selective Resonance Ionization Spectroscopy in a Buffer Gas Cell, *Nucl. Instr. Meth. Phys. Res. B* 126 (1997) 406.
- [31] R. Ambartzumian, V. Letokhov, Selective Two-Step (STS) Photoionization of Atoms and Photodissociation of Molecules by Laser Radiation, *Applied Optics* 11 (1972) 354.
- [32] V. Letokhov, V. Chebotayev, *Nonlinear Laser Spectroscopy*, Springer-Verlag, Berlin Heidelberg New York, 1977.
- [33] G. Hurst, M. Payne, S. Kramer, J. Young, Resonance ionization spectroscopy and one-atom detection, *Rev. Mod. Phys.* 51 (1979) 767.
- [34] J. Townsend, The Diffusion of Ions into Gases, *Philos. Trans. R. Soc. A* 193 (1899) 129.
- [35] H. Ellis, M. Thackston, E. McDaniel, E. Mason, Transport Properties of Gaseous Ions over a Wide Energy Range. Part III, *Atomic Data and Nuclear Data Tables* 31 (1984) 113.
- [36] L. Viehland, E. Mason, Gaseous ion mobility in electric fields of arbitrary strength, *Annals of Physics* 91 (1975) 499.

- [37] H. Ellis, R. Pai, E. McDaniel, E. Mason, L. Viehland, Transport Properties of Gaseous Ions over a Wide Energy Range, *Atomic Data and Nuclear Data Tables* 17 (1976) 177.
- [38] H. Neuert, *Atomare Stoßprozesse*, Teubner-Studienbücher: Physik, Teubner-Verlag, Stuttgart, 1984.
- [39] S. Kim, K. Betty, F. Karasek, Mobility Behavior and Composition of Hydrated Positive Reactant Ions in Plasma Chromatography with Nitrogen Carrier Gas, *Analytical Chemistry* 50.
- [40] L. Viehland, E. Mason, W. Morrison, M. Flannery, Tables of Transport Collision Integrals for (n, 6, 4) Ion-Neutral Potentials, *Atomic Data and Nuclear Data Tables* 16 (1975) 495.
- [41] J. Hirschfelder, C. Curtis, R. Bird, *Molecular Theory of Gases and Liquids*, Wiley, New York, 1964.
- [42] A. Buchachenko, G. Chałasiński, M. Szcześniak, Interactions of lanthanide atoms: Comparative ab initio study of YbHe, Yb₂, and TmHe, TmYb potentials, *Eur. Phys. J. D* 45 (2007) 147.
- [43] H. Revercomb, E. Mason, Theory of Plasma Chromatography/Gaseous Electrophoresis- A Review, *Anal. Chem.* 47 (1975) 970.
- [44] J. Äystö, Development and applications of the IGISOL technique, *Nuclear Physics A* 693 (2001) 477.
- [45] C. Weber, V. Elomaa, R. Ferrer, C. Fröhlich, D. Ackermann, J. Ästö, G. Audi, L. Batist, K. Blaum, M. Block, A. Chaudhuri, M. Dworschak, S. Eliseev, T. Eronen, U. Hager, J. Hakala, F. Herfurth, F. Heßberger, S. Hofmann, A. Jokinen, A. Kankainen, H. Kluge, K. Langanke, A. Martin, G. Martinez-Pinedo, M. Mazzocco, I. Moore, J. Neumayr, Y. Novikov, H. Penttilä, W. Plaß, A. Popov, S. Rahaman, T. Rauscher, C. Rauth, J. Rissanen, D. Rodriguez, A. Saastamoinen, C. Scheidenberger, L. Schweikhard, D. Seliverstov, T. Sonoda, F. Thielemann, P. Thirolf, G. Vorobjev, Mass measurements in the vicinity of the rp-process and the np-process paths with the Penning trap facilities JYFLTRAP and SHIP-TRAP, *Physical Review C* 78 (2008) 054310.
- [46] W. Lauth, *Optische Spektroskopie mit radioaktivem Zerfallsnachweis am Spaltisomer ^{242m}Am und ²⁰⁸Tl*, Dissertation, Institut für Kernphysik, Universität Mainz (1991).
- [47] H. Backe, M. Hies, H. Kunz, W. Lauth, O. Curtze, P. Schwamb, M. Sewtz, W. Theobald, R. Zahn, K. Eberhardt, N. Trautmann, D. Habs, R. Repnow, B. Fricke, Isotope Shift Measurements for Superdeformed Fission Isomeric States, *Phys. Rev. Lett.* 80 (1998) 920.
- [48] H. Backe, A. Dretzke, S. Fritzsche, R. Haire, P. Kunz, W. Lauth, M. Sewtz, N. Trautmann, Laser Spectroscopic Investigation of the Element Fermium (Z = 100), *Hyperfine Interactions* 162 (2005) 3.

- [49] H. Backe, P. Kunz, W. Lauth, A. Dretzke, R. Horn, T. Kolb, M. Laatiaoui, M. Sewtz, D. Ackermann, M. Block, F. Herfurth, F. Heßberger, S. Hofmann, R. Mann, Towards optical spectroscopy of the element nobelium ($z=102$) in a buffer gas cell, *Eur. Phys. J. D* 45 (2007) 99.
- [50] P. Schwamb, Entwicklung eines Detektors zum direkten massenselektiven Ionennachweis nach Resonanzionisationsspektroskopie in einer Puffergaszelle, Dissertation, Institut für Kernphysik, Universität Mainz (1996).
- [51] M. Sewtz, Optische Spektroskopie an Fermium ($Z=100$), Dissertation, Institut für Kernphysik, Universität Mainz (2003).
- [52] H. Backe, W. Lauth, W. Achenbach, M. Hain, M. Hies, A. Scherer, A. Steinhof, S. Tölg, S. Ziegler, Fission fragment anisotropy for the ^{242m}Am fission isomer by spin exchange pumping with polarized rubidium vapour, *Nucl. Instr. Meth. Phys. Res. B* 70 (1992) 521.
- [53] W. Lauth, H. Backe, M. Dahlinger, I. Klaft, P. Schwamb, G. Schwickert, N. Trautmann, U. Othmer, Resonance ionization spectroscopy in a buffer gas cell with radioactive decay detection, demonstrated using Tl 208, *Phys. Rev. Lett.* 68 (1992) 1675.
- [54] K. Bier, Zur Wirkung von Verdichtungsstößen im Übergangsbereich zwischen gasdynamischer und molekularer Strömungsform, *Fortschritte der Physik* 11 (1963) 325.
- [55] W. Paul, M. Raether, Das elektrische Massenfilter, *Zeitschrift für Physik* 140 (1955) 262.
- [56] W. Paul, H. Reinhard, U. Zahn, Das elektrische Massenfilter als Massenspektrometer und Isotopentrenner, *Zeitschrift für Physik* 152 (1958) 143.
- [57] P. Milonni, J. Eberly, *Lasers*, John Wiley & Sons, Inc., New York, 1988.
- [58] W. Demtröder, *Laserspektroskopie*, 3rd Printing, Springer-Verlag, Berlin, 1988.
- [59] S. Chin, P. Lambropoulos, *Multiphoton Ionization of Atoms*, Academic Press, Inc., Toronto, Orlando, San Diego, San Francisco, New York, London, Montreal, Sydney and Tokyo, 1984.
- [60] U. Brackmann, *Lambdachrome Laser-grade Dyes, Data Sheets*, Tech. rep., Lambda Physik GmbH, D-3400 Göttingen (1986).
- [61] *Radiant Dyes, Instruction Manual*, Tech. rep., Radiant Dyes (2000).
- [62] J. Sansonetti, W. Martin, S. Young, *Handbook of Basic Atomic Spectroscopic Data* (2009).
URL <http://physics.nist.gov/PhysRefData/Handbook>
- [63] A. Morbach, Experimentelle Entwicklungen zur optischen Spektroskopie an Trans-Einsteinium-Elementen, Diplomarbeit, Institut für Kernphysik, Universität Mainz (2001).

-
- [64] S. Hofmann, G. Münzenberg, The discovery of the heaviest elements, *Rev. Mod. Phys.* 72 (2000) 733.
- [65] D. Dahl, SIMION 3D 7.0, Tech. rep., Idaho National Engineering Laboratory (2000).
- [66] C. Lock, E. Dyer, Simulation of Ion Trajectories through a High Pressure Radio Frequency Only Quadrupole Collision Cell by SIMION 6.0, *Rapid Commun. Mass Spectrom.* 13 (1999) 422.
- [67] D. Lunney, R. Moore, Cooling of mass-separated beams using a radiofrequency quadrupole ion guide, *Int. J. Mass Spectrom.* 190/191 (1999) 153.
- [68] M. Leino, H. Kankaanpää, R. Herzberg, A. Chewter, F. Heßberger, Y. LeCoz, F. Becker, P. Butler, J. Cocks, O. Dorvaux, K. Eskola, J. Gerl, P. Greenlees, K. Helariutta, M. Houry, G. Jones, P. Jones, R. Julin, S. Juutinen, H. Ketunen, T. Khoo, A. Kleinböhl, W. Korten, P. Kuusiniemi, R. Lucas, M. Muikku, P. Nieminen, R. Page, P. Rahkila, P. Reiter, A. Savelius, C. Schlegel, C. Theisen, W. Trzaska, H. Wollersheim, In-beam study of ^{254}No , *Eur. Phys. J. A* 6 (1999) 63.
- [69] L. Madansky, R. Pidd, Characteristics of the Parallel-Plate Counter, *Phys. Rev.* 73 (1948) 1215.
- [70] J. Cub, C. Gund, D. Pansegrau, G. Schrieder, H. Stelzer, A position sensitive parallel plate avalanche counter for single particle and current readout, *Nucl. Instr. and Meth. A* 453 (2000) 522.
- [71] Goodfellow GmbH (2009).
URL <http://www.goodfellow.com>
- [72] J. Neumayr, The buffer-gas cell and the extraction RFQ for SHIPTRAP, Dissertation, Fakultät für Physik der LMU München (2004).
- [73] J. Neumayr, P. Thirof, D. Habs, S. Heinz, V. Kolhinen, M. Sewtz, J. Szerypo, Performance of the MLL-IonCatcher, *Rev. Sci. Instrum.* 77 (2006) 065109.
- [74] Y. Raizer, *Gas Discharge Physics*, Springer-Verlag, Berlin Heidelberg New York, 1991.
- [75] M. Radmilović-Radjenović, Z. Petrović, G. Malović, D. Marić, B. Radjenović, Modelling of low-pressure gas breakdown in uniform DC electric field by PIC technique with realistic secondary electron emission, *Czechoslovak Journal of Physics, Suppl. B* 56 (2006) B996.
- [76] K. Burm, Calculation of the Townsend Discharge Coefficients and the Paschen Curve Coefficients, *Contrib. Plasma Phys.* 47 (2007) 177.
- [77] V. Lisovskiy, S. Yakovin, V. Yegorenkov, Low-pressure gas breakdown in uniform dc electric field, *J. Phys. D: Appl. Phys.* 33 (2000) 2722.
- [78] M. Zucrow, J. Hoffman, *Gas Dynamics, Vol. I*, John Wiley & Sons, New York, 1976.

- [79] V. Varentsov, D. Habs, "Fair-wind gas cell" - a new concept of a buffer gas cell design, *Nucl. Instr. Meth. A* 496 (2003) 286.
- [80] M. Wutz, H. Adam, W. Walcher, *Theory and Practice of Vacuum Technology*, Friedr. Vieweg & Sohn Verlagsgesellschaft mbH, Braunschweig, 1989.
- [81] A. Bondi, Van der Waals Volumes and Radii, *Physical Chemistry* 68 (1964) 441.
- [82] J. Slater, Atomic Radii in Crystals, *The Journal of Chemical Physics* 41 (1964) 3199.
- [83] E. Clementi, D. Raimondi, W. Reinhardt, Atomic Screening Constants from SCF Functions. II. Atoms with 37 to 86 Electrons, *The Journal of Chemical Physics* 47 (1967) 1300.
- [84] R. Shannon, Revised effective ionic radii and systematic studies of interatomic distances in halides and chalcogenides, *Acta Cryst.* A32 (1976) 751.
- [85] H. Haken, H. Wolf, *Atom- und Quantenphysik*, 5. Auflage, Springer-Verlag, Berlin, Heidelberg, 1993.
- [86] W. Umrath, H. Adam, A. Bolz, H. Boy, H. Dohmen, K. Gogol, W. Jorisch, W. Mönning, H.-J. Mundinger, H.-D. Otten, W. Scheer, H. Seiger, W. Schwarz, K. Stepputat, D. Urban, H.-J. Wirtzfeld, H.-J. Zenker, *Fundamentals of Vacuum Technology*, LEYBOLD VACUUM PRODUCTS AND REFERENCE BOOK, Tech. rep., Oerlikon Leybold Vacuum, <http://www.oerlikon.com/leyboldvacuum> (2001/2002).
- [87] S. Dushman, J. Lafferty, *Scientific Foundations of Vacuum Technique*, John Wiley & Sons, New York, 1965.
- [88] J. Cottrell, R. Greathead, Extending the mass range of a sector mass spectrometer, *Mass Spectrometry Reviews* 5 (1986) 215.
- [89] Balzers, *Quadrupol-Massenspektrometer QMS 311, Betriebsanweisung (BK800013BD)*, Tech. rep., Balzers AG, FL-9496 Balzers, Fürstentum Liechtenstein.
- [90] J. Großer, *Einführung in die Teilchenoptik*, Teubner-Studienbücher: Physik, Teubner-Verlag, Stuttgart, 1983.
- [91] J. Ärje, J. Äystö, H. Hyvönen, P. Taskinen, V. Koponen, J. Honkanen, K. Valli, A. Hautojärvi, K. Vierinen, *The Ion Guide Isotope Separator On-Line, IGISOL*, *Nucl. Instr. and Meth. A* 247 (1986) 431.
- [92] D. Rodríguez-Rubiales, *An RFQ buncher for accumulation and cooling of heavy radionuclides at SHIPTRAP and high precision mass measurements on unstable Kr isotopes at ISOLTRAP*, Dissertation, Universidad de Valencia - CSIC, Instituto de Física Corpuscular, Departamento de Física Atómica, Molecular i Nuclear (2003).
- [93] M. Sewtz, *Entwicklung eines HF-Quadrupols für ein Iontentransportsystem*, Diplomarbeit, Institut für Kernphysik, Universität Mainz (1997).

-
- [94] W. Paul, Electromagnetic traps for charged and neutral particles, *Rev. Mod. Phys.* 62 (1990) 531.
- [95] F. Major, V. Gheorghe, G. Werth, *Charged Particle Traps*, Springer-Verlag, Berlin Heidelberg New York, 2005.
- [96] G. Lee-Whiting, L. Yamazaki, Semi-Analytical Calculations for Circular Quadrupoles, *Nucl. Instr. and Meth.* 94 (1971) 319.
- [97] R. March, J. Todd, *Quadrupole Ion Trap Mass Spectrometry*, Second Edition, John Wiley & Sons, Hoboken, New Jersey, 2005.
- [98] T. Kim, *Buffer Gas Cooling of Ions in a Radio Frequency Quadrupole Ion Guide*, Dissertation, McGill University, Montreal, Canada (1997).
- [99] Dr. Sjuts Optotechnik GmbH (2009).
URL <http://www.sjuts.com>
- [100] H. Schöpe, *Entwicklung eines Systems zum massenselektiven Nachweis von Ionen nach Resonanzionisation in einer Puffergaszelle*, Diplomarbeit, Institut für Kernphysik, Universität Mainz (1992).
- [101] Linde AG (2009).
URL <http://www.linde-gas.de>
- [102] Air Liquide Deutschland GmbH (2009).
URL <http://www.airliquide.de>
- [103] SAES, St 707TM product catalog, Tech. rep., SAES Getters Deutschland GmbH, Köln, <http://www.saesgetters.com> (1999).
- [104] Lambda Physik, Excimer Laser EMG 101-104 MSC, Instruction Manual, Tech. rep., Lambda Physik GmbH, D-3400 Göttingen (1985).
- [105] M. Hies, *Messung von Isotopieverschiebungen am Spaltisomer ^{242f}Am mit optischer Spektroskopie*, Dissertation, Institut für Kernphysik, Universität Mainz (1993).
- [106] Lambda Physik, FL 2002 Operators Manual, Rev. 1, Tech. rep., Lambda Physik GmbH, D-37079 Göttingen (1982).
- [107] ATOS, Lambdameter LM-007, Operation manual, Tech. rep., ATOS GmbH, <http://www.cluster.orc.ru> (2005).
- [108] National Instruments Corporation, R Series Intelligent DAQ with Onboard Processing, Data Sheet (2009).
URL <http://www.ni.com/dataacquisition>
- [109] Leybold Inficon, TranspectorWareTM, User Guide, version 2, Part No.074-255, Tech. rep., Leybold Inficon Inc., New York (1995).
- [110] C. Delaney, *Electronics for the Physicist with Applications*, John Wiley & Sons, New York, 1980.

- [111] G. Goodrich, W. Wiley, Continuous Channel Electron Multiplier, *Rev. Sci. Instrum.* 33 (1962) 761.
- [112] BURLE INDUSTRIES, Electron Multiplier Handbook for Mass Spectrometry Applications, Tech. rep., BURLE INDUSTRIES INC., Lancaster, Pennsylvania (USA), <http://www.burle.com> (2009).
- [113] A. Dretzke, Untersuchungen zu ionenchemischen Reaktionen und Mobilitätsmessungen an schweren Elementen in einer Puffergaszelle, Dissertation, Institut für Kernphysik, Universität Mainz (2003).
- [114] K. Eberhardt, P. Thörle, A. Nähler, N. Trautmann, Preparation of Actinide Targets by Electrodeposition for Heavy-Ion Studies and Laserspectroscopic Investigations, *AIP Conference Proceedings*, AIP Press, 576 (2004) 1144.
- [115] P. Kunz, Resonanzionisations-Massenspektrometrie mit gepulsten und kontinuierlichen Lasern an Plutonium, Dissertation, Institut für Kernphysik, Universität Mainz (2004).
- [116] H. Maier, Preparation of Nuclear Accelerator Targets by Vacuum Evaporation, *IEEE Transactions on Nuclear Science NS-28* (1981) 1576.
- [117] H. Maier, R. Grossmann, H. Friebel, Radioactive targets for nuclear accelerator experiments, *Nuclear Instruments and Methods in Physics Research B* 56/57 (1991) 926.
- [118] H. Maier, Preparation of ^{180}Ta targets by high vacuum evaporation-condensation, *Nuclear Instruments and Methods in Physics Research A* 397 (1997) 110.
- [119] J. Magill, G. Pfennig, J. Galy, Chart of the nuclides, 7th edition, European Communities (2006).
- [120] S. Bader, W. Urfer, J. Baumbach, Preprocessing of ion mobility spectra by longitudinal detailing and wavelet transform, *Int. J. Ion Mobil. Spec.* 11 (2008) 43.
- [121] M. Tabrizchi, E. Khezri, The effect of ion molecule reactions on peaks in ion mobility spectrometry, *Int. J. Ion Mobil. Spec.* 11 (2008) 19.
- [122] P. Kemper, M. Bowers, Electronic-State Chromatography: Application to First-Row Transition-Metal Ions, *J. Phys. Chem.* 95 (1991) 5134.
- [123] W. Siems, C. Wu, E. Tarver, H. Hill, P. Larsen, D. McMinn, Measuring the Resolving Power of Ion Mobility Spectrometers, *Anal. Chem.* 66 (1994) 4195.
- [124] S. Rokushika, H. Hatano, M. Baim, H. Hill, Resolution Measurement for Ion Mobility Spectrometry, *Anal. Chem.* 57 (1985) 1902.
- [125] M. Tabrizchi, F. Rouholahnejad, Pressure effects on resolution in ion mobility spectrometry, *Talanta* 69 (2006) 87.
- [126] J. Elder, Thermal convection, *Journal of the Geological Society* 133 (1977) 293.
- [127] P. Patnaik, Handbook of Inorganic Chemicals, McGraw-Hill Professional Publishing, New York Chicago San Francisco Lisbon London Madrid Mexico City Milan New Delhi San Juan Seoul Singapore Sydney Toronto, 2002.

-
- [128] R. Honig, D. Kramer, Vapour Pressure Data for the Solid and Liquid Elements, *RCA Review* 30 (1969) 285.
- [129] M. Tooma, M. Ueno, K. Kobayashi, K. Tsuchida, K. Suzuki, Reduction of Charge Transfer Loss in Atomic Laser Isotope Separation by Production of Excited Ions through Autoionization Levels, *Journal of Nuclear Science and Technology* 33 (1996) 582.
- [130] J. Hasted, D. Phil, Inelastic collisions between ions and atoms, *Proceedings of the Royal Society of London A* 212 (1952) 235.
- [131] I. Hughes, M. Däne, A. Ernst, W. Hergert, M. Lüders, J. Poulter, J. Staunton, A. Svane, Z. Szotek, W. Temmerman, Lanthanide contraction and magnetism in the heavy rare earth elements, *Nature* 446 (2007) 650.
- [132] T. Braun, G. Ghersini, *Extraction Chromatography*, Elsevier Scientific Pub. Co., *Journal of Chromatography Library*; v. 2, Amsterdam New York, 1975.
- [133] M. Tooma, M. Ueno, K. Tsuchida, K. Kobayashi, K. Suzuki, Y. Naitoh, Y. Takizawa, T. Katou, Cross Sections of Charge Transfer between Uranium Atoms and Ions Produced by Autoionization, *Journal of Nuclear Science and Technology* 37 (2000) 559.
- [134] S. Sakabe, Y. Izawa, Cross sections for resonant charge transfer between atoms and their positive ions: collision velocity $\lesssim 1$ a.u., *Atomic Data and Nuclear Data Tables* 49 (1991) 257.
- [135] S. Sakabe, Y. Izawa, Simple formula for the cross sections of resonant charge transfer between atoms and their positive ions at low impact velocity, *Physical Review A* 45 (1992) 2086.
- [136] S. Allison, Experimental Results on Charge-Changing Collisions of Hydrogen and Helium Atoms and Ions at Kinetic Energies above 0.2 keV, *Reviews of Modern Physics* 30 (1958) 1137.
- [137] W. Lindinger, Reactions of Doubly Charged Ions at Near Thermal Energies, *Physica Scripta T3* (1983) 115.
- [138] M. Saha, On a Physical Theory of Stellar Spectra, *Proceedings of the Royal Society of London A* 99 (1921) 135.
- [139] R. Fowler, E. Milne, Intensities of Absorption Lines in Stellar Spectra, *Monthl. Not.* 83 (1923) 403.
- [140] J. Werning, Thermal Ionization at Hot Metal Surfaces, Diploma thesis, Radiation Laboratory, University of California Berkeley (1958).
- [141] M. Dresser, The Saha-Langmuir Equation and its Application, *Journal of Applied Physics* 39 (1968) 338.
- [142] C. Herring, M. Nichols, Thermionic Emission, *Reviews of Modern Physics* 21 (1949) 185.

- [143] V. Fomenko, Work function of yttrium and lanthanide single crystals, *Powder Metallurgy and Metal Ceramics* 33 (1994) 85.
- [144] G. Gaigalas, Z. Rudzikas, T. Zalandauskas, Studies of Lanthanides 6s Ionisation Energy, *Lithuanian Journal of Physics* 44 (2004) 249.
- [145] E. Beaty, Temperature Dependence of the Mobility of Positive Ions in Argon and Krypton, *Physical Review* 104 (1956) 17.
- [146] L. Chanin, M. Biondi, Temperature Dependence of Ion Mobilities in Helium, Neon, and Argon, *Physical Review* 106 (1957) 473.
- [147] Pfeiffer, Compact Capacitance Gauge, Operation manual, Tech. rep., Pfeiffer Vacuum GmbH, <http://www.pfeiffer-vacuum.de> (2005).
- [148] D. Manura, D. Dahl, SIMION 8.0, User Manual, Tech. rep., Scientific Instrument Services, Inc., NJ 08551 (2007).
- [149] D. Douglas, An Aerodynamic Drag Model for Protein Ions, *J. Am. Soc. Mass Spectrom.* 5 (1994) 17.
- [150] D. Manura, Additional Notes on the SIMION HS1 Collision Model. Included in the packages of SIMION 8.0. <http://simion.com/info> (2007).
- [151] M. Forbes, M. Sharifi, T. Croley, Z. Lausevic, R. March, Simulation of Ion Trajectories in a Quadrupole Ion Trap: a Comparison of Three Simulation Programs, *J. Mass Spectrom.* 34 (1999) 1219.
- [152] J. S. D.A. Dahl, T.R. McJunkin, Comparison of ion trajectories in vacuum and viscous environments using SIMION: Insights for instrument design, *International Journal of Mass Spectrometry* 266 (2007) 156.
- [153] J. Xu, W. Whitten, Monte Carlo simulation of ion transport in ion mobility spectrometry, *Int. J. Ion Mobil. Spec.* DOI 10.1007/s12127-008-0001-x.
- [154] H. Lai, T. McJunkin, C. Miller, J. Scott, J. Almirall, The predictive power of SIMION/SDS simulation software for modeling ion mobility spectrometry instruments, *International Journal of Mass Spectrometry* 276 (2008) 1.
- [155] A. Appelhans, D. Dahl, SIMION ion optics simulations at atmospheric pressure, *International Journal of Mass Spectrometry* 244 (2005) 1.
- [156] R. Teachout, R. Pack, The static dipole polarizabilities of all the neutral atoms in their ground states, *Atomic Data and Nuclear Data Tables* 3 (1971) 195.
- [157] R. Cowan, , A. Larson, D. Liberman, J. Mann, J. Waber, Statistical Approximation for Exchange in Self-Consistent-Field Calculations of the Ground State of Neutral Argon, *Physical Review* 144 (1966) 5.
- [158] H. Hickling, L. Viehland, D. Shepherd, P. Soldán, E. Lee, T. Wright, Spectroscopy of $M^+ \cdot Rg$ and transport coefficients of M^+ in Rg ($M = RbFr$; Rg = HeRn), *Phys. Chem. Chem. Phys.* 6 (2004) 4223.

- [159] A. Buchachenko, G. Chałasiński, M. Szcześniak, Van der Waals interactions and dipole polarizabilities of lanthanides: Tm(2F)He and Yb(1S)He potentials, *J. Chem. Phys.* 124, 114301 (2006).
- [160] A. Buchachenko, private communications.
- [161] L. Viehland, private communications.
- [162] L. Viehland, Gaseous ion transport coefficient, *Chemical Physics* 70 (1982) 149.
- [163] W. Orttung, D. Julien, Polarizability Densities within Atoms. 2. Helium, Neon, and Argon, *J. Phys. Chem.* 87 (1983) 1438.
- [164] F. Cloke, Zero oxidation state compounds of scandium, yttrium, and the lanthanides, *Chemical Society Reviews* 22 (1993) 17.
- [165] D. Eagles, Effective fields in atomic polarizability calculations, *Molecular Physics* 34 (1977) 601.
- [166] G. Chandler, R. Glass, The calculation of atomic polarizabilities, with emphasis on the first transition series, *International Reviews in Physical Chemistry* 5 (1986) 293.
- [167] B. Fricke, W. Greiner, J. Waber, The Continuation of the Periodic Table up to $Z=172$. The Chemistry of Superheavy Elements., *Theoret. chim. Acta (Berl.)* 21 (1971) 235.
- [168] Y. Kudryavtsev, J. Andrzejewski, N. Bijnens, S. Franchoo, J. Gentens, M. Huyse, A. Piechaczek, J. Szerypo, I. Reusen, P.V.Duppen, P. Bergh, L. Vermeeren, J. Wauters, A. Wöhr, Beams of short lived nuclei produced by selective laser ionization in a gas cell, *Nucl. Instr. and Meth. in Phys. Res. B* 114 (1996) 350.
- [169] K. Sasaki, H. Watarai, Reaction between laser ablation plume and ambient gas studied by laser-induced fluorescence imaging spectroscopy, *Journal of Physics: Conference Series* 59 (2007) 60.
- [170] P. Armentrout, Chemistry of Excited Electronic States, *Science* 251 (1991) 175.
- [171] M. Schädel, Superheavy element chemistry at GSI - status and perspectives, *Eur. Phys. J. D* 45 (2007) 67.
- [172] C. Düllmann, Contribution to the International WE-Heraeus Summer School: "Atomic Properties of the Heaviest Elements", Wittenberg, Germany. <http://www.superheavies.de> (2008).
- [173] R. Grob, E. Barry, *Modern Practice of Gas Chromatography*, John Wiley & Sons, New York, 2004.
- [174] C. Düllmann, Physical pre-separation: A powerful new method for transactinide chemists, *Eur. Phys. J. D* 45 (2007) 75.
- [175] M. Belov, B. Clowers, D. Prior, W. Danielson, A. Liyu, B. Petrities, R. Smith, Dynamical Multiplexed Ion Mobility Time-of-Flight Mass Spectrometry, *Anal. Chem.* 80 (2008) 5873.

-
- [176] B. Clowers, Y. Ibrahim, D. Prior, W. Danielson, M. Belov, R. Smith, Enhanced Ion Utilization Efficiency Using an Electrodynamic Ion Funnel Trap as an Injection Mechanism for Ion Mobility Spectrometry, *Anal. Chem.* 80 (2008) 612.
- [177] S. Henderson, S. Valentine, A. Counterman, D. Clemmer, ESI/Ion Trap/Ion Mobility/Time-of-Flight Mass Spectrometry for Rapid and Sensitive Analysis of Biomolecular Mixtures, *Anal. Chem.* 71 (1999) 291.
- [178] V. Letokhov, *Laser Photoionization Spectroscopy*, Academic Press, Inc., Orlando, San Diego, New York, Austin, Boston, Sydney, Tokyo and Toronto, 1987.
- [179] V. Letokhov, *Laser Photoionization Spectroscopy of Single Atoms and Molecules*, *Optica Acta* 32 (1985) 1191.
- [180] R. Martin, *Hyperfeinspektroskopie an ^{243}Am in einer Puffergaszelle mit direktem massenselektivem Ionennachweis*, Diplomarbeit, Institut für Kernphysik, Universität Mainz (1996).
- [181] iseg Spezialelektronik GmbH (2009).
URL <http://www.iseg-hv.de>
- [182] F. Paschen, *Annalen der Physik und Chemie* 37 (1889) 69.
- [183] H. Schade, E. Kunz, *Strömungslehre*, Walter de Gruyter, Berlin New York, 1989.

Acknowledgement

At the end I would like to extend my sincere gratitude and appreciation to all the many people who have contributed in various regards to the success of this work.

I would like to express deep gratitude to my supervisor Prof. Dr. Dietrich Habs, who gave me the opportunity to work on this fascinating field in atomic physics. His guidance and constant support were crucial for the successful completion of this project.

I would like to thank Dr. Werner Lauth, for his never-ending support and inspiration, which laid the ground for fruitful and successful work. I am also thankful to Dr. Michael Sewtz for his guidance through the early and difficult years of this project. His encouragement is gratefully acknowledged at this point.

Thanks goes to Prof. Dr. Hartmut Backe, who shared his knowledge with me and provided many useful hints and friendly encouragement. Special thanks are due to Dr. Peter Thirolf for his many suggestions and fast proofreading. He always managed to find the correct formulation of my beloved colloquial sentences.

Prof. Larry Viehland from the Chatham University and Dr. Alexei Buchachenko from the Moscow State University expressed their interest in my work and supplied me with the proper calculations, which gave me a better perspective on my own results.

Successful experiments would not have been possible without the help from my Munich colleagues. Many thanks are due to Dr. Jürgen Neumayr, Dr. Wolfgang Schwerdtfeger, Ludwig Trepl, Dr. Hans-Friedrich Wirth, Karl Schmid, Peter Hilz, Stefan Gärtner and Christian Lang and anyone I may have forgotten for their efforts and help before and during my experiments. Special thanks goes to Dr. Hans-Jörg Maier and Hans Ulrich Friebel for providing all kinds of filaments. Rainhardt Satzowski deserves special thanks for reliable and safe transportation of delicate experimental equipment.

The continuous commitment of the technical staff at the LMU (Garching) is gratefully appreciated. My sincere thanks go especially to Johann Krapfl and Rolf Oehm, the heads of the electronic and mechanical workshops for always timely manufacturing of all the special experimental setups and the corresponding electronic components. I would like to thank our former as well as current design engineers Michael Schumann, Christian Hübsch and Peter Hartung for their indispensable help with mechanical designs and technical drawings and for helping with many of the figures included in this thesis.

Finally I should also mention that my project was supported by the Bundesministerium für Bildung und Forschung (BMBF) under the contract number 06LM236I and by the Maier-Leibnitz-Laboratory (MLL) of the LMU and TUM.

And of course, I am grateful to my parents and my family for all their patience and mental support. Without their support this work would never have come into existence.

Munich,
December 2009

Mustapha Laatiaoui

Author's publications and conference contributions on the subject of the thesis

Papers

- H. Backe, P. Kunz, W. Lauth, A. Dretzke, R. Horn, T. Kolb, M. Laatiaoui, M. Sewtz, D. Ackermann, M. Block, F. Herfurth, F.P. Heßberger, S. Hofmann, and R. Mann, *Towards optical spectroscopy of the element nobelium ($Z=102$) in a buffer gas cell*, Eur. Phys. J. D **45**, 99 (2007)
- M. Sewtz, M. Laatiaoui, K. Schmid, and D. Habs, *Prospects of ion-mobility measurements in superheavy element research*, Eur. Phys. J. D **45**, 139 (2007)

Conference contributions

- Stopping and Manipulation of Ions (SMI06) Workshop, *Drift Time Spectrometer for Heaviest Elements*, Conference Contribution, Groningen, Holland, March 27 - 28, 2006
- Workshop on the Atomic Properties of the Heaviest Elements, *Development of a Drift Time Spectrometer for the Heaviest Elements*, Conference Contribution, Frauenwörth Chiemsee, Germany, September 25 - 27, 2006
- DPG Spring Meeting: Physics of Hadrons and Nuclei, *Development of a Drift Time Spectrometer for Heavy Element Research*, Conference Contribution, Gießen, Germany, March 12 - 16, 2007
- 3rd International Conference on the Chemistry and Physics of the Transactinide Elements, *Development of a Drift Time Spectrometer for Heavy Element Research*, Conference Contribution, Davos, Switzerland, September 23 - 28, 2007
- DPG Spring Meeting: Interaction of Matter with Ions, *Development of a Drift Time Spectrometer for Heavy Element Research*, Conference Contribution, Darmstadt, Germany, March 10 - 14, 2008
- DPG Spring Meeting: Interaction of Matter with Ions, *Relativistic Contraction Studies at Heavy Elements*, Conference Contribution, Hamburg, Germany, March 02 - 06, 2009
- SHIPTRAP Collaboration Meeting, *Prospects of Isobaric Purification via Ion Mobility Spectrometry*, Conference Contribution, Darmstadt, Germany, March 13, 2009

Summer schools

- International WE-Heraeus Summer School, *Atomic Properties of the Heaviest Elements*, Conference Contribution, Wittenberg, Germany, August 24 - September 06, 2008

Curriculum Vitae

Personal data

Name: **Mustapha Laatiaoui**
 Date of birth: 17.08.1977
 Place of birth: Oujda / Morocco
 Citizenship: Morocco
 Current address: Fakultät für Physik,
 Ludwig-Maximilians-Universität München
 Am Coulombwall 1,
 85748 Garching, Germany
 E-mail: mustapha.laatiaoui@physik.uni-muenchen.de
 Phone: +49 89 289 14083

Education

1984 - 1989: Primary school, Aklim / Morocco
 1989 - 1993: Junior high school, Aklim / Morocco
 1993 - 1996: Hauptschule-In-Der-Landwehr, Dortmund / Germany
 1996 - 1999: Helmholtz-Gymnasium, Dortmund / Germany
 Certificate: University-Entrance Diploma (Abitur)
 10.1999 - 03.2004: Technische Universität München (Eng. Physics Ba.)
 Certificate: Bachelor of Science
 Thesis: *Test of a Scintillating Fiber Readout with Avalanche Photodiodes*
 04.2004 - 09.2005: Technische Universität München (Eng. Physics Ma.)
 Certificate: Master of Science
 Thesis: *Development of Silicon-Photomultipliers for Application in the MAGIC Experiment*
 03.2006 - present: Ph.D. student in Physics at the Ludwig-Maximilians-Universität München, Germany
 Thesis: *Development of an Ion Mobility Spectrometer for Heavy Element Research*
 Supervisor: Prof. Dietrich Habs

Practical experience

03.2000: Internship in communication networks, Siemens AG, Munich / Germany
 04.2000 - 08.2004: Student trainee, Max-Planck-Institut für Physik (Werner-Heisenberg-Institut), Munich / Germany
 11.2000 - 01.2001: Internship in electronics, Max-Planck Institut für Physik (Werner-Heisenberg-Institut), Munich / Germany
 10.2005 - 01.2006: Internship in electronics, MEL Mikroelektronik GmbH, Eching / Germany